

BAIKAL-GVD

Gigaton Volume Detector in Lake Baikal

(Scientific-Technical Report)

MOSCOW - 2012

©2012

**Institute for Nuclear Research, Russian Academy of Sciences,
60th October Anniversary pr. 7a, Moscow 117312, Russia**

Joint Institute for Nuclear Research, Dubna 141980, Russia

Irkutsk State University, Irkutsk 664003, Russia

**Skobeltsyn Institute of Nuclear Physics, Moscow State University,
Moscow 119991, Russia**

**Nizhny Novgorod State Technical University, Nizhny Novgorod
603950, Russia**

**St. Petersburg State Marine Technical University, St. Petersburg
190008, Russia**

EvoLogics GmbH, Berlin, Germany

**This work was supported by the Russian Foundation for Basic
Research (grant 09-02-12295).**

CONTENTS

EXECUTIVE SUMMARY	5
1. Introduction	7
1.1. Scientific Motivation	7
1.1.1. Neutrinos from local astrophysical objects	7
1.1.2. Diffuse neutrino flux	7
1.1.3. Dark matter	8
1.1.4. Atmospheric neutrinos	9
1.1.5. Magnetic monopoles	10
1.2. Neutrino Interactions	12
1.3. Medium as a Cherenkov Light Radiator	13
1.4. Neutrino Telescopes	13
1.5. The History and Current Status	14
2. Baikal Neutrino Experiment	19
2.1. Project History	19
2.2. Site Description	22
2.3. Optical Properties	22
2.4. Baikal Underwater Neutrino Telescope	23
2.4.1. NT200	23
2.4.2. NT200+	26
2.5. Brief Review of NT200 Scientific Results	27
3. Configuration of the BAIKAL-GVD	29
3.1. Concept of Design	29
3.2. Optimization of GVD Configuration	30
3.2.1. Muons	30
3.2.2. Showers	32
3.3. Configuration	34
4. Basic Elements and Electronic Systems	35
4.1. Optical Module	35
4.1.1. Photomultiplier tube	35
4.1.2. Controller	36
4.1.3. Design of optical module	38
4.1.4. Angular sensitivity of OM	39
4.2. Section – Detection Unit of the BAIKAL-GVD	39
4.3. String	41
4.3.1. Calibration of measuring channels	42
4.4. Cluster	44
4.5. Trigger formation and Data Transfer Systems	45
4.5.1. Data transfer system	46
4.5.2. Trigger system	47

4.6. Prototype Arrays	49
4.6.1. Prototypes of GVD string	49
4.6.2. Prototypes of GVD cluster	54
4.7. Shore Data Acquisition and Control Center	57
5. Acoustic Positioning System	59
5.1. Positioning system of NT200/NT200+	59
5.2. Positioning system of the BAIKAL-GVD	64
6. Water Optical Properties	68
6.1. Determination of the Absorption Coefficient	68
6.2. Determination of the Scattering Coefficient	70
6.3. Determination of the Scattering Phase Function	72
6.4. Long-Term Monitoring of Water Optical Properties	73
6.5. Measurement Procedure	75
6.6. Light Absorption in Lake Baikal Water	76
6.7. Light Scattering in Lake Baikal Water	77
6.8. Scattering Phase Function	79
7. Deployment	80
7.1. Cable Network	80
7.2. Carrier Structures	80
7.2.1. Main elements of buoy stations	84
7.3. Deployment of Carrier Structures	90
7.4. Works in the Ice Camp	92
8. BAIKAL Neutrino Experiment	93
8.1. Expected BAIKAL-GVD Performance	93
8.1.1. Cherenkov radiation of muons	93
8.1.2. Muon events simulation	94
8.1.3. Atmospheric muons	96
8.1.4. Atmospheric neutrinos	97
8.1.5. The PMT noise and water background rejection	98
8.1.6. Reconstruction	102
8.2. High-Energy Showers	105
8.2.1. Simulation	105
8.2.2. Reconstruction	109
8.2.3. Shower angular and energy resolution	110
8.2.4. The diffuse neutrino flux detection efficiency	113
9. Final Configuration of the BAIKAL-GVD	115
Bibliography	120

EXECUTIVE SUMMARY

The BAIKAL-GVD Project in Lake Baikal is a logical extension of the research and development work performed over the last thirty years by the BAIKAL Collaboration. The optical properties of the lake deep water have been established, and the detection of high-energy neutrinos has been demonstrated with the existing detector NT200/NT200+. This achievement represents a proof of concept for commissioning a new instrument, Gigaton Volume Detector (BAIKAL-GVD), with superior detector performance and an effective telescope size at or above the kilometer-scale.

The next generation km-scale neutrino telescope BAIKAL-GVD in Lake Baikal will be a research infrastructure aimed primarily at studying astrophysical neutrino fluxes. The detector will utilize Lake Baikal water instrumented at depth with optical sensors that detect the Cherenkov radiation from secondary particles produced in interactions of high-energy neutrinos inside or near the instrumented volume. The concept of BAIKAL-GVD is based on a number of evident requirements to the design and architecture of the recording system of the new array: the utmost use of the advantages of array deployment from the ice cover of Lake Baikal, the extendability of the facility and provision of its effective operation even in the first stage of deployment, and the possibility of implementing different versions of arrangement and spatial distribution of light sensors within the same measuring system.

The design for the final state of BAIKAL-GVD neutrino telescope is an array of 10386 photomultiplier tubes (PMTs) each enclosed in a transparent pressure sphere to comprise an optical module (OM). The OMs are arranged on vertical load-carrying cables to form strings. The basic configuration of telescope consists of 27 clusters of strings – functionally independent sub-arrays, which are connected to shore by individual electro-optical cables. Each cluster comprises eight 705 m long strings of optical modules – seven peripheral strings are uniformly arranged at a 60 m distance around a central one. Each string comprises 48 OMs spaced by 15 m at depths of 600 to 1300 m below the surface. OMs on each string are combined in four sections – detection units of telescope. The distances between the central strings of neighboring clusters are $H=300$ m. The clusters are spaced over an area of approximately 2 km^2 . The water volume instrumented by OMs is about of 1.5 km^3 .

Signal events consist of upgoing muons produced in neutrino interactions in the bedrock or the water, as well as of electromagnetic and hadronic showers (“cascades”) from CC-interactions of ν_e and ν_τ or NC-interactions of all flavors inside the detector volume. Background events are mainly downward-going muons from cosmic ray interactions in the atmosphere above the detector.

The Data Acquisition System of GVD is formed from three basic functional units: optical modules, *sections* of OMs and *clusters* of strings. Each section comprises 12 OMs and the central module (CM), which consists of ADC boards, an OM slow-control unit,

and a Master board. PMT signals from all OMs of a section are transmitted to the CM, where they are digitized by ADC boards. The digitized signals from each ADC are transferred to a FPGA which handles the data. A memory buffer allows for accumulating the waveform data from the ADC. An ADC trigger request channel includes a request builder, which forms the request signals to the trigger logic, which are transferred to the Master board. The Master board provides trigger logic, data readout from ADC boards, connection via local Ethernet to the cluster DAQ center, and control of the section operation. The request analyzer forms the section trigger request (local trigger) on the basis of requests from ADC channels. The section trigger request is transferred to the cluster DAQ center.

The cluster DAQ center is placed near the water surface. It provides the string triggering, power supply control, and communication to shore. The designs of central and section trigger systems are the same. The section requests come to inputs of the central ADC board. The central Master board works out the global trigger for all sections. The global trigger initiates the stop signal for all ADC channels and readout of the waveform information. Waveform information is accumulated in the event buffer and then transmitted via an Ethernet connection to the cluster DAQ center. The cluster DAQ center is connected to shore by an about 6 km long electro-optical cable. The event rate is estimated to be about of 2 kHz for one cluster.

This document is English version of the “Scientific-Technical Report” which concluded in 2010 the BAIKAL-GVD Design Study Phase supported by the Russian Foundation for Basic Research during 2009-2010 (grant 09-02-12295). After the appearance of Russian version of Report in 2010 the Prototyping Phase of BAIKAL-GVD Project is started in 2011 by deployment and long-term in-situ operation of engineering arrays which comprise all elements and systems of GVD-cluster and are connected to shore by own electro-optical cable. Several results, obtained by these arrays are included in current document, as well as the description of accepted to date final configuration of BAIKAL-GVD which comprises 10360 optical sensors (see, Chapter 9).

1 INTRODUCTION

Neutrino telescopes are experimental measuring systems placed deep in transparent natural media in various geographical areas of the Earth that are aimed at investigating a wide spectrum of scientific problems and primarily the natural neutrino fluxes. The deep underwater detection method provides a basis for experiments to record high- and ultra-high-energy astrophysical neutrinos with neutrino telescopes. It was first proposed by M.A. Markov [1] in 1960 and consists in recording Cherenkov radiation from secondary muons and/or high-energy showers produced by the interaction of neutrinos with matter in transparent natural media. By analogy with experiments on ground-based accelerators, the natural neutrino flux that irradiates the target (water or ice, as well as bedrock in the case of muon neutrinos) is used in experiments on deep underwater telescopes. The end products of neutrino interactions - high-energy muons and showers whose Cherenkov radiation is recorded by the neutrino telescope's photo-sensors - are the carriers of information about the neutrinos.

1.1 Scientific Motivation

The astrophysical neutrino fluxes are investigated with neutrino telescopes in two main directions of research [2,3,4]. The first direction of research is concerned with the search for a neutrino signal from known astrophysical objects or the detection of unidentified local sources from observations of the signal excess above the background level over the entire celestial sphere.

1.1.1 Neutrinos from local astrophysical objects

The natural high-energy neutrino fluxes are produced by physical processes in astrophysical objects characterized by enormous energy release at a rate from 10^{39} to 10^{52} erg/s or higher. The nearest (with respect to a terrestrial observer) astrophysical objects that are currently assumed to be capable of emitting high-intensity neutrino fluxes are located mainly in the vicinity of the Galactic center and in the Galactic plane. Supernova remnants, pulsars, the neighborhood of the black hole Sgr A* at the Galactic center, binary systems containing a black hole or a neutron star, and clusters of molecular clouds that are targets for cosmic-ray protons and nuclei are the most promising Galactic sources with respect to the detection of their neutrino emission. The energy spectrum of neutrinos from Galactic sources fills the energy range 10^3 – 10^6 GeV.

Extragalactic objects - active galactic nuclei (AGN), gamma-ray bursts (GRB), starburst galaxies and galaxy clusters - belong to another class of neutrino sources whose emission can be recorded by ground-based facilities. This class of sources is characterized by much greater energy release and generates neutrinos in the energy range 10^4 – 10^8 GeV or higher. Searching for a neutrino signal from identified sources imposes stringent requirements on the resolution of neutrino telescopes from the viewpoint of measuring both neutrino energy and direction.

1.1.2 Diffuse neutrino flux

The other direction of research on the astrophysical neutrinos is to investigate the energy spectrum, global anisotropy, and neutrino flavor composition of the diffuse

neutrino flux from unidentified sources at energies above 10^4 GeV, at which the background from atmospheric neutrinos is comparable to or lower than the expected flux. The diffuse high-energy neutrino flux near the Earth is produced by neutrino emission from the entire set of sources during the period from remote cosmological epochs to the present day. Extragalactic sources make a major contribution to this flux. The neutrinos produced by the interaction of cosmic rays with interstellar matter and, in the case of ultra-high-energy cosmic rays, with electromagnetic radiation from a wide energy range, including the cosmic microwave background, also contribute to the diffuse flux. It should be noted that the neutrinos from the decay of supermassive particles associated, in particular with Grand Unified Theories (GUT) (top-down scenario) could account for a certain fraction of the diffuse flux.

The standard approach used by a wide range of theoretical models describing the formation of neutrino fluxes in cosmic-ray sources suggests the production of neutrinos mainly during the decay of π -mesons produced in pp and $p\gamma$ interactions. In this case, the flavor ratio of emitted neutrino flux is approximately $\nu_e : \nu_\mu : \nu_\tau \approx 1:2:0$. This ratio changes with distance to the source due to the neutrino oscillations. According to Super-Kamiokande experimental data [5], the $\nu_\mu \leftrightarrow \nu_\tau$ oscillation length when choosing the oscillation parameters $\delta m^2 = 2.5 \cdot 10^{-3} \text{ eV}^2$ and $\sin 2\theta = 1$ is about of $L_{\text{osc}} \sim 1.3 \cdot 10^{-4} (E_\nu / \text{PeV})$ parsecs. Thus, the oscillation length turns out to be much smaller than the characteristic distances to the presumed astrophysical sources of high-energy neutrinos and the flavor ratio is transformed in $\nu_e : \nu_\mu : \nu_\tau \approx 1:1:1$.

1.1.3 Dark matter

The biggest problem of modern natural science is to find dark matter particles. Observational data in the field of astronomy and cosmology irrefutably suggest that, apart from ordinary matter, there is matter of a new type - dark matter - in galaxies, galaxy clusters, and the Universe as a whole. Moreover, on the whole, the mass of dark matter in the Universe exceeds that of ordinary matter by a factor of 5-6.

To all appearances, dark matter is composed of as yet unknown particles with the masses which exceed appreciably that of the heaviest known stable elementary particle - the proton. These new particles must have a lifetime comparable to or exceeding the age of the Universe. Undoubtedly, such a long lifetime is related to new conservation laws in fundamental physics. It can be said with great confidence that a whole stratum of new phenomena in particle physics occurring at ultra-high energies and inaccessible to investigation on existing accelerators stands behind the dark matter particles.

Dark matter particles would interact very weakly with ordinary matter. Therefore, their direct detection, if at all possible, is an extremely complicated problem of experimental physics. A different approach to detecting dark matter particles associated with the search for the products of their annihilation at the center of the Earth, the Sun, or the Galaxy is very promising. There must be neutrinos of fairly high energies among these products, which, in turn, interact very weakly with matter and pass through the Earth or the Sun virtually without absorption. Neutrinos of such energies are successfully recorded on large underground facilities and neutrino telescopes placed in natural media.

The methods of searching for dark matter particles with underground detectors and neutrino telescopes in natural media consist in recording an excess of the muon flux in a direction away from the center of the Earth or the Sun or from the Galactic center above the background from atmospheric neutrinos. The constraints on the additional muon flux

in a direction away from the Earth's center and the Sun have been obtained on the Baksan, Super-Kamiokande, and MACRO underground facilities as well as on the underwater and under-ice neutrino telescopes NT200 (Lake Baikal), ANTARES (Mediterranean Sea), AMANDA and IceCube (South Pole). Underground neutrino detectors have a lower muon detection threshold ($\sim 1-3$ GeV) than deep underwater (under-ice) facilities. Therefore, these two classes of detectors complement each other. The former are efficient at searching for particles with a mass below 80 GeV (the threshold W-boson production energy), while the latter are efficient at investigating particles with a mass of ~ 100 GeV or higher.

A further substantial increase in the sensitivity of an experiment to the muon flux from the annihilation of dark matter particles can be achieved only by increasing their effective area. In the case of neutrino telescopes, the problem is reduced to creating cubic-kilometer facilities. In the case of underground facilities, such an increase in the effective area implies an increase in the characteristic detector sizes to a hundred meters or more. Creating such a huge underground facility seems extremely unrealistic at present.

1.1.4 Atmospheric neutrinos

Cosmic rays generate the most intense neutrino flux observed in ground-based experiments in the energy range from hundreds of MeV to hundreds of TeV. A large number of pions and kaons are produced when cosmic rays interact with atmospheric matter. The pion, kaon, and muon decay reactions

$$\pi^\pm \rightarrow \mu + \nu_\mu; K^\pm \rightarrow \mu + \nu_\mu; \mu \rightarrow e + \nu_\mu + \tilde{\nu}_e$$

produce the neutrinos which are referred to as *conventional* atmospheric neutrinos. In the energy range 100 GeV - 100 TeV, the spectrum of *conventional* atmospheric neutrinos is described by the expression:

$$\frac{d^2N}{dE_\nu d\Omega}(E_\nu, \theta) = A_\nu (E_\nu/GeV)^{-\gamma} \left[\frac{1}{1 + 6E_\nu/E_\pi(\theta)} + \frac{0.213}{1 + 1.44E_\nu/E_K(\theta)} \right],$$

where $A_\nu = 0.0285 \text{ GeV}^{-1} \text{ cm}^{-2} \text{ c}^{-1} \text{ sr}^{-1}$, $\gamma = 2.68$, E_π and E_K are the critical energies of the pions and kaons (the energies at which the decay probability is equal to the interaction probability) dependent on the zenith angle θ . The primary cosmic rays are distributed isotropically near the Earth, but the development of cascades initiated by primary radiation in the atmosphere breaks the isotropy of the fluxes of secondary particles. The pions and kaons produced by a primary particle at large zenith angles spend much of their time in a rarefied atmosphere, where the decay probability is higher than the interaction probability. Therefore, the horizontal neutrino flux exceeds the vertical one. As the energy grows, the lifetime of pions and kaons increases and, accordingly, the decay probability decreases compared to the interaction probability. Therefore, the energy spectrum of the neutrinos produced by pions and kaons becomes steeper with growing energy (the exponent γ increases by one) than the primary cosmic-ray spectrum. The uncertainty in the predictions of the neutrino fluxes from pions and kaons is related to the uncertainty in the cosmic-ray flux and energy spectrum as well as to the uncertainty in the fraction of the kaons and pions produced in a nuclear interaction at high energies. The

difference in the spectra of atmospheric neutrinos from pions and kaons calculated by different authors is about 25%.

A different neutrino production mechanism is possible at energies above 100 TeV. The *prompt* neutrinos can be produced in the decays of charmed mesons and baryons with a lifetime of the order of or less than 10^{-12} s. The spectrum of prompt neutrinos essentially follows the cosmic-ray spectrum and is flatter than that of conventional neutrinos. No prompt neutrinos have been experimentally detected so far. According to calculations, the energy at which the fluxes of prompt neutrinos become equal to and then exceed the conventional neutrino fluxes depends on the model for the interaction of primary cosmic rays with the air nuclei and on the zenith angle. For the vertical neutrino flux, this energy lies within the range 100 - 1000 TeV and increases with zenith angle.

From the viewpoint of experiments on neutrino telescopes, atmospheric neutrinos are the source of the natural unremovable background that complicates significantly the detection of astrophysical neutrinos. On the other hand, since the theoretical prediction level of the intensity and characteristics of the atmospheric neutrino flux is fairly high, this flux can be effectively used as a calibration neutrino flux. In addition, searching for prompt neutrinos is an important scientific task.

1.1.5 Magnetic monopoles

The concept of a magnetic monopole was introduced into the modern physical theory in 1931 by Dirac [6]. He showed that any magnetic charge should be a multiple of the minimum possible charge g uniquely related to the minimum electric charge:

$$g = (\hbar c/2e) \approx \frac{137}{2} e.$$

Thus, the minimum magnetic charge is approximately a factor of 68.5 larger than the minimum electric charge. In particular, this implies that the ionization energy losses for relativistic monopoles in a medium are much larger than those for relativistic muons. This opens good possibilities for the detection of fast monopoles in experiments with neutrino telescopes. The theory of Cherenkov radiation from magnetic monopoles was first examined by I.M. Frank [7]. The linear density of Cherenkov radiation with a wavelength λ (under the assumption that the permeability of the medium is $\mu \sim 1$) is described by the expression

$$\frac{d^2 n_c}{dx d\lambda} = \frac{2\pi\alpha}{\lambda^2} \left(\frac{ng}{e}\right)^2 \left(1 - \frac{1}{n^2\beta^2}\right),$$

where g is the magnetic charge of the monopole, e is the charge of electron, n is the refractive index of the medium (for water, $n=1.33$), $\beta = v/c$ is a monopole velocity expressed in units of the speed of light in vacuum and α is the fine-structure constant. The Cherenkov radiation from a relativistic monopole in water is a factor of $(ng/e)^2 \approx 8300$ more intense than that from a relativistic muon. Thus, a magnetic monopole with a speed $\beta \sim 1$ is a bright light source corresponding in intensity to a muon with an energy of $\sim 1.4 \cdot 10^4$ TeV. Intense searches for magnetic monopoles stimulated by the works [8, 9] have been performed since the mid-1970s. In these works, it was shown for the first time that the possibility of the existence of topological defects in the form of magnetic

monopoles in the Universe is a corollary of Grand Unified Theories (GUT). The masses of these particles lie in a wide range from $\sim 10^8$ GeV to $\sim 10^{21}$ GeV, depending on the GUT versions. The most reliable astrophysical constraints on the natural flux of monopoles are: the Chudakov-Parker limit [10,11,12] derived from the condition for the conservation of the observed Galactic magnetic field strength

$$F_{mon} < 10^{-15} \text{ cm}^{-2} \text{ s}^{-1} \text{ sr}^{-1},$$

and the *cosmological* constraint following from the obvious condition

$$4\pi F_{mon} m_{mon} (c\beta)^{-1} < \rho_{cr} = 10^{-29} \text{ g cm}^{-3},$$

which yields

$$F_{mon} < 1.4 \cdot 10^{-12} \beta [(10^{16} \text{ GeV}/c^2)/ m_{mon}] \text{ cm}^{-2} \text{ s}^{-1} \text{ sr}^{-1}.$$

Both these constraints do not rule out the possibility of a local excess above these limiting fluxes of monopoles, for example, in the Solar system. As a result of its acceleration in Galactic magnetic fields, the kinetic energy of a heavy monopole can reach $\sim 10^{11}$ GeV. On the other hand, when passing through the Earth, the energy losses of quasi-relativistic monopoles with $\beta \geq \beta_c$ ($\beta_c=0.75$ is the threshold speed of the monopole with respect to the generation of Cherenkov radiation) are $\sim 10^{11}$ GeV. It thus follows that monopoles with a mass of less than 10^{11} GeV passing through the Earth remain quasi-relativistic and can be detected by their Cherenkov radiation with neutrino telescopes.

In 1981, Rubakov [13] published a paper where he concluded that the processes with baryon number nonconservation are not suppressed in the presence of a monopole predicted by Grand Unified Theories. A similar conclusion was reached in 1982 by Callan [14]. The cross section for the reaction of monopole catalysis of baryon decay was estimated as

$$\sigma_{cat} = \sigma_0 / \beta_{mon},$$

where σ_0 was taken to be equal in order of magnitude to the characteristic values of strong interactions: $\sigma_0 \sim 10^{-28} \text{ cm}^2$. When the electromagnetic interaction between a monopole and a nucleus incorporating a nucleon is taken into account, the factors $F(\beta_{mon}) = 2.4 \cdot 10^7 \beta_{mon}^{3.1}$ for the nucleons constituting the ^{16}O nucleus and $F(\beta_{mon}) = 0.17/\beta_{mon}$ for free protons appear in the expression for the catalysis cross section. A monopole moving in water with a speed less than or of the order of 10^{-3} must initiate mainly the decay of hydrogen nuclei with the cross section

$$\sigma_{cat}^p = 0.17 \sigma_0 \beta_{mon}^{-2}.$$

The energy being released in a single catalysis event ($m_p c^2 = 938$ MeV) is distributed between the proton decay products. While propagating in water, the latter become the sources of Cherenkov radiation, which is also generated by their daughter particles, δ -electrons, e^+e^- pairs, etc. As a result of each proton decay, up to $N_\gamma = 1.1 \cdot 10^5$ Cherenkov photons are emitted in the wavelength range $300 < \lambda < 600$ nm. Thus, the trajectory of the muon inducing proton decays when crossing a water volume must appear as a chain of

flashes with a Cherenkov spectrum. If the decays occur frequently, for example, $10\text{-}10^3$ per 1 cm of the monopole path, then the detection rate of Cherenkov photons emitted by decay products can exceed noticeably the pulse count rate attributable to the photomultiplier dark current and water luminescence. The method of searching for slow monopoles in experiments on neutron telescopes is based on the selection of such events [15].

1.2 Neutrino Interactions

Natural high-energy neutrinos interact with the target material of neutrino telescopes mainly through the reactions on nucleons via the channels of charged (CC) and neutral (NC) currents:

$$\nu_l(\bar{\nu}_l) + N \rightarrow l^-(l^+) + \text{hadrons (CC)}, \quad (1.2.1)$$

$$\nu_l(\bar{\nu}_l) + N \rightarrow \nu_l(\bar{\nu}_l) + \text{hadrons (NC)}, \quad (1.2.2)$$

where $l = e, \mu$ or τ . The interaction of neutrinos with target electrons makes virtually no contribution to the total number of recorded events, except for the resonant scattering of electron antineutrinos in the W-resonance region:

$$\bar{\nu}_e + e^- \rightarrow W^- \rightarrow \text{all} \quad (1.2.3)$$

with the energy at resonance $E_0 = M_W^2/2m_e = 6.3 \cdot 10^6 \text{ GeV}$ and a cross section of $5.02 \cdot 10^{-31} \text{ cm}^2$. The final products of reactions (1.2.1 - 1.2.3) - leptons and high-energy cascades - carry information about the energy, direction, and, in principle, flavor of neutrinos.

In experiments on deep underwater and under-ice Cherenkov detectors, the effective target size depends on the neutrino energy and flavor. In the case of muon neutrinos, both the transparent medium around the telescope and the bedrock are the neutrino target, because the secondary muons have a high penetrating power. In the former case, the muon neutrino energy can be determined by reconstructing the energies of the muon and the shower generated at the neutrino interaction vertex. During the muon neutrino interaction in rock, the neutrino energy in each individual event cannot be reconstructed exactly due to the energy losses of the muon as it propagates from the interaction vertex to the facility. However, when the statistics of recorded events is large enough, the energy spectrum of the muon neutrino flux can be derived by the reconstruction of the muon energy. The astrophysical fluxes of electron and τ -neutrinos, which account for two thirds of the total flux, can be investigated in experiments on neutrino telescopes only by recording the secondary showers generated in a water target. Hadronic showers are produced in the interactions of neutrinos of all flavors with nuclei via the channels of charged (CC) and neutral (NC) currents. In addition, in the case of the (CC) interaction of electron and τ -neutrinos, the electron energy is converted into the energy of an electromagnetic shower, while a significant fraction of the τ -lepton energy is transferred to the hadronic or electromagnetic shower as a result of its decay. Thus, achieving a high accuracy of reconstructing the energy and direction of showers is an indispensable requirement for efficient detection of neutrinos of all flavors.

1.3 Medium As a Cherenkov Light Radiator

A transparent medium is not only the target but also the medium for the generation and propagation of Cherenkov radiation of high-energy muons and showers from the source to the neutrino telescope's photo-sensors. Investigation of the astrophysical neutrino fluxes with neutrino telescopes imposes stringent requirements on the optical properties and background conditions of the natural medium: it should have a high transparency, the temporal and angular distributions of Cherenkov photons from muons and showers at large distances from the sources should not be distorted significantly by the scattering of light in the medium and background luminescence of the medium should be at a level that allows reliable selection and identification of neutrino events. Thus, from the viewpoint of optical properties, a medium with a large light absorption and scattering length and a highly anisotropic scattering phase function is most adequate with respect to the detection efficiency. In this case, the set of temporal and amplitude information of the telescope's measuring channels allows one to accurately determine the shower coordinates, energy, and direction or to reconstruct the muon trajectory and energy. In addition, the degree of aggressiveness of the medium with respect to the structural materials is an important factor. The deep fresh water of Lake Baikal, the deep ice of the Antarctica, and the deep sea water of the Mediterranean Sea are the locations of active and currently planned neutrino telescopes. These media are characterized by unique properties, but each of them has certain advantages and disadvantages compared to the two remaining ones and, in this sense, they mutually complement each other.

1.4 Neutrino Telescopes

The basic elements of neutrino telescopes are the photo-sensors that fill a geometric volume of about 10^5 - 10^7 m³ in the case of first-generation telescopes (NT200/NT200+ [16, 17], AMANDA [18], ANTARES [19]) and a volume of the order of a cubic kilometer in the case of the next-generation telescopes (IceCube [20], BAIKAL-GVD, KM3NeT [21]). The amplitude-time response of the photo-sensors and the topology of the telescope response to Cherenkov radiation from high-energy muons and showers are the information that allows one to select neutrino events and to determine parameters of the recorded neutrinos. The studies of astrophysical neutrino fluxes by recording secondary muons or showers have their advantages and mutually complement each other.

Muons are long-range particles capable of traversing distances up to several kilometers in a dense medium, depending on their energy. When passing through the sensitive volume of a neutrino telescope, the intensity of Cherenkov radiation from a muon with $E_\mu > 1$ TeV is proportional to its energy and remains essentially constant. The peculiarities of muon propagation in a transparent medium determine the characteristic response of a neutrino telescope - the triggered photo-sensors are located along the muon trajectory, the photo-sensor trigger time sequence is determined by the muon transit time near the photo-sensor, and the photo-sensor amplitude response depends on the distance to the muon trajectory. The angular resolution of the muon trajectories in the currently operated neutrino telescopes is about 0.5-3 degrees, while the next-generation telescopes will have an angular resolution of ~ 0.1 -0.8 degrees. Thus, the method of neutrino detection using muons is a powerful tool for investigating astrophysical Galactic and

extragalactic objects. A significant shortcoming of the muon channel of research is that it is applicable only to one flavor of neutrinos - the muon neutrinos.

The high-energy showers produced at the neutrino interaction vertex are quasi-local sources of Cherenkov radiation with intensity proportional to the shower energy. The number of Cherenkov photons recorded by the photo-sensors of a telescope and, consequently, the amplitude of the recorded signal from the triggered photo-sensors decrease with increasing distance to the shower. The photo-sensor trigger time is determined by the propagation time of Cherenkov photons from the shower to the photo-sensor. Reconstructing the shower direction is a more difficult task than reconstructing the muon trajectories. In Antarctic ice, in view of intense light scattering, the accuracy of reconstruction of shower direction is about of 25° . In experiments on deep underwater telescopes, the angular resolution of the shower direction is considerably higher, $3-7^\circ$, because of the small light scattering cross section in water. Such reconstruction accuracy allows one to search for and investigate quasi-local astrophysical objects, for example, the clusters of molecular clouds in the Galactic plane by their neutrino emission, and to study the global and local anisotropy of the diffuse neutrino flux. An indubitable advantage of the shower recording channel is that showers emerge during the interaction of all three types of neutrinos in the telescope's sensitive volume. Moreover, electron and τ -neutrinos can be detected only by recording secondary showers.

1.5 The History and Current Status

In the mid-1970s, the problems of astrophysics, cosmic-ray physics, and particle physics that could be investigated with deep underwater neutrino telescopes, in particular, the Deep Underwater Muon and Neutrino Detector (DUMAND) in the Pacific Ocean near the Hawaiian Islands [22, 23], were actively discussed. In particular the scientific program of studies with the DUMAND-like array was summarized by V.S. Berezinsky and G.T. Zatsepin [2].

The ultimate DUMAND design envisaged an array of photomultiplier tubes (PMTs) housed in transparent pressure spheres spread over a cubic kilometer scale instrumented volume. The most important result achieved during the works on the DUMAND project was the in-situ testing of a Short Prototype String (SPS) that contained seven optical modules [24]. It provided the measured muon intensity as a function of depth as well as a limit on astrophysical diffuse neutrino flux. After the successful SPS test, in 1988 the technical project of the DUMAND-II was prepared [21]. This version of array would comprise 216 OMs arranged at eight strings at the corners of an octagon and one in the center, and would have 100 m in diameter and 230 m in height. The plan was to deploy the detector 30 km off the coast of Big Island, Hawaii, at a depth of 4.8 km. In December 1993, a first string of the DUMAND-II, together with a string of environmental instruments was deployed and linked to shore via a junction box placed on the ocean bottom and a shore cable which had been laid some months earlier. However, some pressure housings developed leaks and soon the communication to shore failed. The works on the DUMAND project were terminated in 1995.

The current level of knowledge about the natural high- and ultra-high-energy (10^{10} - 10^{18} eV) neutrino fluxes is mainly determined by the results obtained in the last decade in experiments on the NT200/NT200+ and AMANDA Cherenkov detectors. In 2008, the data collection with the ANTARES neutrino telescope in the Mediterranean Sea was started. These three detectors constitute the first generation of neutrino telescopes and

have an effective volume of $\sim 10^7$ m³ with respect to the detection of neutrinos with energies above 10 TeV.

In 1980, the studies aimed at creating a deep underwater Cherenkov detector at Lake Baikal were begun in the Soviet Union. In 1993, the first stage of the NT200 detector containing 36 deep underwater optical modules was deployed. The NT200 neutrino telescope was brought into operation in its full configuration in April 1998 and was the world's first underwater neutrino telescope. In 2005, the sensitive volume of the Baikal neutrino telescope was increased by installing three additional external strings containing 12 optical modules each at a distance of 100 m from the telescope center. This version of the telescope (NT200+) has been operating to the present day.

The works on the Antarctic Muon and Neutrino Detection Array (AMANDA) project at the South Pole were started in the early 1990s. In 1996, 86 optical modules placed on four strings at a depth of 1.5-1.9 km were installed [18]. The array was upgraded stepwise in succeeding years and the AMANDA detector was put into operation in February 2000 in its full configuration containing 677 optical modules arranged at 19 strings, most of them at depths between 1500 and 2000 m. AMANDA was decommissioned in 2009.

The ANTARES collaboration has been working over the last ten years on the creation of a deep underwater Cherenkov neutrino telescope in the Toulon bay of the Mediterranean Sea. ANTARES stands for Astronomy with a Neutrino Telescope and Abyss environmental RESearch. The telescope is located at a distance of 25 km from the shore at a depth of about 2400 m and contains 900 photomultiplier tubes (PMTs) grouped into triplets and placed on 12 strings 350 m in length spaced by 70 m apart [19]. The ANTARES construction started in 2002 with the deployment of a shore cable and a junction box, the central element connecting the shore cable to the detector. In 2002/2003, a preproduction string was deployed and operated for a few months. The first string of the telescope was deployed in February 2006 and the ANTARES neutrino telescope started data taking in its project configuration in March 2008.

Apart from the operating first-generation neutrino telescopes listed above, there are two Mediterranean projects, NESTOR and NEMO, aimed at creating neutrino telescopes in Greece and Italy, respectively.

The NESTOR collaboration has been working on the creation of a neutrino telescope close to Pylos at the West coast of the Peloponnesus. It should be noted that the geographical, hydrooptical, and hydrological properties of the medium and the background level due to bioluminescence processes at the telescope location suit best the requirements imposed on the water environment when creating a neutrino telescope in the Mediterranean Sea. NESTOR should consist of seven "towers" (six on the edges of a hexagon and one in the center) covering an area of about 10^5 m². A single tower should carry 168 PMTs on 12 hexagonal floors, vertically spaced by 20-30 m, each with six omnidirectional modules at the end of 16 m arms and one in the center [25]. After a long phase of tests and developments, a cable was installed to a site at 4 km depth. In 2004, a single prototype floor with 12 OMs was deployed and operated for about one month [26]. The data taken with this prototype demonstrated the detector functionality and provided a measurement of the atmospheric muon flux [27]. Currently NESTOR is part of the KM3NeT framework which is directed towards a multi-cubic kilometer detector in the Mediterranean Sea.

The NEMO (NEutrino Mediterranean Observatory) collaboration began active studies of the Mediterranean region near Sicily about ten years ago with the objective to

study the feasibility of a cubic kilometer detector, to develop corresponding technologies and to identify and explore a suitable site, in their case close to Sicily [28]. The basic units of NEMO are towers composed by a sequence of floors. Each floor consists of 15 m long horizontal *bars*, each equipped with four 10-inch PMTs [29]. A suitable site at a depth of 3.5 km, about 100 km off Capo Passero at the South-Eastern coast of Sicily has been identified and investigated during various campaigns. During the first prototyping phase, a cable to a test site near Catania at a depth of 2 km was installed and equipped with a junction box. In December 2006, the prototype of one tower containing 16 optical modules arranged at 4 bars was installed and its in-situ tests were performed. Although the data taking period was limited to a few months due to technical problems, the mini-tower provided the proof of concept for the technologies and most of the components employed. A mechanical test tower of limited size was successfully deployed and unfurled in early 2010. The plans to deploy a full-size prototype tower will be pursued in the KM3NeT framework.

The successful operation of the first-generation neutrino telescopes over more than ten years and the sensitivities to natural high- and ultra-high-energy neutrino fluxes achieved in these experiments, which exceed those of the largest underground detectors (Super-Kamiokande, MACRO) approximately by two orders of magnitude, have conclusively proven the efficiency of the method for detecting neutrinos and other elementary particles in natural media. At the same time, the results obtained in experiments on the first-generation neutrino telescopes were the motivation for designing and creating neutrino telescopes with a characteristic scale of the order of cubic kilometer. They will allow the sensitivity to natural neutrino fluxes to be increased by more than an order of magnitude.

At present, three projects of large-scale neutrino telescopes in natural media are being actively developed in the world: IceCube at the South Pole, the Mediterranean KM3NeT, and the Baikal BAIKAL-GVD, which are at different stages of realization.

The successful development of AMANDA convinced the US Government and Congress of the necessity of allocating considerable financial resources (about 300 million US dollars) for creating the IceCube detector with an effective volume of ~ 1 cubic kilometer at the South Pole. IceCube [30, 31] consists of 5160 digital optical modules (DOMs) installed on 86 strings at depths of 1450 to 2450 m. A string carries 60 DOMs with 10-inch photomultipliers Hamamatsu R7081-02 housed in a 13-inch glass sphere. Signals are digitized in the DOM and sent to the surface via copper cables. 320 further DOMs are installed in IceTop, an array of detector stations on the ice surface directly above the strings. There is a high-density sub-array (DeepCore) of six strings at large depths (i.e. in the best ice layer) at the center of IceCube, which allows a threshold less than 10 GeV for muon detection. The first of 86 IceCube strings was deployed at the South Pole in the winter of 2005. The speed with which the array was mounted increased steadily in succeeding years and the detector was deployed in its full configuration in December 2010. With this detector, the idea of a cubic-kilometer detector was finally realized.

The Mediterranean neutrino telescope groups ANTARES, NEMO, and NESTOR are among the main participants of the KM3NeT project on the creation of a cubic-kilometer neutrino telescope in the Mediterranean Sea. The project is funded from the common budget of the EU countries. A design study from 2006 to 2009 resulted in a Conceptual Design Report (CDR) [32] and a Technical Design Report (TDR) [33]. At present, the project is in a Prototyping Phase and envisages installing of two detectors

with total of 6 km³ volume from 2014 on. The final decision on the detector's design and the site of its installation is expected in 2012.

Each of the next-generation telescopes being planned or created at present (IceCube, BAIKAL-GVD, KM3NeT) has certain advantages and disadvantages attributable to its location, the properties of the medium, the complexity of the engineering solutions in creating and operating the array, the cost of creating and maintaining the infrastructure, and the possibility of changing the configuration and increasing the sensitivity of the telescope. In view of their geographical location, the Baikal BAIKAL-GVD and Mediterranean KM3NeT telescopes in the Northern Hemisphere and the IceCube detector at the South Pole will mutually complement each other and will form the Global Neutrino Observatory (GNO) aimed at searching for and investigating neutrino sources on the entire celestial sphere. The detectors in the Northern Hemisphere have an important advantage - they are capable of providing an almost continuous observation of the Galactic center (BAIKAL-GVD about of 18 h and KM3NeT about of 15 h during a day) and the main part of Galactic plane, where the majority of the potential Galactic cosmic-ray sources (pulsars, supernova remnants, binary systems, etc.), including the massive black hole Sgr A* at the Galactic center, are concentrated.

The optical properties of the medium - its optical transparency and intrinsic luminescence background level, as well as its aggressiveness with respect to the structural materials are significant factors in a comparative analysis of various experiments in natural media. The Antarctic ice is characterized by a strong inhomogeneity in depth related to the atmospheric transparency and the conditions of the Antarctic snow cover formation in a period of the order of a hundred thousand years. As a result, at 400 nm the light absorption length in ice at depths from 1500 to 2500 m changes in a wide range from 40 to 150 m, the scattering length changes from 0.4 to 2.4 m, and the asymptotic (propagation) length varies in a range of 10 – 45 m [34]. The optical properties of the Mediterranean deep water are characterized by an absorption length of 50-70 m and a scattering length of ~30-60 m [32]. For the deep water of Lake Baikal, the characteristic absorption and scattering lengths are 22-25 m and 30-50 m, respectively [35]. The light scattering length in the Baikal and Mediterranean water exceeds that in the Antarctic ice by more than an order of magnitude. The depth dependence of the optical properties of ice complicates the analysis of the experimental data. Furthermore, the large delays in photon propagation due to the strong scattering cause worse angular resolution of deep-ice detectors compared to water ones. On the other hand, the large absorption length results in better photon collection.

From the viewpoint of the natural background attributable to the medium's intrinsic luminescence, the IceCube has an undeniable advantage over the deep underwater experiments. In the Antarctic ice, there is virtually no intrinsic luminescence of the medium. In addition, since the deep-ice temperature is extremely low (about -30° -50°C), the PMT dark current is about 300-600 Hz compared to about 15 kHz due to chemiluminescence in Lake Baikal water and about 30 kHz caused by K⁴⁰ decays in Mediterranean Sea. In turn, from the viewpoint of background conditions, the BAIKAL-GVD detector has an advantage over KM3NeT, because, in contrast to the fresh water of Lake Baikal, there is a background in the Mediterranean seawater attributable to bioluminescence processes. E.g. the bioluminescence rate at ANTARES site exhibits a slowly varying baseline of typically a few 10 kHz to a few 100 kHz, and second-scale

bursts in the MHz region. Efficient data taking is possible up to baseline rates of 100 - 200 kHz.

To conclude our comparison of various experiments from the viewpoint of advantages attributable to the medium's properties, we will note that the salt water of the Mediterranean Sea imposes much more stringent requirements on the anticorrosion properties of the structural materials of the elements, components, and supporting structures of the neutrino telescope than the fresh Baikal water and Antarctic ice.

One of the most important factors determining the feasibility of the large-scale neutrino telescope projects is the creation and maintenance of their infrastructure and the complexity of the project's engineering realization. The IceCube project uses the infrastructure of the Amundsen-Scott Antarctic polar station. Maintaining the viability of this station requires a substantial financial expenditure, because it is hard to reach and the climatic conditions at the South Pole are extreme. The telescope deployment technology is based on drilling holes in ice with a depth up to 2500 m using special high-power-input equipment. Drilling one hole requires 5520 gallons or 18 tons of fuel. The freezing of the telescope's optical modules into ice rules out the possibility of extracting and repairing the scientific equipment and changing the telescope's configuration. All these factors determine the project's high cost. In the case of the Mediterranean KM3NeT project, creating the shore infrastructure involves no fundamental difficulties. On the other hand, the deployment and long-term operation of a neutrino telescope deep in the Mediterranean salt water impose more stringent requirements on the reliability of the electronic and communication systems and supporting structures of the telescope and is a difficult and costly engineering task. As a result, the cost of creating the KM3NeT telescope is estimated to be about 220 to 250 million Euros. In contrast to the Antarctic ice, placing a telescope in a sea allows some of the telescope's failed elements and components to be made accessible for repair. This applies mainly to the strings of optical modules that, if necessary, can be disconnected from the bottom anchors and sent to the shore for repair in case of successful surfacing.

The BAIKAL-GVD project suggests using the existing infrastructure of the Baikal Neutrino Observatory of the Institute for Nuclear Research of the Russian Academy of Sciences when creating and operating it. The relief of the Lake's bottom allows the array to be deployed at a distance of 4-6 km from the shore, which is considerably less than the characteristic distances of 25-100 km being discussed for the Mediterranean projects. The presence of a stable ice cover for about two months (from mid-February to mid-April) allows the telescope deployment as well as the repair, maintenance, and research works to be performed directly from the ice using it as a solid and stationary mounting platform. The same features of the Baikal project makes it possible to design a modular architecture of the BAIKAL-GVD telescope, thereby retaining the possibility of increasing its volume by installing additional, functionally independent clusters. Furthermore, under the Baikal conditions, there is a unique (an already tested) opportunity to promptly change the configuration of the deep underwater array by moving the strings to a new position directly under water without their prior lifting and dismantling on the surface.

2 BAIKAL NEUTRINO EXPERIMENT

2.1 Project History

At the suggestion of A.E. Chudakov, supported by M.A. Markov, a start was made on the development of the method for deep-sea neutrino recording in Lake Baikal as a proving ground for testing and constructing the prototypes for future large-scale detectors. We can assume that the Baikal neutrino experiment was initiated on 1 October 1980, when the Institute for Nuclear Research (INR). USSR Academy of Sciences announced its decision to found a Laboratory of High-Energy Neutrino Astrophysics, which later became the core of the Baikal collaboration also including Irkutsk State University, Moscow State University, the Joint Institute for Nuclear Research (Dubna), DESY-Zeuthen Research Center (Germany), Nizhny Novgorod State Technical University, and St. Petersburg State Marine Technical University. The researchers from Tomsk Polytechnical University, the Russian Research Center “Kurchatov Institute”, the Limnology Institute, RAS Siberian Branch, the Academician Andreev Acoustic Institute, and a number of other Russian and foreign (Hungary, Italy, France) institutions also participated in the experiment at some of its stages.

Lake Baikal was chosen as a place for the development of the experimental studies for the following obvious reasons: high transparency (comparable to ocean water transparency) of deep waters; the presence of places with sufficiently steep shore slopes in which a depth of about 1 km, required for protection from penetrating cosmic rays, is located at distances of 4-5 km from the shore; the presence of an ice crust allowing the mounting of deep-sea instruments and laying down cable communications from it for two months per annum, and a low expected level of the intrinsic emission of deep waters caused by bioluminescence and radioactivity. Based on the experience and results of Baikal studies performed for many years by researchers at the Limnology Institute, Siberian Branch of the RAS, a particular site was chosen for starting the work – an area of the lake adjacent to the 106th km of the Krugobaikal railway.

The design of the project, the deployment and startup of the detector were preceded by investigations of experimental hydrooptical, hydrophysical, and hydrological conditions in Baikal, which were performed for about a decade [36,37,38]. In these experiments, an intrinsic emission of deep waters in the lake, which is caused by the oxidation of particles a few micrometers in size, was discovered. This emission is typical of the Baikal bacteria that dominate in amount and of many phyto- and zooplankton species. Deep-sea pilot Cherenkov detectors were installed for long-term operation to try out the method of data acquisition and perform the first physical experiments [15, 39]. The first stationary string of optical modules (OMs), named GIRLANDA-84, was deployed in 1984 and comprised 12 PMTs. The arrangement aimed at detection of atmospheric muons, search for superheavy magnetic monopoles catalyzing baryon decays, as well as investigation of the long-term characteristics of the Baikal water luminescence. This string was connected to the shore by a seven-wire cable which was also deployed in 1984. The total data collection time for GIRLANDA-84 was 50 days. The search for slowly moving, bright objects was continued in 1986 with the Stationary Monopole Search String (SMSS) or GIRLANDA-86 which, in a rearranged configuration (GIRLANDA-86M), also operated in 1987-1988. The combined upper limit on the flux of GUT monopoles catalyzing proton decay was obtained from data collected by GIRLANDA-84, -86 and -86M arrays [15]. Beside to search for monopoles a variety of

methodical questions were investigated with these arrays. For instance, the seasonal variations of the natural luminescence were investigated and found to reach a factor of up to five. Furthermore, coincidences due to atmospheric muons were monitored. These measurements show that the acceptance of the array does not suffer critically large variations, be it due to changing optical parameters of the water or due to sediment accumulation on the optical modules.

Design of the first large-scale deep underwater neutrino telescope NT200 with an effective detection area of $(2-10) \cdot 10^3 \text{ m}^2$ (depending on the particle energy), as well as a wide program of physical studies with it were developed during 1988 – 1992 [40, 41]. The array was deployed stepwise from 1993 to 1998 in Lake Baikal. It was designed on the basis of 192 optical modules (OMs) comprising QUASAR-370 phototube with photocathodes of 370 mm in diameter, exclusively designed for the BAIKAL neutrino experiment [42].

The first stage of the detector was deployed in 1993. It consisted of 36 optical modules arranged at three vertical strings at a depth of about 1100 m, as well as an underwater data acquisition and transmission system, a shore station, a laser based time synchronization system, tools for permanent *in situ* monitoring of water parameters, and acoustic positioning system for measurements of spatial coordinates of the optical modules. The effective area of the array for muons detection was about of 300 m^2 . The setup operated 240 days during the first year and about of $7 \cdot 10^7$ events from atmospheric muons were detected [43]. This array was partly updated in 1994 (the distance between the strings was increased up to 21 m) and operated 242 days in such a configuration. In winter 1994, an additional bottom communication fiber-optic cable was deployed to shore.

In 1995, 36 optical modules were mounted additionally at the detector. During winter 1996, updated high-voltage-proof power supplies of QUASAR-370 phototubes were embedded in most optical modules. To prepare the detector to long-term operation, all telescope rope frames, made of ordinary steel, were replaced by corrosion resisting stainless steel ropes. Mounted during the winter expedition of 1996, the setup included 96 optical modules arranged at four vertical strings (24 optical modules on each of them).

During the winter expedition of 1997, 48 additional optical and 16 electronic modules were mounted on the umbrella-like frame of the NT200 telescope. The resulted number of optical modules thus increased to 144. The setup operated 240 days in the data taking mode. During the winter expedition of 1997, the experiment on light detection of a submerged point source (based on a laser) with photo-sensors of the NT-144 neutrino telescope was carried out. Analysis of data of this experiment allowed to obtain values of water optical parameters for the 480-nm wavelength: an absorption length of (21–23) m and asymptotic attenuation length of (17.0–17.6) m [44]. These results confirmed the applicability and efficiency of the neutrino telescope in medium optical parameters monitoring.

Deployment of the NT200 was completed in 1998, and the first underwater neutrino telescope has been put in operation since April 6, 1998 in a configuration of 192 optical modules composed as eight 68.75 m long vertical strings at a depth of 1100–1200 m. The counting rate was about 14 Hz for atmospheric muons and about one event per two days for atmospheric neutrinos from under the horizon.

A sample of qualitative data, corresponding to 1038 live-days of data taking, was selected from successive operation of the NT200 telescope from April 1998 to February 2003. The sample was used for data analysis in various physical investigations [45-49].

Implementation of the NT200 neutrino telescope project was the first successful attempt of designing a large-scale deep underwater stationary Cherenkov detector. It has opened new prospects in neutrino astrophysical investigations, and becomes the powerful monitoring tool of the Southern Baikal ecosystem.

During NT200 operation in 2002–2004, faults occurred with cable communication system between the detector and shore station. Analysis of these faults showed that they were caused by electrochemical corrosion of the cable sheath in the vicinity of the detector at a depth of about 1100 m. To eliminate this defect, a special polypropylene-sheathed cable was designed and manufactured. The first bottom communication line with the use of this cable was deployed in Lake Baikal in 2004.

The NT200+ neutrino telescope project was proposed in 2002. Along with the NT200 detector, it consists of additional three external strings, located at a distance of 100 m from the NT200 detector and comprising 12 optical modules each. This setup was considered as an intermediate step in designing a cubic-kilometer-scale telescope at Lake Baikal.

The first external string was deployed in 2003, and elements of the time-synchronization system and the data acquisitions system of the NT200+ detector were tested *in situ*. During the winter expedition of 2004, the main efforts were focused on the assembling the second external string of the NT200+ detector and the system of underwater cable communications. New communication line to shore based on the specially designed seven-lead cable with polypropylene cover was deployed. The NT200 detector combined with the external strings by means of the joint control and data acquisition system on the basis of submerged local network of microcomputers was commissioned on April 2004. The underwater part of the control system was almost totally updated, as well as the shore data acquisition and processing center. The use of up-to-date network solutions within the developed system provided for an increase in the data exchange rate between the shore and underwater devices by more than an order of magnitude and allowed reduction of the number of required bottom cable communication lines. The last, third external string was deployed in 2005 and the NT200+ was put in operation in its full configuration. Also a new communication line to shore and new calibrating light source (based on a laser) were deployed.

Update of underwater recording and controlling systems of NT200+ and deployment of new (the fourth) cable to shore have been performed in 2006. As a result, the efficiency of physical event detection by the NT200+ setup was increased by more than 20% in comparison with that in 2005. The effective volume of the NT200+ exceeds 10^7 m^3 for detection of showers with energies of 10 PeV and higher.

The construction of a km^3 -scale neutrino telescope - the Gigaton Volume Detector (GVD) in Lake Baikal - is the central goal of the Baikal collaboration since 2006. The R&D Phase of BAIKAL-GVD project started with the long-term *in situ* test of new optical modules based on Hamamatsu R8055 and R7081-20 PMTs and new controllers of the data acquisition system in 2006-2007. During 2008-2010 years the basic elements of GVD - new optical modules, FADC readout units, underwater communication network and trigger systems - have been developed, produced and tested *in situ* by long-term operating prototype strings in Lake Baikal [50, 51]. The Prototyping Phase of the GVD project has been started in April 2011 with the deployment of a 3-string engineering array (prototype cluster) which comprises all basic elements and systems of the GVD-telescope in Lake Baikal.

2.2 Site Description

The site chosen for the experiment is in the southern basin of Lake Baikal, near the outfall of a small river, named *Ivanovka*, and about 40 km west of the place, where the Angara river leaves the lake. Here combination of hydrological, hydrophysical, and landscape factors is optimal for deployment and operation of the neutrino telescope. The geographical coordinates of the detector site are 51°50' N and 104°20' E.

Quite developed infrastructure in this part of shore was an important factor caused the choice of the telescope site; in particular, this allows railway transportation of goods and scientific equipment.

Lake depth is about 1300–1400 m here at distances beginning from about of three kilometers from the shore. A flat the lake bed throughout several tens of kilometers from the shore allows practically unlimited instrumented water volume for deep underwater Cherenkov detector. A strong up to 1 m thick ice cover from February to the middle of April allows telescope deployment, as well as maintenance and research works directly from the ice surface, using it like a solid and fixed assembling platform. The quality of the ice cover, the absence of stable hummocking fields and backbone slits are determining conditions from the viewpoint of safety equipment assembling and underwater cable lines deployment. The period of safety works is usually longer than 8 weeks. Vanishingly small values of under-ice water currents allow the required precision of the assembling works.

2.3 Optical Properties

The absorption $\alpha(\lambda)$ and scattering $\sigma(\lambda)$ coefficients, the phase scattering function $\chi(\mu, \lambda)$ ($\mu = \cos(\theta)$, θ is the photon scattering angle), and the light propagation velocity in a medium $v(\lambda)$ are the main optical parameters characterizing the propagation of light with the wavelength λ in transparent media. Analysis of long-term measurement data of optical parameters of Lake Baikal deep water shows that the absorption length $L_\alpha = 1/\alpha(\lambda)$ is a quite stable parameter with a characteristic value of 20–24 m in the water transparency window ($\lambda = 480\text{--}500$ nm). Seasonal variations in the absorption length do not usually exceed 20%. In contrast to the absorption length, the Baikal water scattering length $L_s = 1/\sigma(\lambda)$ varies in quite wide limits. Though the characteristic values $L_s = 30\text{--}50$ m in the water transparency window, it varied from 15–20 m to 70 m in certain measurement periods. Long-term monitoring of optical parameters of Lake Baikal water at the neutrino telescope site was carried out with the use of special ASP-15 measuring complex. During the winter expedition of 2001, optical parameters of Baikal water were simultaneously independently measured by the ASP-15 complex and the AC9 device (NEMO collaboration, Italy). Figures 2.3.1 shows the values of absorption length and scattering coefficient of Baikal water measured with different devices in 2001 [35].

The phase scattering function is defined through the differential scattering cross-section:

$$\chi(\mu, \lambda) = \frac{d\sigma}{\sigma d\mu}, \quad \int_{-1}^1 \chi(\mu, \lambda) d\mu = 1.$$

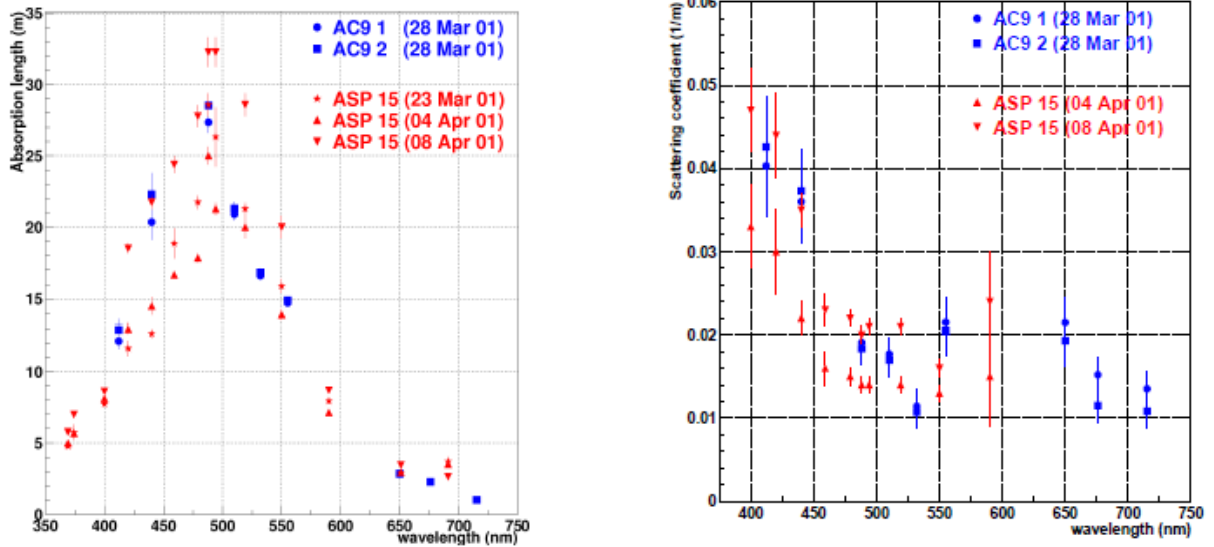


Fig. 2.3.1: Spectral dependence of the absorption length (left) and the scattering coefficient (right) of Baikal water at a depth of 1000 m [35].

The phase scattering function of Baikal deep waters is strongly anisotropic and characterized by an average scattering angle of about 0.86–0.9.

2.4 Baikal Underwater Neutrino Telescope

2.4.1 NT200

The NT200 telescope is located at a depth of about 1100 m at a distance of 3.6 km from the shore. Lake depth at the site is about of 1366 m. It is connected to shore by four copper cables which allow for operation over the full year. The underwater ends of cable communication lines are fasten at buoy stations at a depth of about 25 m from the lake surface and connected with the telescope central electronic unit (CEM) by means of cable jumpers. All the connections are made on dry from the ice cover of the lake. Such an approach allows the assembling without complicated and expensive equipment for connecting cable communication lines deep under water.

The neutrino telescope is a 3D-array of optical modules (OMs) arranged on vertical carrying cables, bottom ends of which are fasten to anchors, and the upper ones, to buoys. Each vertical cable with optical modules forms a structure unit of the telescope - a string of optical modules. The telescope contains 192 OMs, assembled on 8 strings, each 68.75 m long. The central string is surrounded by peripheral strings which are located uniformly on a circle 21.5 m in radius and attached to an umbrella-like rigid frame (Fig. 2.4.1).

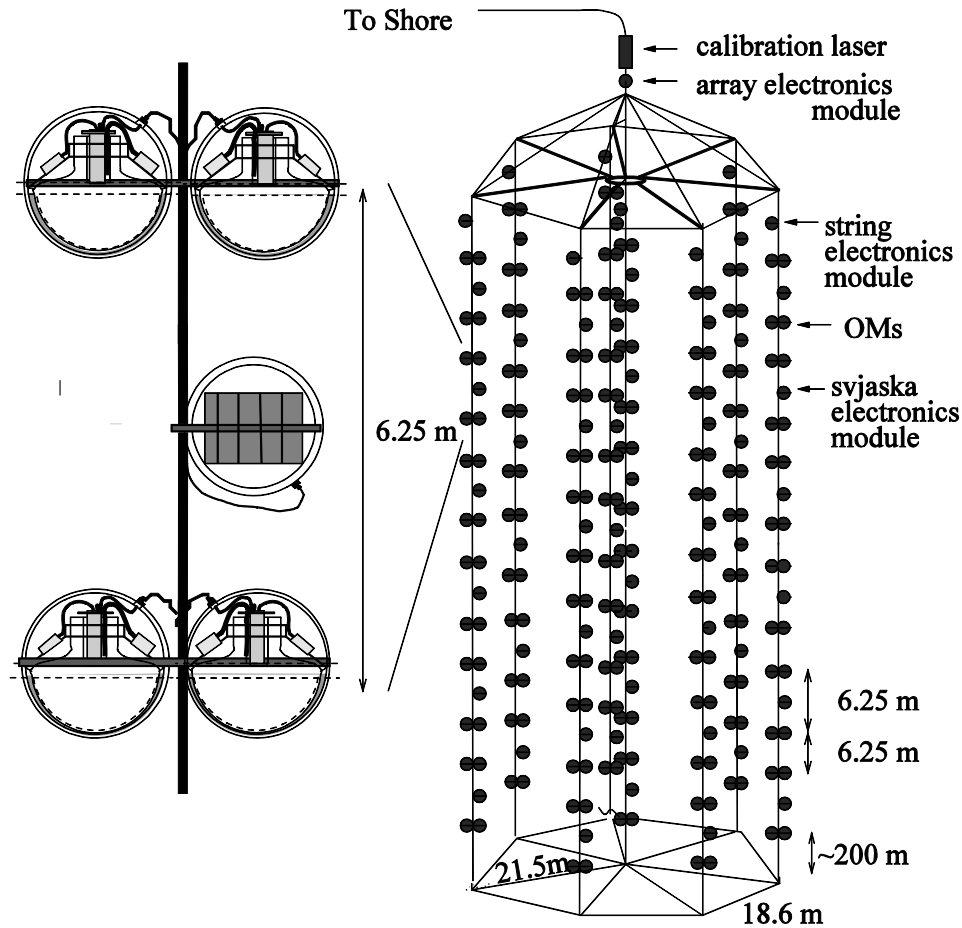


Fig. 2.4.1: A schematic view of the NT200. The left-hand expansion shows two pairs of optical modules (svjaska) with the svjaska electronics module, which houses part of the readout and control electronics.

Each string comprises 24 OMs which are grouped pair-wise along a string. In order to suppress accidental hits from dark noise (about 30 kHz) and luminescence of the medium (typically 50 kHz but seasonally raising up to hundreds of kHz), the two photomultipliers of a pair are switched in coincidence, defining a *detecting channel*, with typically only 0.25 kHz noise rate. Two pairs of OMs have a common electronic system module (SM) and form a functional unit of a string - a *svjazka* (which is the Russian word for “bundle” or “connection”). All OMs face downward, with the exception of the second and eleventh pairs on each string which face upward. The distance between the first and second and tenth and eleventh *detecting channels* is 7.5 m, between the second and third and eleventh and twelfth *detecting channels* is 5.0 m, and between all other contiguous *channels* is 6.25 m. The time of the first triggered OM of the *channel* is chosen as the signal time stamp. The amplitude of one of the OMs chosen beforehand based on the calibration of the telescope’s measuring systems is used as the *detecting channel* amplitude.

The position of the array is monitored by a hydro-acoustical positioning system. The signals of several ultrasonic emitters placed at radial distances of 600 m with respect to the telescope are recorded by receivers arranged at the strings. This system allows the determination of the OMs positions with an accuracy of better than 20 cm. A special string at a distance of 120 m to the telescope carries devices to measure the optical parameters, the temperature and the pressure of the water.

An optical module is a key element of the telescope. It consists of a pressure resistant glass spheres equipped with QUASAR-370 phototube, attendant electronics, HV supply units, as well as calibration LED. The QUASAR-370 is a hybrid device [42]. Photoelectrons from a large hemispherical cathode (K2CsSb) with $> 2\pi$ viewing angle are accelerated by 25 kV to a fast, high-gain scintillator which is placed near the center of the glass bulb. The light from the scintillator is read out by a small conventional photomultiplier (PMT). One photo-electron from the hemispherical photocathode yields typically 20 photoelectrons in the conventional photomultiplier. This high multiplication factor results in an excellent single electron resolution of about 70%. Furthermore, the QUASAR-370 is characterized by a small time jitter (2 ns) and a small sensitivity to the Earth's magnetic field. Signals from the PMT anode are fed to the fast preamplifier with the amplification coefficient equal to 10 and used for measurements of PMT response time. Signals from the 11th dynode come to the amplitude measurement system through the amplifier with the amplification coefficient equal to 3.

The underwater electronics consists of the front-end electronics and the systems which carry out the time and amplitude measurement, formation of the master trigger on relativistic particles, selection of candidates for slowly moving particles, data transmission, slow control and power supply. These systems are mounted in the OMs, in the system modules (SM), in the string electronic modules (SEM) and in the central electronic module (CEM).

Each optical module is connected with corresponding system electronic module (SM) with four coaxial cables for power supply and control, PMT's anode and dynode signal transfer, and calibration LED control. In the SM, the PMT signals are discriminated, shaped and checked for coincidence in a 15 ns time window. In the case of coincidence, a semi-digital pulse is formed (*local trigger*), which carries the time (leading edge) and amplitude (width) information of hit *channel*.

The next level in the functional hierarchy of electronics systems is formed by the string electronic modules. The SEM electronics is arranged in two spheres. Each of the two identical parts (semi-SEMs) serves 3 SMs (i.e. 6 PMT pairs). The SEM electronics receives the *local triggers* from every PMT pair and digitizes both its leading edge and width. The leading edge of a *local trigger* is used to form a request signal sent to the central electronic module (CEM), into the scheme forming the *master trigger*. Also, the request signals are fed into the system of slow particle identification. This system responds to particles with velocities of $10^{-5} < v < 10^{-2}c$. The data transmission system at the SEM-level manages the transfer of the data collected in the SEM buffers to the CEM. The string controller connects the SEM with the shore station.

Central electronic module (CEM) comprises the module forming the *master trigger* (≥ 3 *local triggers* within a 500 ns time window), the system which receives SEM information and transmits it to shore (CEM level of the data transmission system), the system of “coarse” time and event counter, and the CEM-controller. The *master trigger* is fed to all digitizers in the SEMs, where it is used as a *stop* pulse in the time measurement system. Furthermore, it increments the event counters in all SEMs. The event number is essential for event building in the on-line computer. The information from the time and charge digitization and from the SEM event counters is transmitted from the SEMs to buffers in the CEM; from there, together with CEM event counter status and “coarse” time, it is sent via the transmission system to the shore data acquisition and control center.

2.4.2 NT200+

To improve the detection efficiency of high-energy neutrinos, the NT200 telescope was upgraded in 2004–2005. The new setup was called NT200+ and provided for both an increase in the effective volume for detecting neutrino induced cascades and a significant increase in the energy resolution of the telescope in general. Last but not least the NT200+ was exploited as an initial prototype version of a structure unit (cluster) of the future km³-scale neutrino telescope in Lake Baikal.

The NT200+ in final configuration was commissioned in April 9, 2005. It consists of the central part (NT200 array) and three external strings (NT+) 100 m away from the central part of the telescope (Fig. 2.4.2). Each external string comprises 12 OMs, which are grouped pair-wise along a string. Two OMs of a pair are switched in coincidence, defining a *detecting channel*, similar to OMs of the NT200. The distance between the lower and upper pairs of OMs is 140 m. The upper *channels* of the external strings are located at the same depth that the lower *channels* of the NT200. The distances between channels of the external strings are 20, 50, 20, 40, and 20 m, counting from the upper channel. All OMs are faced downward, except OMs of two bottom pairs on each string, which are faced upward. Each external string also comprises a LED-calibration system (LED), light signals from which are transferred via individual optical fibers to all OMs of the string.

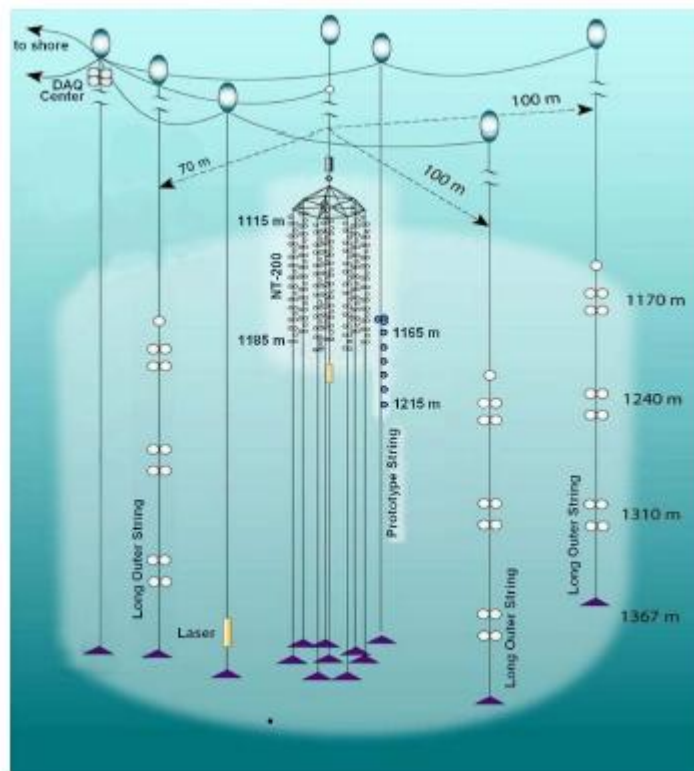


Fig. 2.4.2: NT200+ detector.

To integrate NT200 and external strings into one NT200+ detector, it was necessary to solve two basic problems, i.e., update of the control and data acquisition system of external strings and time synchronization between certain parts of the setup accurate to several nanoseconds. Simple duplication of the control and data acquisition

system for NT200 and external strings was incompatible with both the number of available cables connecting the detector with the shore, and plans of future upgrade of the setup. It was decided to change the system architecture in general. Industrial DSL modems (Ethernet network) and submerged single-board industrial computers were used for the first time. All cable communications of the NT200+ control and data acquisition system commutate via the central communication unit (DAQ center), located at a depth of 30 m. The DAQ center provides for data flow conjunction and transmission of all the received information to the shore center.

The electronic systems of the external strings mainly repeat the NT200 systems in the design and operation principle. Two pairs of OMs have a common electronic system module (SM) and form a functional unit of an external string - *a svjazka*. Information on the response times and amplitude (*local trigger*) of each hit *detecting channel* is transmitted from SMs to the string electronic module (SEM).

The optical modules (OMs), system modules (SMs), and string electronic modules (SEMs) of external strings are completely identical to those of NT200. However, the SEM controller electronics required significant update. Each measuring channel comprises an 11-bit TDC, a 10-bit ADC, and an event number record circuit. The principle of operation of the TDC is based on prolongation of the time interval between the START (*channel request*) and the STOP signals (*string request*). The TDC resolution is equal to 2 ns. The *string request* signal is formed by the SEM under condition of double coincidence of the *channel request* signals within a time window of 0.5 μ s. *Request signals* of all external strings are transferred to the DAQ center. In the DAQ center, a *master trigger* is formed and returned to all external strings with a delay of about 11 μ s, ensuring synchronization of their work.

In the presence of a *master trigger*, data from external strings are transmitted into the DAQ center via an Ethernet channels based on DSL modems. The need for modems is caused by a large distance between the external strings and the DAQ center (1.2 km). Three DSL modems, receiving data from the strings, are mounted in one glass sphere.

Data are transmitted to the shore under the control of two submerged computers of the DAQ center, placed in two underwater glass spheres. The electronics of the spheres are almost identical. Each sphere contains a PC/104 single-board computer, an Ethernet-controlled DSL modem, and a modem for string equipment control. Data are transmitted to shore via the DSL modem with a speed of up to 2 Mb/s.

2.5 Brief Review of NT200 Scientific Results

The Baikal underwater neutrino telescope is one of the three largest high-energy neutrino detectors (along with the IceCube at the South Pole, and the underwater ANTARES detector in the Mediterranean Sea). The important results of the first stage of Baikal project investigations obtained with intermediate setups between 1980 and 1998 concerned both the study of the parameters of detectors and atmospheric muon fluxes, the selection of events produced by neutrinos, and the search for magnetic monopoles. The upper limit on the flux of super-heavy magnetic monopoles was derived from the catalysis of barion decay, which was at that time one of the strongest theoretical and experimental restrictions [15]. In experiments with the NT36 and NT96 detectors, the first neutrino events were recorded and one of the strongest restrictions on the additional muon flux caused by the annihilation of dark matter particles (neutralinos) at Earth's center was established [52]. In addition, the limit on the high-energy (above 10 TeV)

diffuse neutrino flux was derived [53]. The limits for the value of natural flux of magnetic monopoles, moving with the velocities $v/c > 0.8$, were also found at a world's best level [54].

The most important results were obtained by analysis of data collected with NT200 since 1998. The analysis of these data has allowed new restrictions (one of the strongest at present) on the intensity of the natural flux of fast ($v/c > 0.8$) magnetic monopoles, $4.6 \cdot 10^{-17} \text{ cm}^{-2} \text{ s}^{-1} \text{ sr}^{-1}$ (for $v/c = 1$) [47], on muon fluxes accompanying the annihilation of dark matter particles (neutralino) at Earth's center [48], $4.2 \cdot 10^{-15} \text{ cm}^{-2} \text{ s}^{-1}$, and at the Sun's center [49], $3 \cdot 10^3 \text{ km}^{-2} \text{ yr}^{-1}$, in the region of neutralino masses above 500 GeV, on the neutrino flux from gamma-ray bursts in the energy range up to 10^7 GeV [46], on the neutrino fluxes from local Galactic sources located in the Southern Celestial Hemisphere depending on the declination at a level of $E^2 F < 5 \cdot 10^{-10} \text{ TeV cm}^{-2} \text{ s}^{-1}$, and, finally, the limit on the diffuse neutrino flux, which is $E^2 F < 2.9 \cdot 10^{-7} \text{ GeV cm}^{-2} \text{ s}^{-1} \text{ sr}^{-1}$ for total flux of all neutrino flavors in the energy range from $2 \cdot 10^4$ GeV to $2 \cdot 10^7$ GeV and lies in the region of theoretically predicted values [45]. In addition, the limit $F < 3.3 \cdot 10^{-20} \text{ cm}^{-2} \text{ s}^{-1} \text{ sr}^{-1} \text{ GeV}^{-1}$ on the electron antineutrino flux in the region of the $6.3 \cdot 10^6$ GeV – resonance was derived [55].

The fortunate combination of natural factors along with the well-studied place for experimentation and the experience acquired in the deployment and operation of the first-generation NT200/NT200+ neutrino telescope provided the required prerequisites for the beginning of work on the designing construction of the deep-underwater Baikal GVD neutrino telescope.

3 CONFIGURATION OF the BAIKAL-GVD

3.1 Concept of Design

The second-stage neutrino telescope BAIKAL-GVD in Lake Baikal will be a research infrastructure aimed mainly at studying natural neutrino fluxes by recording the Cherenkov radiation of the secondary muons and showers generated in neutrino interactions.

The concept of BAIKAL-GVD is based on a number of evident requirements to the design and architecture of the recording system of the new array: the utmost use of the advantages of array deployment from the ice cover of Lake Baikal, the extendability of the facility and provision of its effective operation even in the first stage of deployment, and the possibility of implementing different versions of arrangement and spatial distribution of light detectors within the same measuring system.

With all above requirements taken into account, the following conceptual design of GVD has been developed. The Data Acquisition System of GVD is formed from three basic building blocks: optical modules, *sections* of OMs and *clusters* of strings. The OM consists of a photomultiplier tube (PMT) with large hemispherical photocathode and attendant electronics, which are placed in pressure-resistant glass sphere. The OMs are arranged on vertical load-carrying cables to form strings. Optical modules of each string are grouped into two, three or four sections. A section is a basic detection unit (DU) of array. Each section consists of 12 – 16 OMs and the central module (CM). PMT signals from all OMs of a section are transmitted to the CM, where they are digitized by ADC boards. The CM consists of ADC boards, an OM slow-control unit, and a Master board. The digitized signals from each ADC are transferred to a FPGA which handles the data. A memory buffer allows for accumulating the waveform data from the ADC. An ADC trigger request channel includes a request builder, which forms the request signals to the trigger logic, which are transferred to the Master board. The Master board provides trigger logic, data readout from ADC boards, connection via local Ethernet to the cluster DAQ center, and control of the section operation. The request analyzer forms the section trigger request (local trigger) on the basis of requests from ADC channels. The section trigger request is transferred to the cluster DAQ center.

The cluster DAQ center is placed near the water surface. It provides the string triggering, power supply control, and communication to shore. The organizations of central and section trigger systems are the same. The section local triggers come to inputs of the central ADC board. The central Master board works out the global trigger for all sections. The global trigger produces the stop signal for all ADC channels and initiates waveform information readout. Waveform information is accumulated in the event buffer and then transmitted via an Ethernet connection to the cluster DAQ center. The cluster DAQ center is connected to shore station by an about 6 km long electro-optical cable.

Each BAIKAL-GVD cluster is a functionally complete and independent sub-array, which can operate both as a part of unified configuration and autonomously. This allows for easy upgrade of array configuration, as well as put in operation its individual parts within the telescope deployment phase.

3.2 Optimization of GVD Configuration

The objective of the optimization of the GVD configuration is to provide a large cascade detection volume with the condition of also effectively recording high-energy muons. The choice of the optimal configuration, as well as the estimation of the GVD sensitivity and resolution is based on the results of full-scale simulation of the telescope response to the Cherenkov radiation of muons and showers. An extensive code library has been used to perform this simulation, which includes both codes for simulating the propagation of Cherenkov radiation in water and the response of neutrino telescope light sensors to this radiation, as well as the codes for muon and shower induced event reconstruction.

The MC-optimization for the km³-scale detector configuration was performed for 96 strings grouped in 12 clusters with 192 OMs each. The total number of OMs was 2304. Optical modules contain photomultipliers Hamamatsu-7081HQE with photocathode diameter of 10 inch and high quantum efficiency of 35%. Coincidences of any neighboring OMs on a string (thresholds 0.5 and 3 ph. el.) were used as an initial trigger condition. Basic parameters for optimization were:

- h - the vertical distance between optical modules on each string,
- R - the distance between the central and peripheral strings of cluster,
- H - the distance between the central strings of neighboring clusters.

The simulation scenario was as follows. The muon or shower energy, arrival direction, and coordinates were simulated in the first stage. In the next stage, the propagation of Cherenkov photons from the source to the photo-sensors was simulated taking into account the absorption and scattering of light in water. Furthermore, the response of the optical module to Cherenkov radiation was simulated taking into account the quantum and angular sensitivity of the photo-sensors. When the telescope response satisfied the appropriate trigger conditions, the information about an event was retained in the database. After simulating a statistically significant number of events, the effective area (for muons) or effective volume (for showers) was calculated. This procedure was performed for a wide set of telescope configurations with different values of optimization parameters. The optimal telescope configuration was chosen by comparing the obtained values of the muon effective area and the shower effective volume.

3.2.1 Muons

In case of muons at least six hit OMs on at least three strings (6/3 condition) were required for event selection. This condition allows to achieve full spatial reconstruction of muon track. The calculations were performed for configurations with the following values of parameters:

- the distance between optical modules in a string, $h = 15$ and 20 m;
- the distance between the central and peripheral strings of cluster, $R = 40, 60, 80, 100,$ and 120 m;
- the distance between the central strings of neighboring clusters, $H=150, 200, 250$ and 300 m.

The muon arrival direction was simulated uniformly within the lower hemisphere. The simulation area for a given direction was determined by the largest detection distance for a muon with a specified energy by one optical module. The onset of muon trajectory tracing, i.e., simulation of the showers generated along the muon track, was also determined by the largest detection distance at the highest possible shower energy.

Fig. 3.2.1 shows the dependence of effective area, averaged over the arrival directions of 10 TeV muons on the parameters of optimization. As can be seen in the figure, the preferred telescope configuration is that characterized by a cluster radius $R=40$ m. However, this configuration does not satisfy the technical requirements to the telescope deployment: the distances between the strings are too small in this case and may lead to their crisscross and meshing during annual operation.

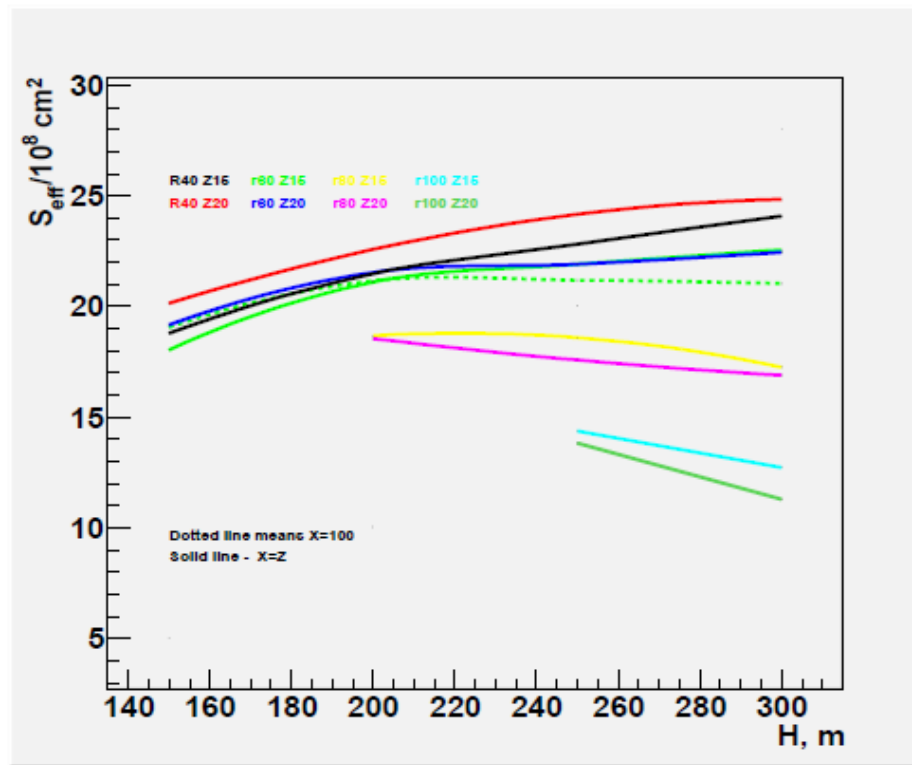


Fig. 3.2.1: Dependence of the muon effective area on the parameters of optimization.

Strings 1300 m long, spaced by only 40 m, can be meshed under bad weather conditions on the lake surface. And, since the difference in the effective muon detection areas for telescope configurations with cluster radii of 40 m and 60 m is rather small, the configuration with the cluster radius $R = 60$ m was chosen as most favorable for muon detection. The muon effective area weakly depends on the values of h and H parameters for given fixed value of R . Figure 3.2.2 shows the energy dependences of muon effective areas for different configurations. As can be seen in this figure, an increase in the cluster radius, as well as in the distance between modules reduces significantly the effective area at low energies. At high muon energies the effective area weakly depends on the variation in the aforementioned parameters of the telescope configuration.

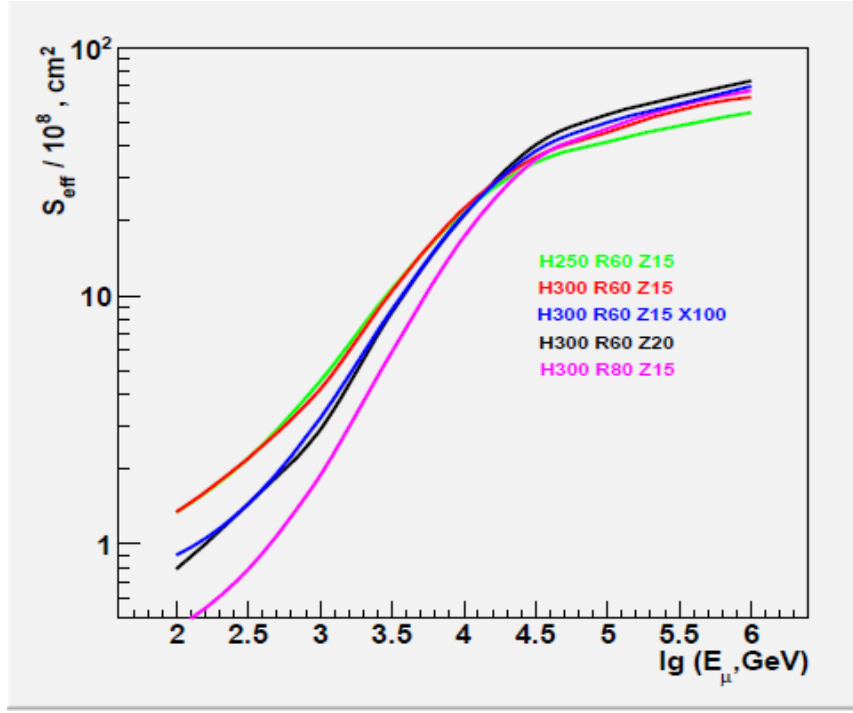


Fig. 3.2.2: GVD (2304 OMs) effective area for muon detection.

3.2.2 Showers

In case of showers at least ten hit OMs on at least three strings (10/3 condition) were required for event selection. To study the dependence of the effective detection volume for high-energy shower on the optimization parameters, we simulated the responses of different telescope configurations. These configurations differed in the geometric parameters, which could take the following values:

- the distance between optical modules in a string, $h = 15$ and 20 m;
- the distance between the central and peripheral strings of cluster, $R = 60, 80, 100$ and 120 m;
- the distance between the central strings of neighboring clusters, $H=200, 250$ and 300 m.

The shower energy was chosen from a wide range of 10^4 - 10^9 GeV. The shower directions were simulated according to the isotropic distribution. The shower coordinates were simulated uniformly in a volume of about 1 km^3 , in the center of which the telescope was located. Total of $4.4 \cdot 10^6$ events were simulated for each configuration.

It was shown, that shower effective volume weakly depends on values of h and R parameters of optimization. Figures 3.2.3 - 3.2.4 illustrate obtained results. Figure 3.2.3 (left panel) shows, as an example, the energy dependence of effective volumes for two configurations with the values $h=15$ m and $h=20$ m and fixed values of $R=60$ m and $H=300$ m. These distributions have similar behavior depending on the shower energy and differ by no more than 15%. The energy distributions of effective volumes for two configurations with the values $R=60$ m and $R=80$ m and fixed values of $h=15$ m and $H=300$ m are shown in Fig. 3.2.3 (right panel). In the energy range above 100 TeV these distributions are very similar.

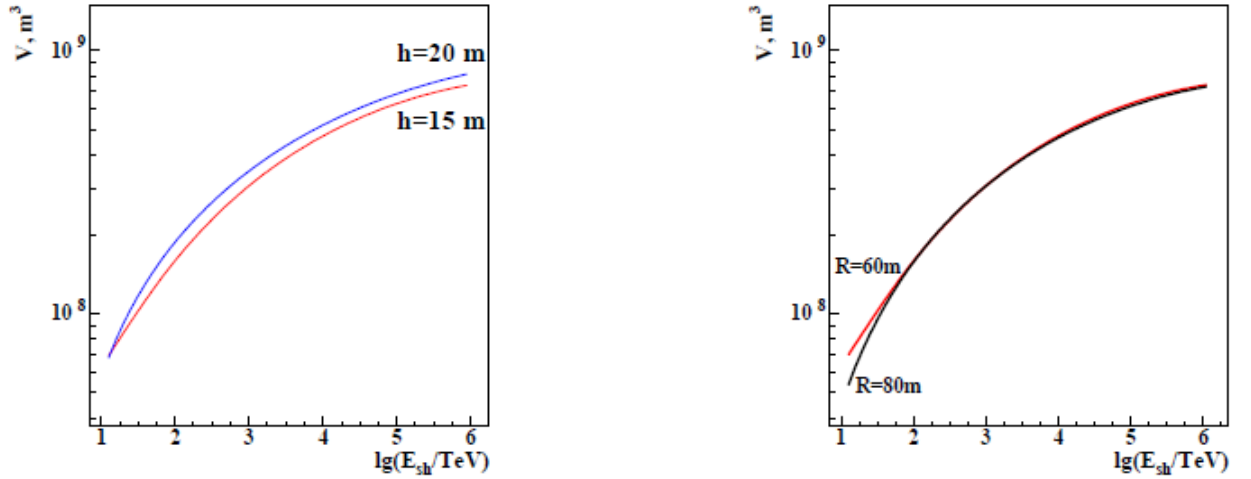


Fig. 3.2.3: Energy dependence of shower effective volumes for different configurations (2304 OMs). Left panel: the upper and lower curves correspond to the distances between optical modules $h=20$ and 15 m, respectively ($R=60$ m and $H=300$ m for both configurations). Right panel: effective volumes for configurations with $R = 60$ and 80 m ($h=15$ m and $H=300$ m for both configurations).

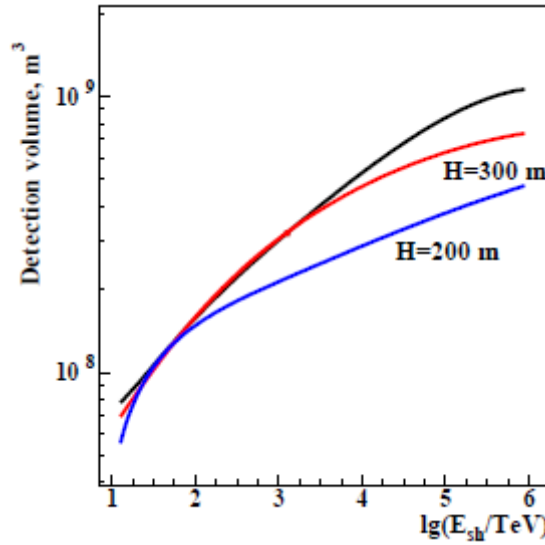


Fig. 3.2.4: Energy dependence of the shower effective volume (2304 OMs). The upper curve corresponds to the configuration with clusters spaced by infinity and the intermediate and lower curves are for the configurations with $H = 300$ and 200 m, respectively.

A comparison of the modeling results for different configurations indicates a significant dependence of the shower effective volume on the distance between neighboring clusters of the array. Figure 3.2.4 shows the energy dependence of the effective volumes for three configurations with fixed values of $h=15$ m and $R=60$ m and different values of H . The upper curve corresponds to the case where the effective volumes of individual telescope clusters do not intersect, the intermediate curve corresponds to the configuration with $H = 300$ m, and the lower curve is for the configuration with $H = 200$ m. The degree of influence of the parameter H on the effective volume increases with an increase in the shower energy. At energies above 10

PeV the effective volumes of the configurations with $H = 200$ m and $H = 300$ m differ by a factor of 1.5.

3.3 Configuration

Based on the results of optimization analysis the compromise between shower effective volume and muon effective area was obtained for the following values of the parameters: the distance $h = 15$ m between optical modules on each string, the distance $R = 60$ m between the central and peripheral strings of each cluster, and the distance $H = 300$ m between the central strings of neighboring clusters. The GVD configuration (see, Fig. 3.3.1) with total of 2304 OMs combined in 12 clusters and chosen values of parameters provides an effective shower detection volume (10/3 condition) of about 0.1--0.7 km³ above 30 TeV and effective area for muons (6/3 condition) which rises from 0.1 km² at 3 TeV to 0.8 km² asymptotically.

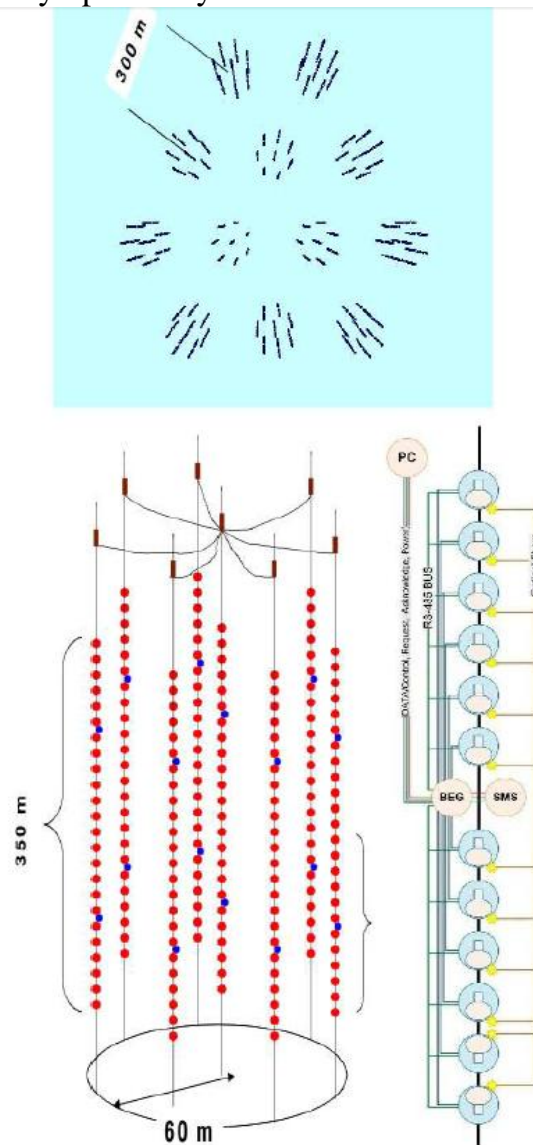


Fig. 3.3.1: GVD design (total of 2304 OMs): GVD top view (12 clusters); schematic view of cluster (eight strings with two sections each); and a section of OMs (12 OMs with PMTs R7081HQE).

4 BASIC ELEMENTS AND ELECTRONIC SYSTEMS

4.1 Optical Module

The basic measuring units of the BAIKAL-GVD are optical modules (OMs), which are design to convert the Cherenkov radiation of muons and showers into electric signals. An OM consists of the following elements: a photo-multiplier tube (PMT), a controller, an amplifier, LED calibration unit, and a high-voltage converter. The OM block scheme is shown in Fig. 4.1.1.

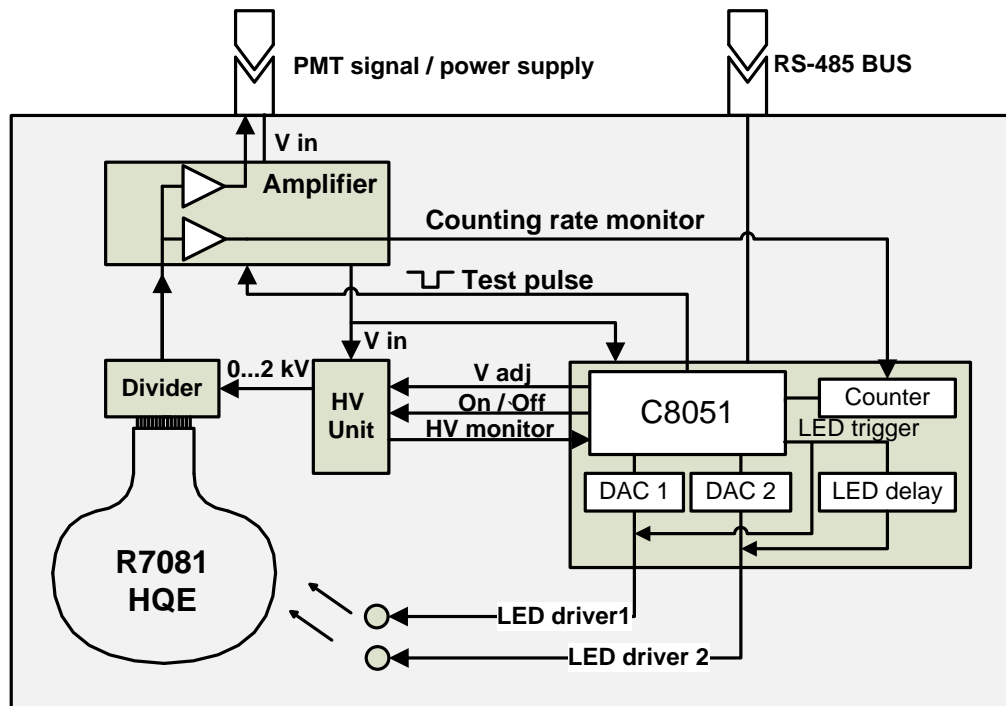


Fig. 4.1.1: Block diagram of optical module.

4.1.1 Photomultiplier tube

The choice of the optimal type of photomultiplier tube for the BAIKAL-GVD is a top priority task. The main requirements to PMT are high time resolution (at a level of several nanoseconds), large photocathode area, and high quantum efficiency. Currently, only Hamamatsu-R8055 and Hamamatsu-R7081HQE PMTs with hemispherical photocathodes satisfy the requirements of the BAIKAL-GVD experiment. PMTs R8055 and R7081HQE have, respectively, the following characteristics: the photocathode area $\sim 1000 \text{ cm}^2$ and $\sim 500 \text{ cm}^2$ and the quantum efficiency ~ 0.2 and more than 0.3 . PMTs of both types were tested as components of engineering arrays in Lake Baikal. At present R7081HQE is chosen as a light sensor of the BAIKAL-GVD (see Fig 4.1.1). The photomultiplier is fed by a high-voltage TRACO POWER SHV12-2.0K1000P DC/DC converter through a voltage divider with a resistance of $18 \text{ M}\Omega$. Working voltage from the range $1300 - 1800 \text{ V}$ is selected to provide a gain of the dynode PMT system of $\sim 10^7$.

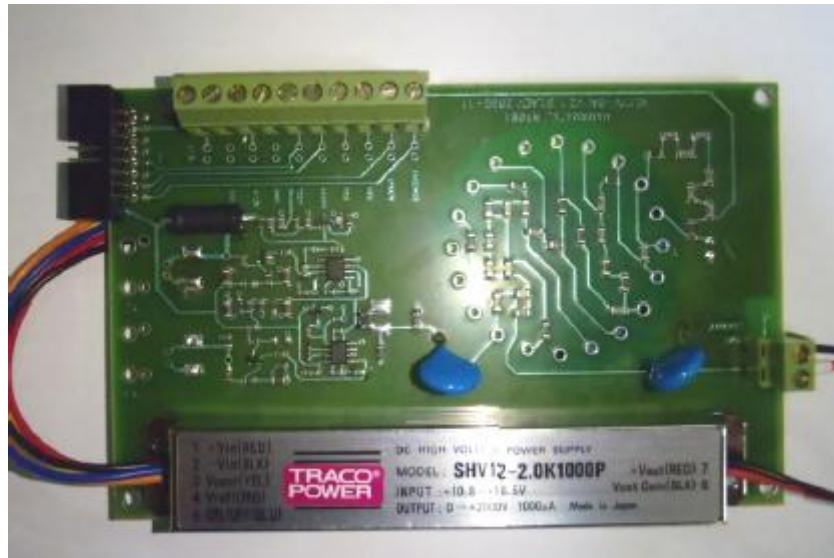


Fig. 4.1.2: Amplifier/divider board with a mounted high-voltage power supply.

To provide reliable operation of the spectrometric channels of the telescope, the PMT signal is additionally amplified by a factor of 12 (the first amplifier channel). This amplification level provides both a sufficiently high average single-electron PMT signal (30-40 mV) with respect to the noise pulse amplitude in the spectrometric channel and the necessary range of linearity up to 100 photoelectrons (p.e.). Two-channel amplifier unit and PMT voltage divider are placed on the same board. The first amplifier channel is used for spectrometric measurements and the second channel (amplification factor 25) serves to amplify signals arriving at the noise pulse counter of the photomultiplier. The amplifier/divider board is shown in Fig. 4.1.2.

4.1.2 Controller

The optical module is controlled through a deep underwater bus RS-485 with the aid of a controller specially developed for BAIKAL-GVD based on a C8051F124 processor (see Fig. 4.1.3). The main functions of the controller are as follows:

- adjustment of the PMT high voltage;
- amplitude and time calibration of channels using LED light sources;
- monitoring the basic parameters of the PMTs and electronics during long-term operation.

The working PMT voltage is set using the control input of SHV12-2.0K1000P DC/DC converter. The control voltage is formed by a digital-to-analog converter (DAC) of the controller in the range of 0 - 2.5 V with a step of ~1 mV. As a result, the working PMT voltage can be set with an accuracy of about ~0.5%.

The amplitude and time calibrations of the photomultiplier were performed using two Kingbright L7113 PBC-A LEDs. The LED brightness is highest at a wavelength of 445 nm, and the light pulse duration is about 5 ns. The controller provides precise control of the LED intensity and adjusts the delay between their signals. The LED intensity varies from 1 to $\sim 10^8$ photons per flash. Delay time between two LED's pulses may be

varied in the range up to 1000 ns with the step of 100 ns and the precision better than 1 ns. The effect of mutual influence of two LED does not exceed 0.5%.



Fig. 4.1.3: Optical module controller.

The control of the PMT and OM electronics operation implies continuous monitoring of their main parameters and operation conditions. The controlled PMT parameters are the high voltage value, the phototube transit time, and the rate of PMT intrinsic noise. To inspect the high voltage, the PMT divider is equipped with a monitor output, the voltage at which is proportional to the total voltage across the divider. This voltage is measured by an analog-to-digital converter (ADC) of the OM controller. The technique of monitoring the PMT transit time is based on measuring the time interval between the LED triggering signal and the LED signal detected by the PMT. In mode of measuring PMT transit time the signal coinciding in time with the triggering signal is applied to the output cascade of the amplifier in the OM spectrometric channel. As a result, two signals are formed and the time between them is determined by the PMT transit time. This time interval is measured on the central module (CEM) of the section with an accuracy of about 2 ns. Note that the possibility of forced signal formation at the OM output is also used to monitor the operating performance of the section as a whole, without applying a high voltage across photomultipliers.

The PMT intrinsic noise rate is measured using the second channel of the amplifier (with a gain ~ 25), the signal from which is provided to the pulse counter of the OM controller (Fig. 4.1.1). The width of time window for noise rate measurement can be set in the range from several milliseconds to 10 s, depending on the PMT operation mode. The counter detection threshold can be controlled from 0.2 up to 100 p.e.: the lowest operating threshold is limited by the noise level of the OM electronics.

To monitor the external conditions of OM electronics operation, the controller allows one to measure the temperature and power supply voltages. A power supply voltage of 12 V is fed to the optical module through the same wire through which the PMT signal is transferred. The aggregation of power supply with the spectrometric

channel simplifies significantly the system of deep underwater cable communications of BAIKAL-GVD section. However, this configuration increases the noise in the spectrometric channel to 10-15 mV because of the power supply unit intrinsic noise. The OM current consumption at a voltage of 12 V is 200 mA; the controller contribution is ~80 mA.

4.1.3 Design of optical module

The optical module design is shown in Fig. 4.1.4. The OM electronic components are placed in a pressure-resistant VITROVEX glass sphere 42 cm in diameter, which consists of two hemispheres. To fix reliably the hemispheres, the optical module is evacuated to a pressure of about 0.7 atm.

The photomultiplier is glued into one of the hemispheres using silicon elastic gel, which provides an optical contact between the PMT and the sphere glasses. To reduce the influence of the terrestrial magnetic field, the PMT photocathode is enclosed in a mu-metal wire cage. The controller, amplifier, and high-voltage converter are mounted on the PMT base. Drivers equipped with LEDs are connected to the OM controller through high-frequency SMA connectors.



Fig. 4.1.4: Optical module with an R7081HQE PMT, protective mu-metal cage, and electronics kit.

The light from LEDs arrives at the center of the PMT photocathode through optical fibers 0.5 m long. The amplified PMT signal is extracted from the module through a deep underwater coaxial connector CP-50-862/8b3. The OM power supply is fed through the same connector. The slow control bus RS-485 is also led into the OM through the CP-50-862/8b3 connector. A vacuum valve is placed on the sphere near the two connectors, and a manometer is connected to it for monitoring the pressure in the OM.

4.1.4 Angular sensitivity of OM

The information about the angular dependence of the optical module response to Cherenkov radiation is of primary importance for simulating the processes of muon and shower detection in the BAIKAL-GVD. The angular sensitivities were measured for selected OM samples using a diffuse light source with a wavelength of 445 nm, mounted at a distance of 2.5 m from the optical module. The optical module under study was placed in a water-filled tank. Figure 4.1.5 presents the results of measuring the angular sensitivities of OMs based on PMT R8055, XP1807 (Photonis), and R7081HQE.

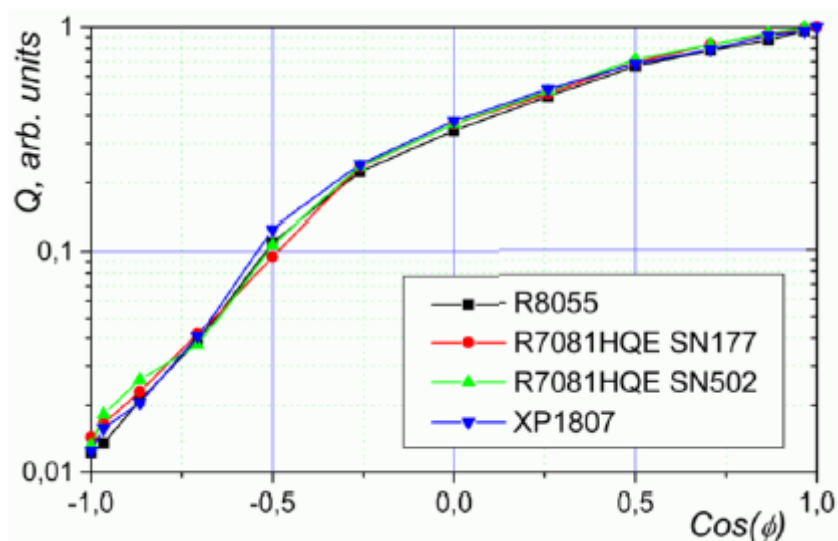


Fig. 4.1.5: Relative angular sensitivity of OMs based on R8055, XP1807, and R7081HQE PMTs.

4.2 Section - Detection Unit of the BAIKAL-GVD

Optical modules are mounted on vertical load-carrying cables to form strings. A low level data collecting unit of a string is a section of optical modules. Each section contains 12 OMs, a central module (CEM), and a service module (SM). The section functional scheme is shown in Fig. 4.2.1. The central module collects and transfers data and controls the section electronics operation. Analog signals from optical modules arrive at CEM through coaxial cables 90 m long. Digitization of the PMT signal is performed in a 15- μ s window by three boards of four-channel 12-bit ADC (FADC) with a discretization frequency of 200 MHz. Waveform stamp of events are formed in the channels, the analysis of which makes it possible to determine the amplitude and detection time of OM signals. Two ring buffers are provided in each channel to record signal waveform with dead time minimized. Along with the conversion of analog signals and intermediate data storage, the ADC boards form the so-called channel *request* signals. A *request* signal is formed when the input signal amplitude exceeds the specified threshold. The threshold function is implemented on digital comparators (two comparators per channel). The comparator thresholds are controlled with a step of ~ 1.4 mV. *Request* signals from all ADC channels arrive at the *Master* board, which forms a section *request*. This signal is formed when the *request* signals from the section channels

fulfill specified conditions. The information about the allowed combinations of the signals is loaded dynamically into the *Master* board memory (the so-called coincidence matrix is formed). The *request* signals of sections are transferred to the cluster center through coaxial cables ~1200 m long. A *acknowledge* signal is formed in the cluster center; it serves as a global trigger for all sections and provides their synchronous operation. This signal initiates readout of the data of all ADC channels and their transfer to the data acquisition center of the cluster (DAQ-center), which is in turn connected with the shore station through an electro-optical cable.

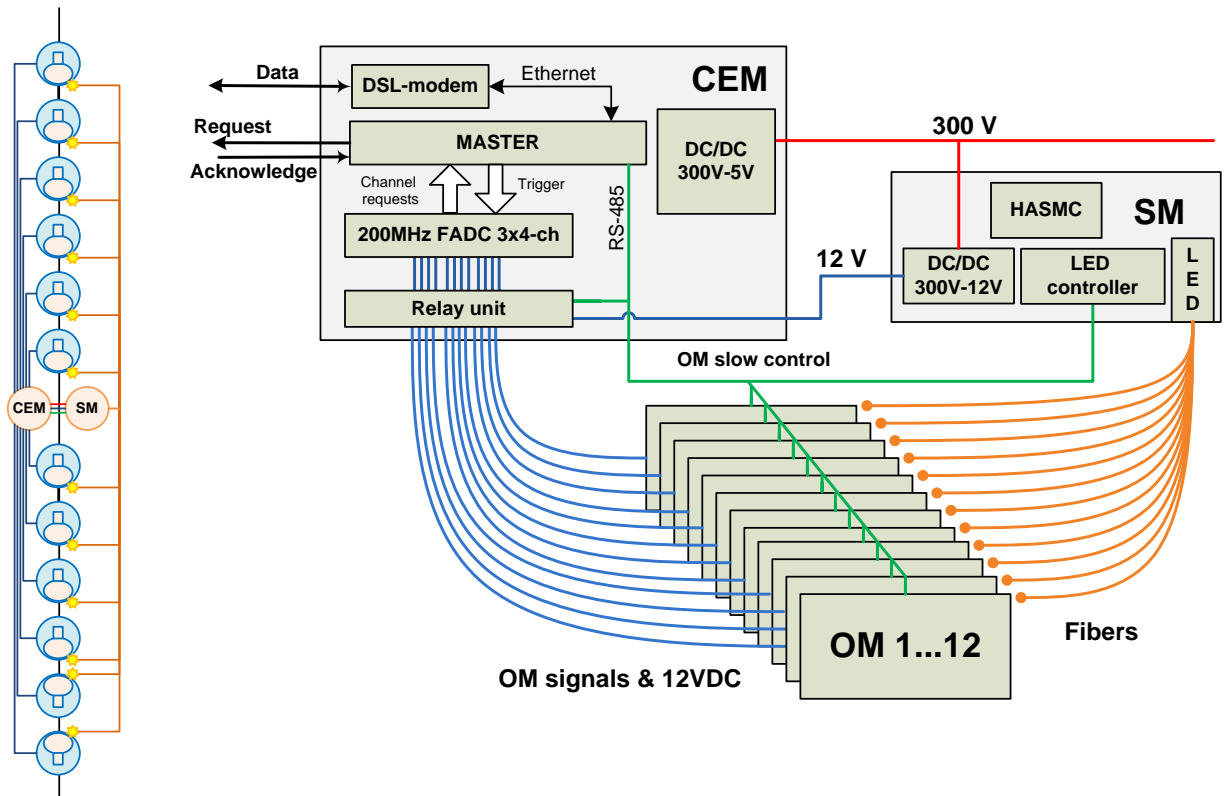


Fig. 4.2.1: Functional scheme of BAIKAL-GVD section.

Data from OMs of the section are readout through the Ethernet channel of the *Master* board, which is elongated to 1200 m via DSL modems (transfer rate up to 8 Mbit/s). A local underwater RS-485 data bus, based on the ASCII protocol, is used for slow control (setting the modes of OM operation, calibration, and monitoring the equipment). The Ethernet to RS485 converter for slow control channel is implemented on the *Master* board. The power supply voltage is fed to optical modules from 300 V - 12 V DC/DC converters, which are mounted in the section SM. A relay control of OM switching makes it possible to switch off optical modules from the power supply unit in the case of short circuit. Along with DC/DC converters, the SM includes elements of the calibration system and the acoustic positioning system.

A section is calibrated by two pulsed LED light sources, the signals of which are branched through optical cables to all optical modules of the section. The monitoring system of the section provides information on the power supply voltage across the section and each optical module, on the temperature inside OM, on the high voltage across the photomultipliers, and on the count rate of PMT noise pulses.

The design of the central and service modules is similar to a great extent to the OM design. The electronics of the modules is located in pressure-resistant VITROVEX glass spheres. An aluminum ring is glued into the lower hemisphere, and a crate with electronics is mounted on this ring. Signals and data are transferred using pressure-resistant coaxial CP-50-862/863 connectors. The power supply (300 VDC), data transfer (Ethernet), and synchronization (*request* and *acknowledge* signals) are performed through a load-carrying cable, which contains three conducting supply wires, a twisted-pair cable for data transfer (data), and two coaxial cables for synchronization. The main parameters of the OM section are listed in table 4.2.1.

Table 4.2.1: Main parameters of BAIKAL-GVD section.

Number of measuring channels	up to 12
PMT type	R7081HQE
ADC sampling rate	200 MHz
Number of effective ADC bits	11
Dynamic range of spectrometric channels	$1-10^4$ p.e.
Linear range of spectrometric channels	$1-10^2$ p.e.
Event time window	to 5 μ s
Frequency of channel noise pulses at a level of 0.3 p.e.	~ 20 kHz
Data transfer rate from a section at distances up to 1200 m	8 Mbit/s
Accuracy of time measurement in a channel	2 ns
Error of channel amplitude calibration	$< 10\%$
Error in determining the section coordinates	~ 0.2 m
Power supply voltage	300 VDC
Power consumption	< 100 W

4.3 String

String is the basic structural unit of the BAIKAL-GVD detector. It is an assembly composed of several sections, positioned on the same backbone cable. The string includes two or four sections and communication module (COM). The functional scheme of a string is shown in Fig. 4.3.1.

The string communication module provides connection of data transfer, synchronization, and power supply systems of sections to the load-carrying cable, which connects the string to the cluster DAQ-center. The cable of the KG(2RK50+(2x0.5)E+3x0.5)-50 0a type ('PSKOVGEOKABEL') consists of two coaxial RK50 cables to translate *request* and *acknowledge* signals, three power supply wires with a cross section of 0.5 mm^2 and a screened twisted pair for data transfer. The data from sections are transferred through DSL modem lines to the COM and translated (through the Ethernet switch and additional DSL modem) to the cluster DAQ-center. The *request* signals from sections are combined by a logical *OR* element in the trigger commutator unit to form the string *request* signal. The *acknowledge* signal from COM is branched to arrive at string sections. The string configuration, composed of two sections, does not need additional switching of power supply lines: each section is connected to its own power supply wire in the load-carrying cable. The power supply voltage 300 VDC is controlled in the cluster DAQ-center through a relay commutator. The relay commutator

is also planned to be used for a larger number of sections in the string communication module.

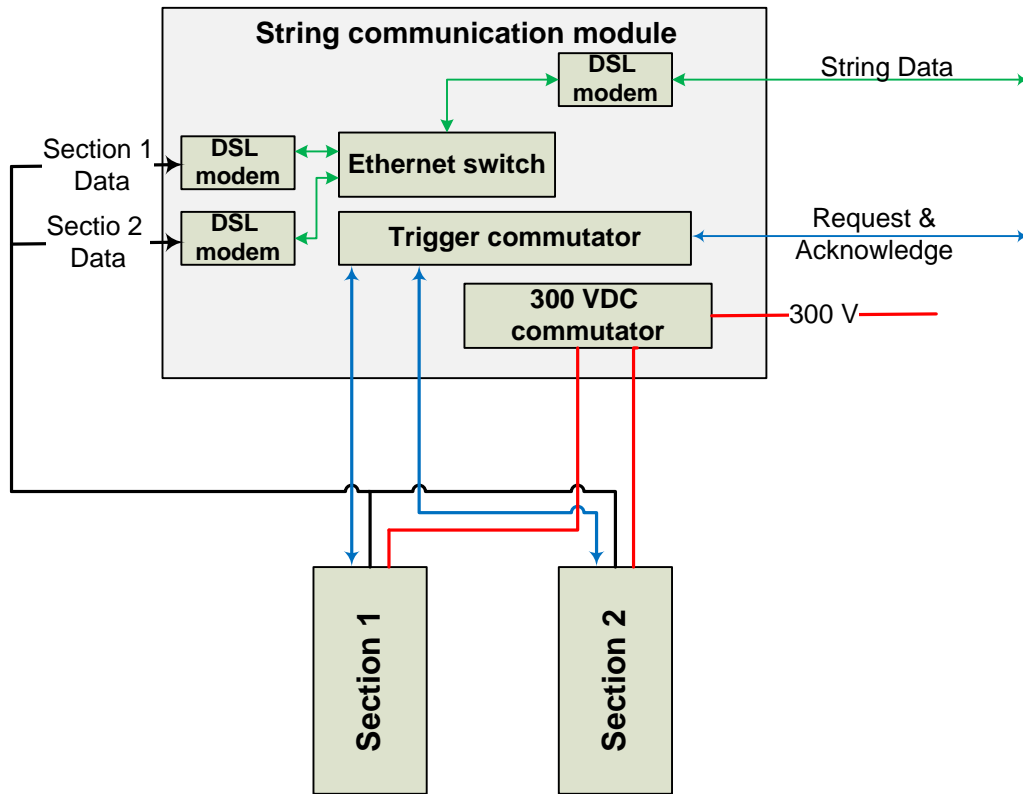


Fig. 4.3.1: Functional scheme of the string communication module of BAIKAL-GVD.

4.3.1 Calibration of measuring channels

The BAIKAL-GVD is designed for long-term operation. The characteristics of its detection channels may degrade in the course of time because of the variations in the parameters of photomultipliers and measurement circuits and change in the equipment operation conditions (in particular, PMT supply voltage). The measured values are transformed into physical parameters (photon intensity and photon arrival time) using results of the section calibration. Two main stages of section calibration procedure are the temporal and amplitude calibrations. Temporal calibration serves to determine the intrinsic delay times of channels (time shifts), which are related to the rather large lengths of communication cables and photomultiplier delays. Amplitude calibration is aimed at transforming the PMT signal response into the number of photoelectrons. One can pass from photoelectrons to the Cherenkov photon flux using the known value of the PMT photocathode quantum efficiency, which is in turn controlled with the aid of an underwater laser light source and atmospheric muons. Temporal calibration is performed using a LED light source located in the service module. A light pulse from the LED source is branched and applied to each optical module through fiber cables with a calibrated optical length. With a known delay times in the optical cables, this approach makes it possible to find the relative time shifts for each channel. This technique was tested on the NT200 and NT200+ detectors and yielded a time calibration error of about 2 ns. A drawback of this approach is the necessity of using 12 fiber cables for each section, which increases significantly the deployment time on the lake ice cover. The application

of FADC in the measurement channels of sections makes it possible to use an alternative technique of time calibration, which is based on direct measurement of the signal delay time in the optical module (the measurement technique is described in Subsection 4.1). To find the time shifts of channels, it is sufficient to add the time delay of cables, measured in a laboratory, to the signal delay in OM.

The amplitude calibration of spectrometric channels is based on the widely used technique of measuring single-electron spectra (SES) of photomultipliers. The SES of PMT is measured using a LED flasher installed in the optical modules (Subsection 4.1.4). Two pulses with a delay time of about 500 ns are produced by the LED flashers during the amplitude calibration. The first LED provides a pulse of low intensity (single electron mode of phototube operation). The intensity of the second LED pulse is substantially higher than the PMT noise level. This pulse is used as a trigger for the phototube dark noise suppression. An example of an SES for OM is presented in Fig. 4.3.2. The single electron distribution has an average value of about 80 FADC channels above the pedestal (see parameter p3 in Fig. 4.3.2). This value is used as an amplitude calibration coefficient for the given FADC channel.

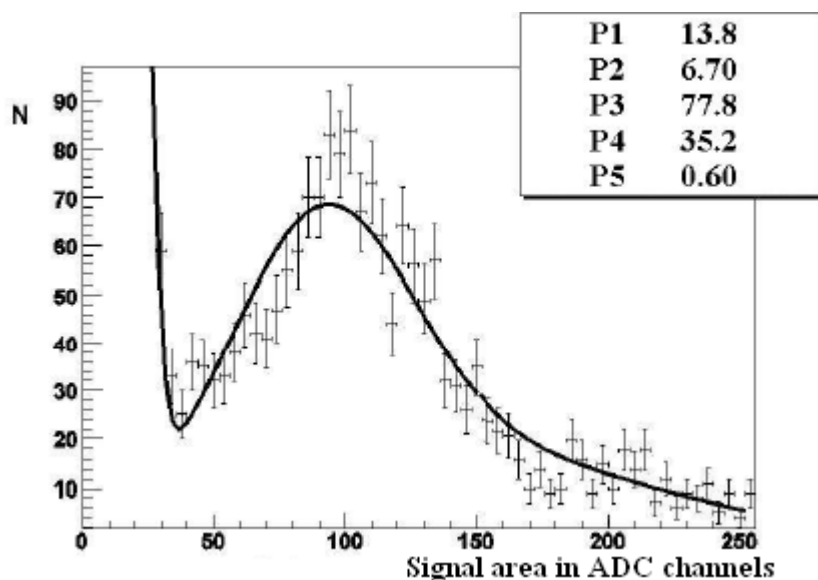


Fig. 4.3.2: Single-electron PMT spectrum.

Thus obtained calibration coefficient can only be used in the linear range of measuring channel operation, which is limited by signals of ~ 100 p.e. Specifically this range is most interesting in the reconstruction of physical events in BAIKAL-GVD. To apply the amplitude information in the nonlinear range, one must measure a calibration curve of channels (dependence of the measured pulse charge on the number of detected photoelectrons). Measurement of the calibration curve is performed using light pulses produced by two LEDs by means successive doubling the LED luminosity and tabulating obtained channel responses. An example of a channel calibration curve is shown in Fig. 4.3.3. Measurement errors are accumulated with a calibration signal increase, and a systematic shift of the calibration curve may arise. The systematic shift of the calibration curve in the range up to $\sim 10^3$ p.e. was measured by independent way and turned out to be 10%, which does not exceed the statistical error at the linear-range boundary (100 p.e.).

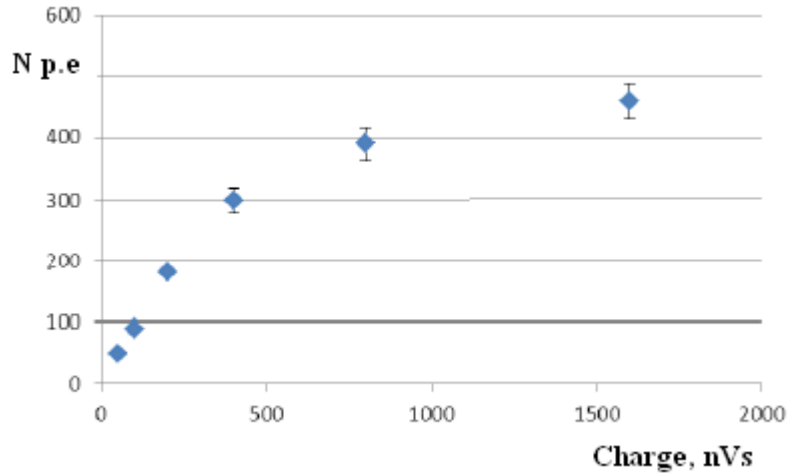


Fig. 4.3.3: Example of the calibration curve of a spectrometric channel. The measurements were performed with a load of 50Ω .

4.4 Cluster

The basic configuration of BAIKAL-GVD cluster comprises eight strings, a data acquisition center (DAQ-center), and electro-optical cable, which connects the cluster to the shore station (see Fig. 4.4.1). The DAQ-center of a cluster consists of 3 underwater modules, located at a shallow depth of about 30 m: a cluster communication center, a PC-sphere, and an optical cable clutch.

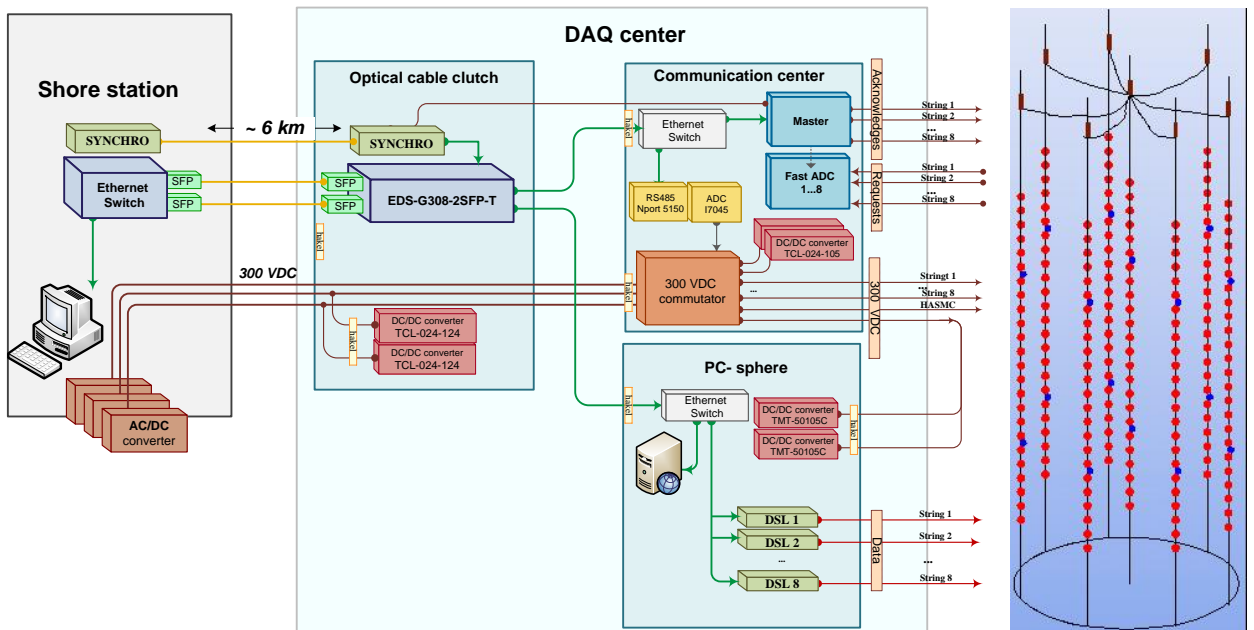


Fig. 4.4.1: Functional scheme of the data acquisition center of a cluster (on the left) and a cluster composed of eight strings (on the right).

Strings are connected to the DAQ-center of cluster through ~ 1.2 km long cables, which serve to transfer data, supply power, and synchronize the operation of sections. Data from 8 strings are transferred through two-wire communication lines based on DSL modems, located in the PC-sphere (data transfer rate up to 8 Mbit/s). This module contains also an underwater microcomputer to perform on-line analysis of the information received. The strings data are transferred from the PC-sphere to the optical cable clutch through an underwater 100-Mbit Ethernet line for their subsequent translation to the shore through the Gigabit Ethernet switch EDS-G308-2SFP-T.

The cluster DAQ-center is connected to the shore by an electro-optical cable about 6 km long. This cable serves to feed the cluster and transfer digital data through a gigabit optical fiber communication line (OFCL). An OFCL consists of 3 pairs of single-mode fibers (AHWave FLEX ZWP). Two pairs are used to transfer data (main and reserve lines), and one pair is aimed at synchronizing the operation of BAIKAL-GVD clusters. Shore power supply units (AC/DC converters) with an output voltage up to 450 VDC and power up to 1 kW are used to feed a cluster. The output power supply voltage is controlled so as to provide a voltage of 300 V at the end of the 6-km underwater feed line. The underwater part of the equipment, which is designed to control the cluster power supply and to synchronize the operation of the sections, is located in the cluster communication center. Independent switching on and off the 300V power supply of each section is performed by a relay commutator, which is controlled via a 16-channel digital output module (I-7045) and RS485 serial device server (NPort 5150A-T). The relay commutator and its control devices are fed by TCL-024-124 sources, which are located in the optical cable clutch.

The operation of the measuring systems of cluster sections is synchronized by the DAQ-center *Master* and 8-channel FADC units, which are identical to the units of the section CEMs. *Request* signals from all strings arrive at the cluster DAQ-center, where their arrival times are measured. The *Master* unit analyzes the string requests and generates a *acknowledge* signal, which is branched to all sections of all strings as a global trigger. The arrival times of photons detected by section channels are measured with respect to this signal. The differences in the transit times of the *request* and *acknowledge* signals of different sections are measured with FADC units of the CEMs with an error of < 5 ns.

4.5 Trigger Formation and Data Transfer Systems

The BAIKAL-GVD data transfer and trigger systems are closely interrelated. The neutrino telescope records fairly rare events. However, to detect signal events from muons or showers by the selected trigger system at the instrumental level with a high detection efficiency, one has to reduce maximally the channel detection thresholds. As a result, background (noise) events make the main contribution to the total data flux. The background is filtered in the stage of on-line analysis of the data in the shore station. The data transfer system is aimed at transmitting the total data flow (which can be as high as several tens of Mbit/s) from the underwater part of the system to the shore station without loss.

4.5.1 Data transfer system

The underwater information network of the BAIKAL-GVD is based on usage of the Ethernet technology. The network design is schematically shown in Fig. 4.5.1. Four types of underwater information network segments can be selected: the shore segments linking cluster DAQ-centers to Shore station; the cluster segments linking cluster DAQ-centers and string communication modules (COM); the string segments linking COMs and section central modules (CEM); and the section segments linking CEMs with optical modules (OM).

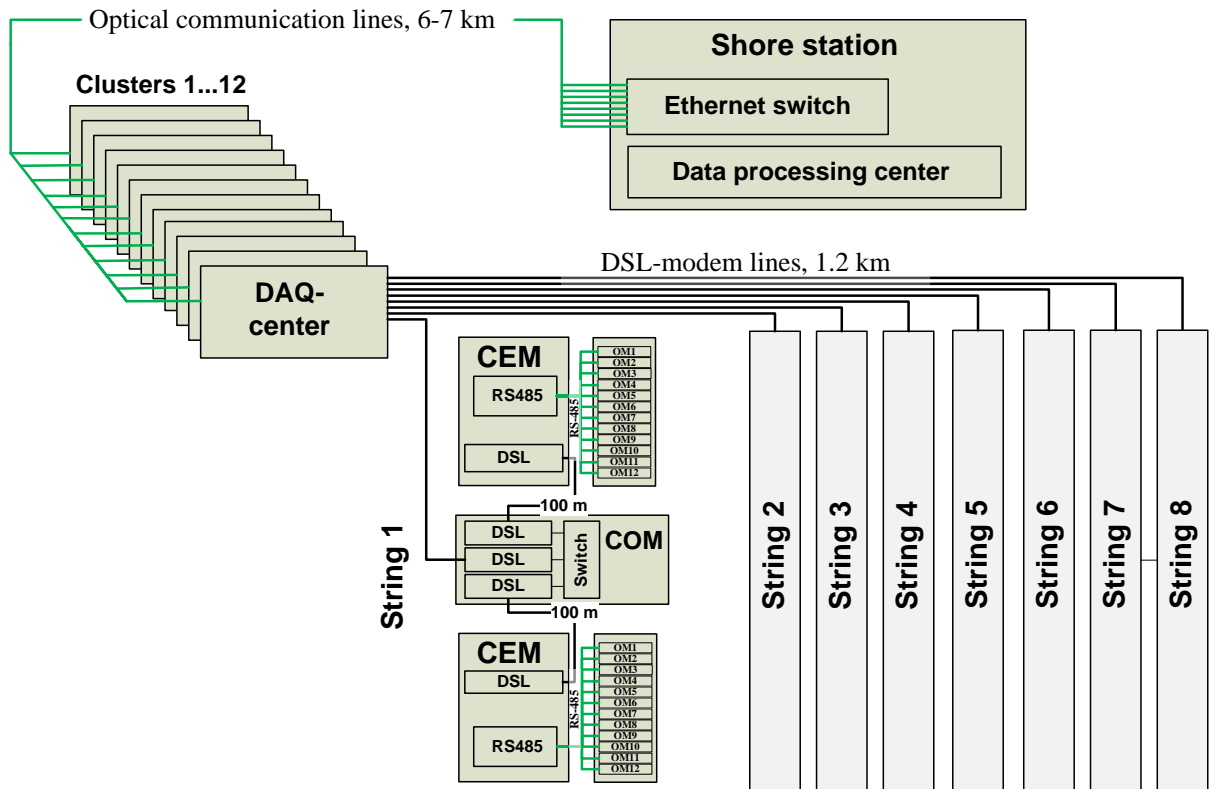


Fig. 4.5.1: Architecture of the BAIKAL-GVD underwater information network.

Table 4.5.1: Segments of BAIKAL-GVD underwater information network.

Segment	Length	Cable type	Technology	Transfer rate
Shore	6 - 7 km	Optical fiber	1000 Base FX	1 Gbit/s
Cluster	1.2 km	Twisted pair	xDSL, 2 wire	8 Mbit/s
String	100 m	Twisted pair	xDSL, 2 wire	12 Mbit/s
Section	100 m	Twisted pair	RS-485, 2 wire	115200 bit/s

Table 4.5.1 shows the main characteristics of the communication lines for segments of all types. The data transfer rates were obtained from direct measurements with the real cable communications that are expected to be used in the BAIKAL-GVD system. A two-wire RS-485 bus with the ASCII protocol is applied to control the operation of the optical modules of the sections that does not require high data transfer rates. This channel is used to set the OM operation modes (PMT high voltage and

parameters of OM monitoring system) and transfer the monitor information from optical modules: noise count rate, temperature, and power supply voltage.

Testing of the RS-485 communication line under real underwater operation conditions in Lake Baikal showed its reliable operation at distances ~ 100 m (a half-length of one string section) at a rate of 115200 bit/s. With the exchange rate reduced to 9600 bit/s, data can be reliably transferred at distances up to 1 km.

Much higher rates are necessary to transfer the data on the time tracks of FADC channels of sections. This is due to the large amount of data associated with each recorded event. The amount of information on an event is determined by the degree of compressing the waveform stamp data by on-line processing system of the CEM *Master* board. If the data are not processed and complete information from the 5- μ s window of each FADC channel (2 Kbyte per channel) is transferred, the amount of data per event in section (12 OM) is 24 Kbyte. This technological mode is used to test and monitor the measurement equipment and does not require high data transfer rates. In the main operation mode the size of data sample will be reduced significantly by selecting only useful information from a waveform stamp in the intervals where the desired signal exceeds the channel noise level: 40 bytes per pulse and on average about 200 bytes per event recorded by one section (with allowance for the contribution of PMT noise pulses). With this event size, the limiting throughput of the section-string and string-cluster network segments, connected in series, is $\sim 2 \cdot 10^3$ events/s. The subsequent data transfer to the shore station through a fiber communication line does not reduce the throughput of the system as a whole.

4.5.2 Trigger system

The arrival rate of physical events is controlled by the BAIKAL-GVD trigger system. The general approach to the organization of this system is based on the selection of events that are characterized by coincidences of signals from certain groups of OMs (trigger groups) in a specified time interval (time of coincidences). The limitations on the choice for channel groups involved in coincidences are related to only the design of the BAIKAL-GVD cable communications through which trigger signals are transferred. The following trigger groups can be selected: coincidences of signals from OMs of the same section, coincidences of trigger signals of sections within one string, and coincidences between strings of the same cluster. The system for controlling the trigger devices allows one to set the following parameters for each trigger group:

- threshold levels of channel digital comparators (two comparators are provided for each channel);
- set of allowed combinations of channels involved in coincidences;
- coincidence time window.

Optimal tuning of the trigger system depends on the current priorities of physical problems, detector sizes (depending on the deployment stage of the system), and the configuration of recording equipment. Currently, the version of tuning the trigger system that is shown in Fig. 4.5.2 is considered as a basic. The lower-level trigger is generated by trigger groups of individual sections. Each section channel forms *request* signals of two types: low-threshold ($l \sim 0.3$ p.e.) and high-threshold ($h \sim 3$ p.e.) ones. The arrival rate of signals l from each channel in the period of enhanced light activity on Lake Baikal

may reach ~ 40 kHz; the signal count rate, h , is approximately two orders of magnitude lower. A characteristic dependence of the suppression factor for PMT noise pulses on the detection threshold in the case of PMT exposure at large depths of Lake Baikal is shown in Fig. 4.5.3. The *request* signals of channels arrive at the *Master* CEM board to form a *request* signal of section: coincidence of signals l and h from any two neighboring optical modules in a 100 ns window (signal lh). The rate of signals lh is about 3 Hz for a pair of optical modules and 30-50 Hz for a section composed of 12 OMs. The *request* signals from two sections arrive in the string communication module COM to be combined into the total *request* signal of the string. The rate of string *request* signals can be as high as ~ 100 Hz

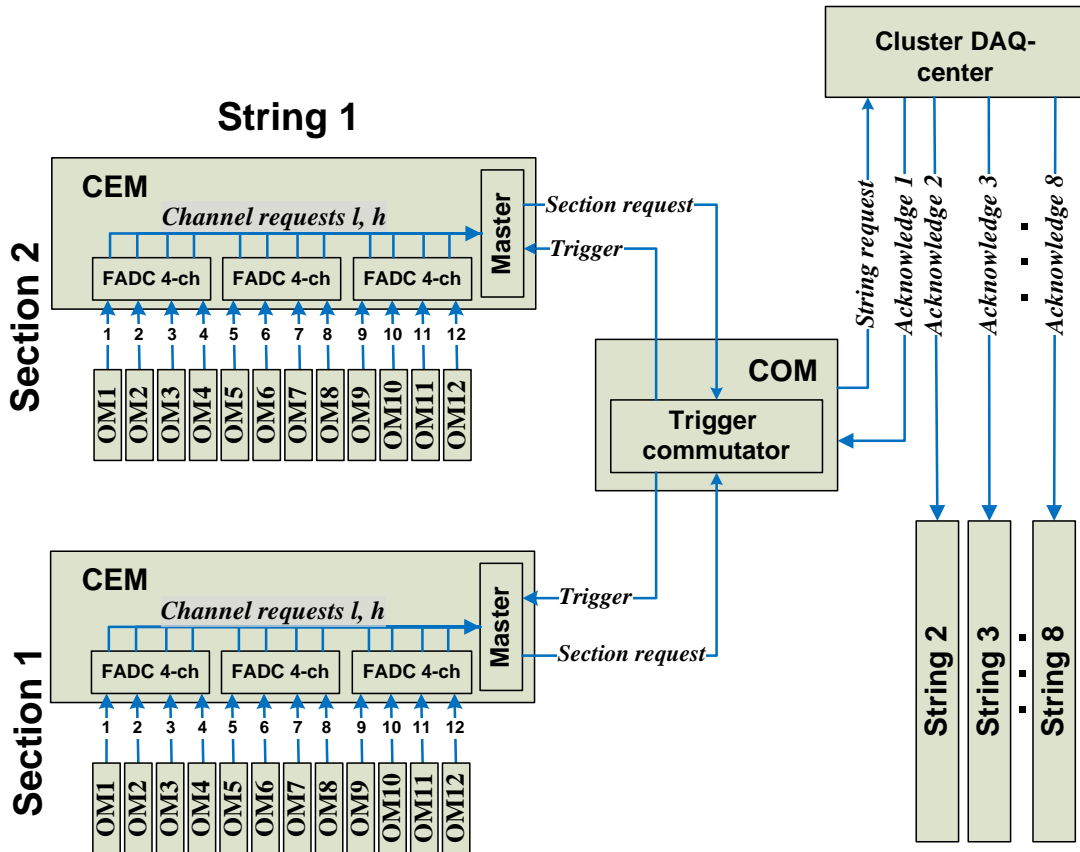


Fig. 4.5.2: Functional scheme of the cluster trigger organization.

The string *request* signals are transferred through coaxial cables ~ 1.2 km long to the cluster DAQ-center, where a cluster trigger is formed as a logical *OR* of all string *request* signals. The cluster trigger forms a *acknowledge* signal, global trigger for all strings. The *acknowledge* signal returns to all cluster strings, is branched in the COM, and translated to all sections as a trigger, providing synchronous data processing by all FADC boards. The delay between the *request* and *acknowledge* signals is mainly determined by the cable length and amounts to $15 \mu\text{s}$.

The trigger rate is determined by the rates of *request* signals from 8 strings and amounts to ~ 1 kHz. The trigger initiates transfer of the data from all triggered ADC channels to the cluster DAQ-center (the throughput of string information channels is $\sim 2 \cdot 10^3$ events/s). Then the data are translated through the optical communication line to the shore station, where noises are filtered and useful events are selected on-line by corresponding programs.

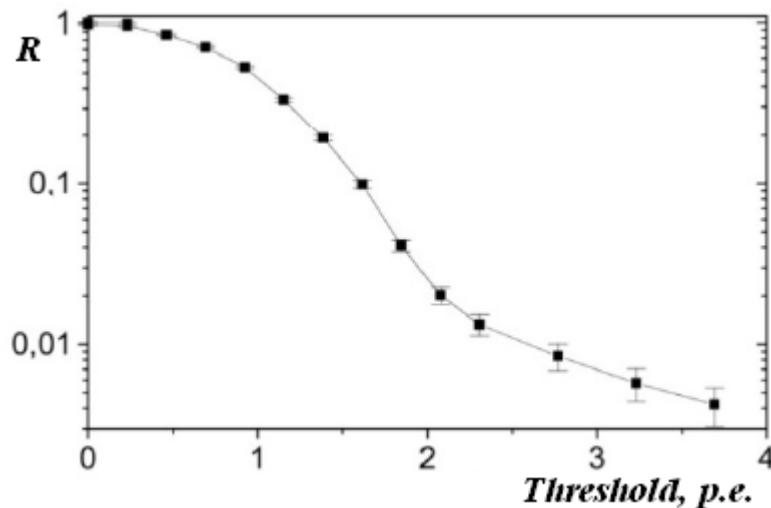


Fig. 4.5.3: Example of the dependence of the suppression factor of photomultiplier noise, R , on the detection threshold.

4.6 Prototype Arrays

4.6.1 Prototypes of GVD string

The first prototype of GVD electronics was deployed in Lake Baikal in April 2008. It was a reduced-size section with six OMs. This unit provided the possibility to study basic elements of the future detector: new optical modules and FADC based measuring system. During the next two years different versions of prototype string were tested in Lake Baikal as a part of NT200+ detector.

The prototype string 2009 consisted of 12 optical modules with six photomultipliers R8055 and six XP1807, which were combined in two sections (Fig. 4.6.1). OMs were spaced by 10 m on the string and the total string length was 110 m. The photocathodes of all PMTs, except for the two lower OMs, were faced upward. The central part of the string contains two CEMs, one service module (SM), and a computer module (PC-sphere), which provides the functions of the BAIKAL-GVD cluster DAQ-center. The control and data transfer systems of the string are similar to the basic design developed for a BAIKAL-GVD section. PC-module formed the global trigger signal for two sections and transferred data to the shore station through an Ethernet channel using a DSL modem. Since the PC-module was located close to the CEMs, it was connected with CEM1 and CEM2 without DSL modems, which are provided in the basic configuration of the section equipment. The equipment of acoustic positioning system was located in separate spheres in the upper and lower parts of the strings.

In 2009 Photonis ceased production of PMTs with a 12'' diameter photocathode. Meanwhile Hamamatsu announced a new PMT R7081HQE, having a 10'' diameter photocathode with high quantum efficiency (more than 30%). In April 2010, a prototype of the GVD string with eight PMTs R7081HQE and four PMTs R8055 was deployed and had been tested until August 2010 in Lake Baikal.

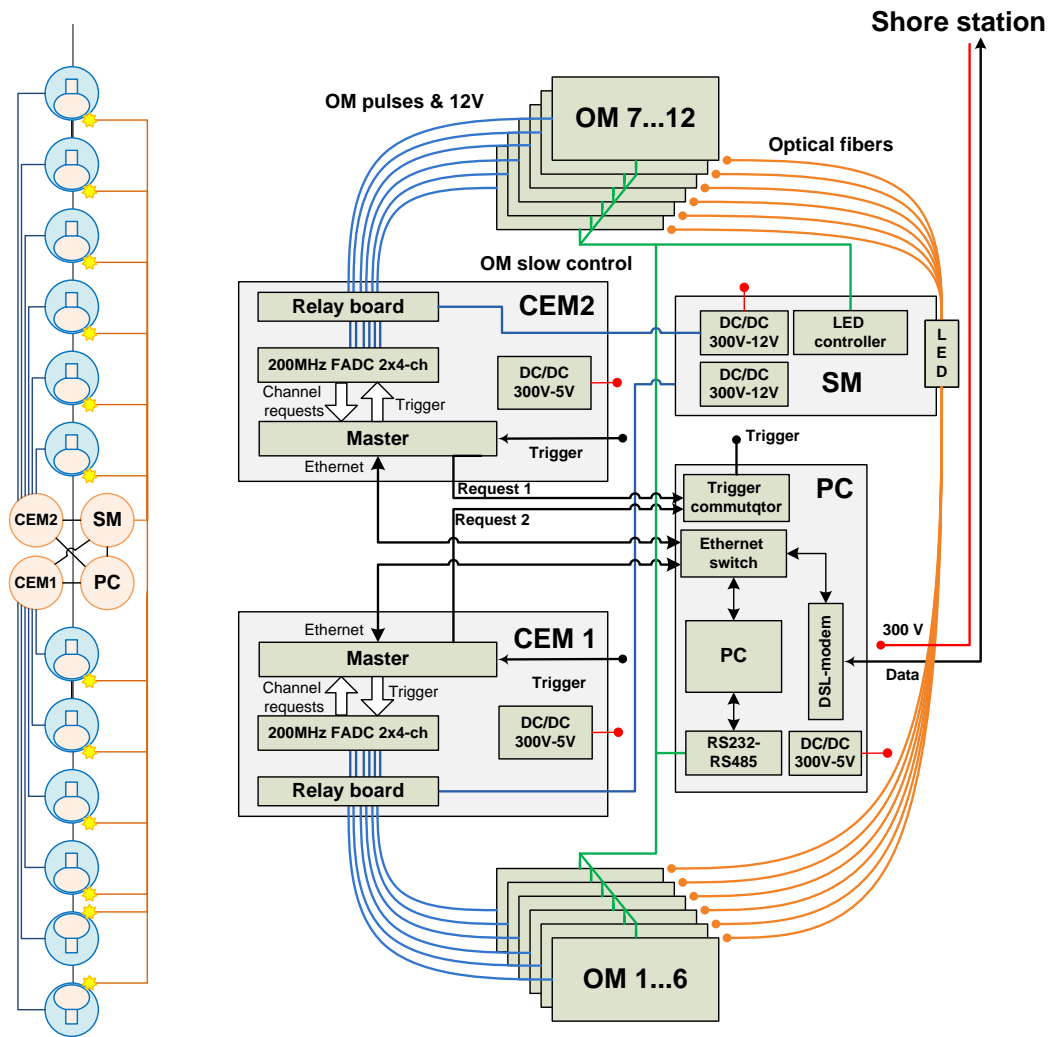


Fig. 4.6.1: Block diagram of the experimental string composed of two sections, six OMs in each.

The tests of the experimental string were aimed at a complex check of the operation of all electronic units, underwater cable communications, and load-carrying structures under long-term exposure of the equipment. On the whole, during the period from 2008 to 2010, the experimental string in different configurations worked for about 12 months. During this time we did not fix any significant errors in the operation or seal failure for the basic string units: optical modules, ADC and control units, and deep underwater cables. The breaks in the string operation were caused by failures of DC/DC converters of the service module. Based on the results of this experiment, systems of lightning protection and string power supply redundancy were developed and implemented.

An analysis of the background detection conditions for the experimental string in Lake Baikal did not reveal any new effects in comparison with those observed previously in the experiments with the NT200 detector. Figure 4.6.2 shows the time dependence of the noise pulse count rate (threshold 0.5 p.e.) for seven OMs. The pronounced correlation in the channel count rates indicates that the luminescence of Baikal water contributes significantly to the PMT noise. Independent investigations showed that this water emission has a chemiluminescence nature. Along with relatively stable luminescence periods, there are intensity bursts, which increase the noise pulse rate by more than twice.

These bursts are due to the transport of luminous masses by deep-water flows in Lake Baikal.

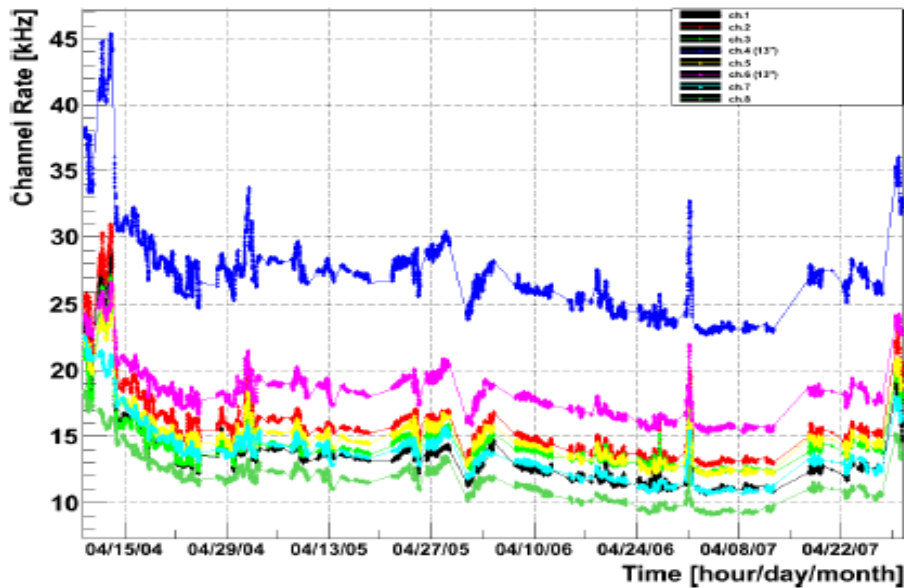


Fig. 4.6.2: Count rates of seven OMs of the experimental string for a four-month exposure in 2009.

The key parameter of the BAIKAL-GVD telescope is its angular resolution, which should be much better than 1° . The angular resolution depends primarily on the accuracy in measuring the Cherenkov radiation arrival time for each measuring channel. This error is determined by two parameters of the recording system: the time resolution of the channels and error of their time calibration. In situ tests of the prototype strings allow to estimate the accuracy of photon arrival time measurements. The measurements were performed with the LED-flasher, laser calibration source and cosmic ray muons.

The time resolution of the channels was measured *in situ* using a LED-flasher. A LED-flasher was located in the central part of the string (in the service module). It generated a series of double pulses with a strictly fixed time delay between them. The delay about $0.5 \mu\text{s}$ was chosen so as to make both pulses fall in the same event time window ($5 \mu\text{s}$). The light pulses were transferred to all OMs of the string through optical fibers. The positions of pulses on the time tracks of channels were determined by excess over a fixed threshold, which was chosen at a level of 0.5 p.e. Figure 4.6.3 shows the delay between LED-flasher pulses calculated using channel waveform data. The value of the time delay averaged over all channels (498.3 ns) differs from the expected value (497.5 ns) by less than 1 ns. The delay rms deviation, averaged over all channels, is 1.6 ns. This value characterizes a time resolution of the string channel. Note that the time resolution can be somewhat improved by fitting the shapes of pulses on a track to determine their position. The significant spread in rms deviations is explained by the difference in the light pulse amplitudes (from 1 to 100 p.e.), which is due to the different focusing conditions for the light from LED-flasher at the inputs of optical fibers.

The accuracy of time calibration is the second factor that affects the detector time characteristics. This calibration implies determination of relative time shifts in channels, t_{shift} , which are due to the difference in the lengths of communication cables and PMT

transit times. The values of the calibration parameters t_{shift} , obtained by two methods (measurement of the detection times of LED-flasher signal, common for all channels, and measurement of the PMT intrinsic delays), are consistent within 3 ns, which exceeds somewhat the expected value of 2 ns. The analysis of the reasons for this discrepancy between the calibration results will be continued.

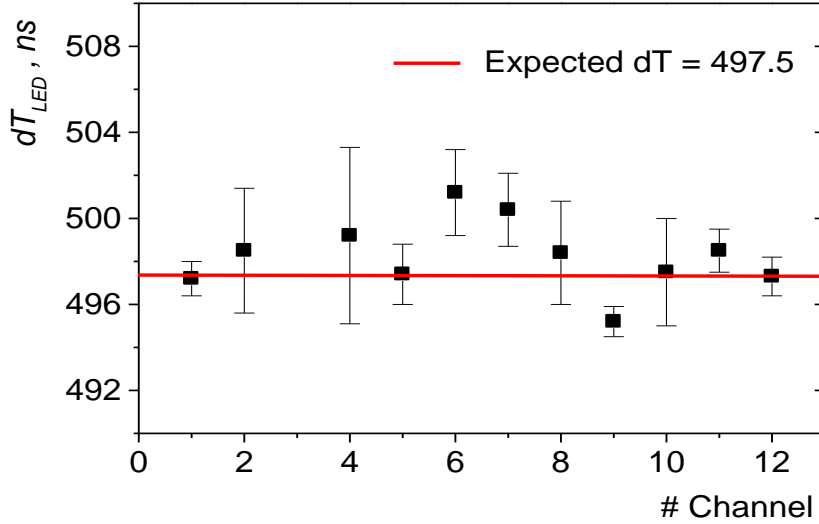


Fig. 4.6.3: Time difference between LED-flasher pulses measured for 12 channels of the experimental string.

More detailed studies of the time accuracy were performed with a laser based calibration source. It is an isotropic light source with intensity up to $5 \cdot 10^{13}$ photons per pulse at a wavelength of 475 nm and light pulse width less than 1 ns. The laser source was located at a distance of about 100 m from the experimental string, at a depth of ~ 1.2 km. The acoustic positioning system provides an error in determining the mutual position of the laser source and the optical modules of the string at a level of 0.5 m. Hence, one can compare the expected radiation arrival time at the string channels with the experimental values. The measured parameter was a difference in the response times of string channels, ΔT . The results of comparing the measured values, ΔT_{meas} , and the values expected from geometric considerations, ΔT_{geom} , are listed in Table 4.6.1 in dependence on the distance between the channels. The ΔT_{meas} values were obtained by averaging over all combinations of the channels spaced by the same distance R. These results suggest that the error in measuring the detection times of string channels does not exceed 2 ns, which provides the necessary angular resolution of the BAIKAL-GVD detector.

Table 4.6.1: Calibration of string channels by a laser light source.

Distance between channels, m	10	20	30	40	50
$\Delta T_{meas} - \Delta T_{geom}$, ns	0.3	-1.2	-2.2	0.5	1.3

The atmospheric muon flux makes it possible to investigate the performance of the time measuring channels of the experimental string under the conditions that are very close to the real experiment. The muon events were analyzed for a pair of OMs with upward faced PMTs, which imitate most adequately the detection conditions for the neutrino events from the lower hemisphere. The experimental distribution of time

difference ΔT was compared with the results of simulation (Fig. 4.6.4). The experimental distribution is in good agreement with the expected one. The relative displacement of the distributions on the time scale is 2 – 3 ns. This value characterizes the time error of the experimental string as a whole, including all sources of time measurement errors.

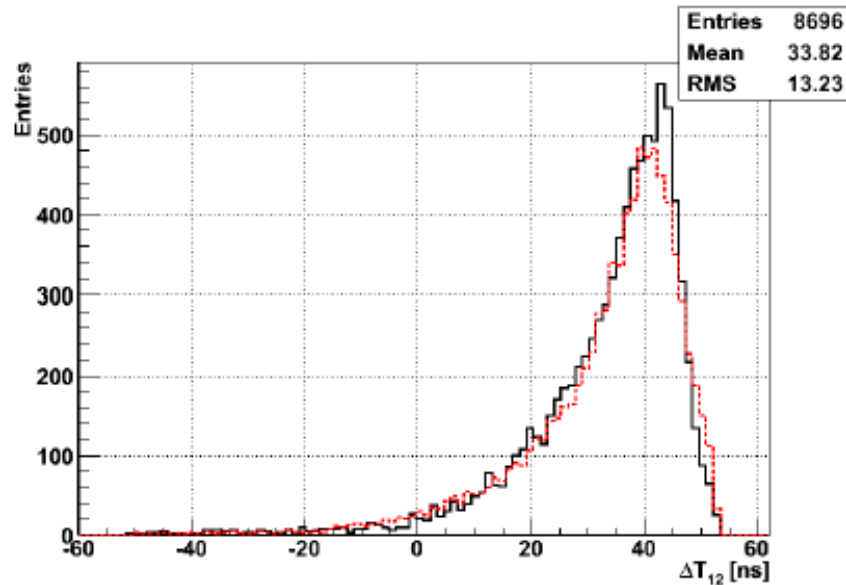


Fig. 4.6.4: Distribution of time difference ΔT between muon pulses for two up-ward faced PMTs: experiment (solid histogram) and calculation (dotted histogram).

The atmospheric muon flux is a natural calibration source which allows to test the performance of the array measuring systems, as well as to estimate the efficiency of background suppression and event reconstruction procedures. Prototype string data allow to reconstruct the zenith angle distribution of downward going atmospheric muons. A selected sample of 2010 prototype string data was used for the atmospheric muons analysis. A sample of MC-events from atmospheric muons has been generated, taking into account the features of prototype string measuring system and actual counting rates of optical modules. At the first step of analysis a causality criterion, as well as a special muon selection conditions were applied to events for elimination of background signals caused by PMTs noise and water luminescence background, muon bundles and electromagnetic showers induced by muons. At the next step the cleaned time information of OMs was used for track reconstruction with a trigger condition >3 hit OMs. Finally, soft cuts on χ^2 value and on the error of reconstructed zenith angle were applied for muon event selection. Fig.4.6.5 illustrates the precision of the zenith angle reconstruction procedure. Shown here is a distribution of mismatch angles between generated and reconstructed zenith angles of muons. An expected average number of muons in finally selected events is about 1.8. This explains the rather wide shape of mismatch angle distribution in Fig.4.6.5. Zenith angular distributions of experimental and MC-simulated event rates are shown in Fig.4.6.6. The good consistency between the data and theoretical expectation confirms the expected performance of the time measuring systems and the efficiency of used calibration methods, as well as the efficiency of event selection and noise suppression procedures.

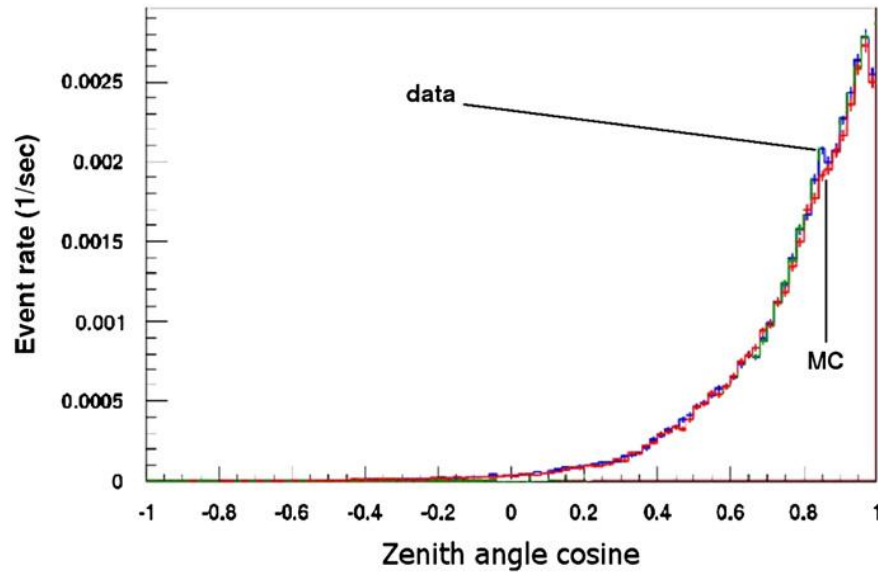


Fig. 4.6.6: Experimental and theoretically expected event rates after final cuts.

4.6.2 Prototype of GVD cluster

The operation of GVD prototype strings in 2009 and 2010 allows a first assessment of the DAQ performance. On the basis of the experience of prototype string operation, in April 2011 a prototype GVD cluster with three strings was installed in Lake Baikal and put in operation. Each string consists of one section with eight optical modules. Distances between the OMs are 10 m along the string; distances between the strings are 40 m. The OMs house photomultipliers of different types: 16 PMTs R7081HQE, three PMTs XP1807, and five PMTs R8055. Also, transmitters and receivers of two alternative acoustic positioning systems are arranged on each string. A sketch of prototype cluster and layout of cluster, NT200+ and communication lines are shown in Fig.4.6.7 and Fig.4.6.8.

Analog signals of PMTs are transferred to the central modules (CEMs) of sections. For the connection between the CEMs and the cluster center an armored 1.2 km carrier cables were deployed (custom designed for this setup). Each cable includes two coaxial lines for request and global trigger signals, a screened twisted pair for the DSL-modem data channel, and three power lines.

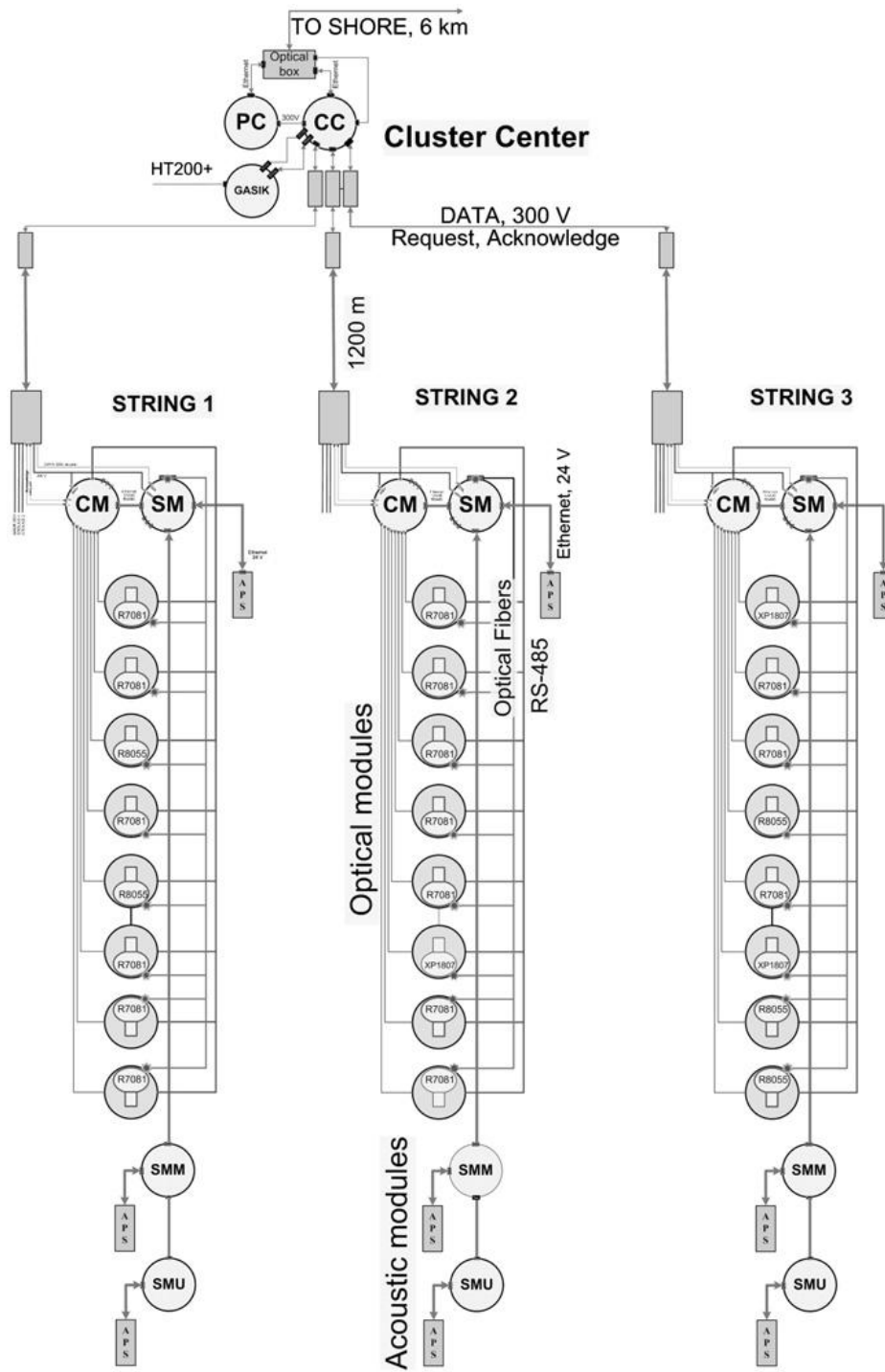


Fig. 4.6.7: Artistic view of the 2011 year prototype cluster.

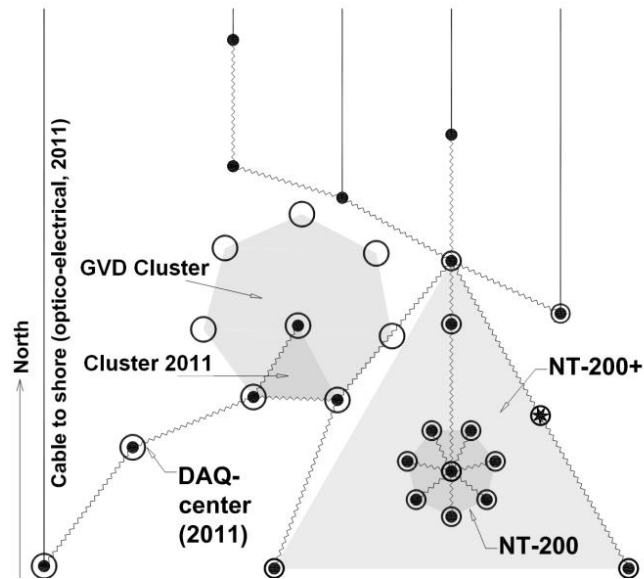


Fig. 4.6.8: Sketch of prototype cluster, neutrino telescope NT200+, and communication lines locations.

The cluster DAQ-center is placed near the surface (~30 m depth as for GVD layout). It provides the string triggering, power supply, and communication to shore. A block diagram of the cluster center electronics is presented in Fig.4.6.9. The design of central and section trigger systems are the same. The section request lines are connected to three inputs of the central ADC board. The request pulse waveforms are accumulated in the ADC buffers. The *Master* board distributes the global trigger for all strings. Data from the strings are transferred through DSL-modem channels to the cluster center. The DSL-modem bandwidth was set to the level 4Mb/s (about half of maximum data rate supported for 1.2 km cable line). This value restricts the maximum event rate per string section to about 25 Hz. Each event has a fixed length of 16 kB and contains waveform data for all ADC channels for 5 μ s time window centered around the trigger time. The prototype cluster DAQ-center is connected to shore by optical Ethernet lines. An electro-optical cable of 6 km length with three pairs of optical fibers and three power lines was deployed in 2011.

The prototype cluster was successfully operated since April 2011 till February 2012. The cluster DAQ system was tested with the Baikal underwater calibration laser, with LED-flashers, and atmospheric muons. Two trigger modes were used for muon detection: four-fold coincidences of optical modules on a string (trigger 4/1, event rate 4 Hz), and inter-string two-fold coincidences of two strings (trigger 2/2, event rate 0.5 Hz). All tests of the prototype cluster show good performance of the basic cluster elements.

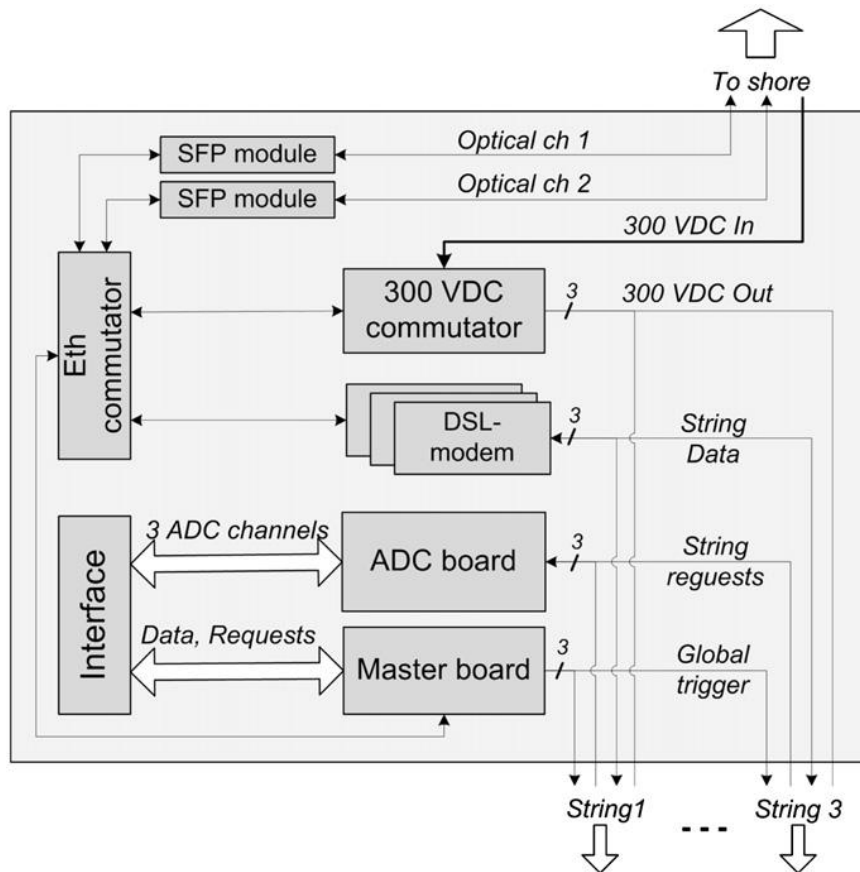


Fig. 4.6.9: Block diagram of the cluster DAQ center unit of the 2011 prototype GVD cluster.

4.7 Shore Data Acquisition and Control Center

The shore DAQ-system for collecting and processing events should be organized as follows. Electro-optical bottom cable lines (one line per cluster) are used for power supply and data exchange of clusters. Data channels are connected to the Host PC Station through a 16-port Ethernet switch to the input of the Host Station, where the data flow is processed. The Host Station (enterprise-level server, designed, in particular, for scientific computations) is a multiprocessor platform (processors based on four or more cores) with 128-Gb RAM, in the address space of which a unified dataset is formed from the input data flow. The Host Station must have a sufficiently high reliability (up to *hot* replacement of components), be easy in maintenance, and flexible in distributing resources. Preliminary estimates show that this system is minimally sufficient for stable processing of the total data flow, concerning all main purposes of the system. However, in the case of unforeseen increase in the necessary computational resources of the server, the solution chosen has an advantage: its resource can easily be increased by scaling. The dataset formed is filtered, and the events that did not pass through the trigger chosen for a specific physical problem are rejected, while the events passed through the trigger are directed to the output data flow. The output data are saved either on the RAID-5 array or on external carriers. The predicted data flow from the system suggests the annual amount of the output data to be no larger than few terabytes. Thus, this configuration not only makes it possible to store data but also allows one to use, process, and transfer them on-line through the Internet. The accuracy in timing the experimental data to the world time

should be better than 100 μ s. Such accuracy can be achieved by installing and tuning local GPS receivers and tuning the *ntp* (*network time protocol*) service.

The functions of the basic service program of the software system (Basic Program, BP), which is run at the Host PC, are as follows:

- Choice of the static configuration of the telescope (number of clusters, strings, addresses of data transfer controllers, etc.). Change in the dynamic parameters of the state of strings and optical modules of the telescope (setting PMT high voltages, channel thresholds, modes of the LED-flasher operation, and setting parameters in the data transfer controllers of the strings).
- Time and amplitude calibration of the detector.
- Saving the data obtained in the real-time format using a large set of information messages. The obtained data of different types are saved (after preprocessing) in data files and are indicated by corresponding marks.
- Automatic logging sessions performed and tests of measurement systems.
- Provision of an integrated set of low-level utilities that are necessary for handling separate OMs and data transfer controllers.
- Generation of monitor data (amplitude and time distributions, statistical distributions, spectra of the shape of measurement channel pulses), which is necessary for on-line monitoring the information received.

The Host PC software is developing under the Linux OS on the C and C++ languages, using Qt and ROOT graphical libraries (and the tools existing in the ROOT for developing and designing applied user interfaces). One of the key features of the shore software developed is the possibility of full remote control of the detector through specialized network protocols SSH and VNC, which are provided at the OS level. This possibility is necessary for solving current problems, maintaining the standard mode of detector operation during data collection sessions, and on-line monitoring the quality of the information received. The use of the system for remote monitoring and controlling the detector increases significantly the efficiency of the system; however, a threat of unauthorized access to the local computational network of the telescope arises in this case. To protect the computational network from unauthorized access, it is divided into two zones: a users' zone, which contains user computers with access to the Internet, and a safety zone, with the equipment that is necessary for the telescope operation. The safety zone contains the computers of the data collection system of the telescope (Host PC); the systems for monitoring the telescope operation; and the underwater local computer network, which is connected to the shore part of the control system through a fiber cable. The local network is connected to the Internet through a router for controlling access. The router is also equipped with a firewall to exclude all unauthorized entry connections. When entering the local network, one can get access to the shore-center computers only after the corresponding authentication procedures.

5 ACOUSTIC POSITIONING SYSTEM

5.1 Positioning System of NT200/NT200+

Exact positioning of photo-sensors of deep underwater neutrino telescopes is impossible, in contrast to underground and ground-based cosmic ray detectors. Even in conditions of deploying from the ice cover at Lake Baikal, buoy stations cannot be positioned with accuracy better than several tens of centimeters. Moreover, positions of optical modules change during operation due to undercurrents. However, effective reconstruction of the events detected by a neutrino telescope requires sufficiently precise knowledge of spatial coordinates of array elements. Photo-sensor dimension determines the scale of required coordinate measurement accuracy, which is about 200–400 mm for different PMT types. On the other hand, the typical time measurement accuracy, caused by both “electronic” and “physical” jitters, is equal to several nanoseconds that correspond to distances of several tens of centimeters for light propagating in water. Thus, an accuracy of telescope’s optical modules coordinates measurement should be about 20 cm.

Coordinates of optical modules, calibration light sources, and other components of the Baikal neutrino telescope NT200/NT200+ are measured by a sonar triangulation system with the Hydroacoustic Coordinate-Measuring System (GASIK, in Russian transcription) [56], which has been operating well during more than 15 years as a part of the experimental underwater infrastructure of the Baikal neutrino telescope. GASIK is a complex of underwater electronic acoustic sensors fixed on the telescope strings at points, coordinates of which should be determined, and at reference points around telescope, relative to which the measurements are carried out. Functionally, the underwater sensors are divided into receiving-emitting devices (transponder start drivers, TSD, and transponders) and ultrasonic receivers.

GASIK consists of (Fig. 5.1.1):

- shore unit comprising a control computer, a modem, and a power supply unit;
- cable communication line about 7 km long;
- two transponder start drivers (TSDs) at the bottom of the *hydrological* string;
- six battery powered transponders (T) which are disposed at a distance of 600 m around of the hydrological string, and 4 m above ground;
- receivers (R) arranged near the top and the bottom optical modules of the telescope strings and at several positions along the *hydrological* string.

TSDs and receivers fixed on buoy stations are supplied with power by the cables from the shore. TSDs and receivers are equipped with microprocessor modules for measurements, control, and communication with the shore center. Power supply of the transponders is provided with galvanic elements, with energy resource for 2–3 years of autonomous operation. Six transponders are equally spaced along a circle of 600 m in radius centered at the telescope’s *hydrological* string position. Their hydrophones are fixed on a rigid rod at a distance of 4 m from the lake bed. The transponders are reference points associated with geographical coordinates. Six reference points (transponders) have been chosen to ensure the measurement reliability, redundancy and refinement of measurement results during their further statistical analysis. Exact geographical

coordinates of the transponders are determined when the system is deployed.

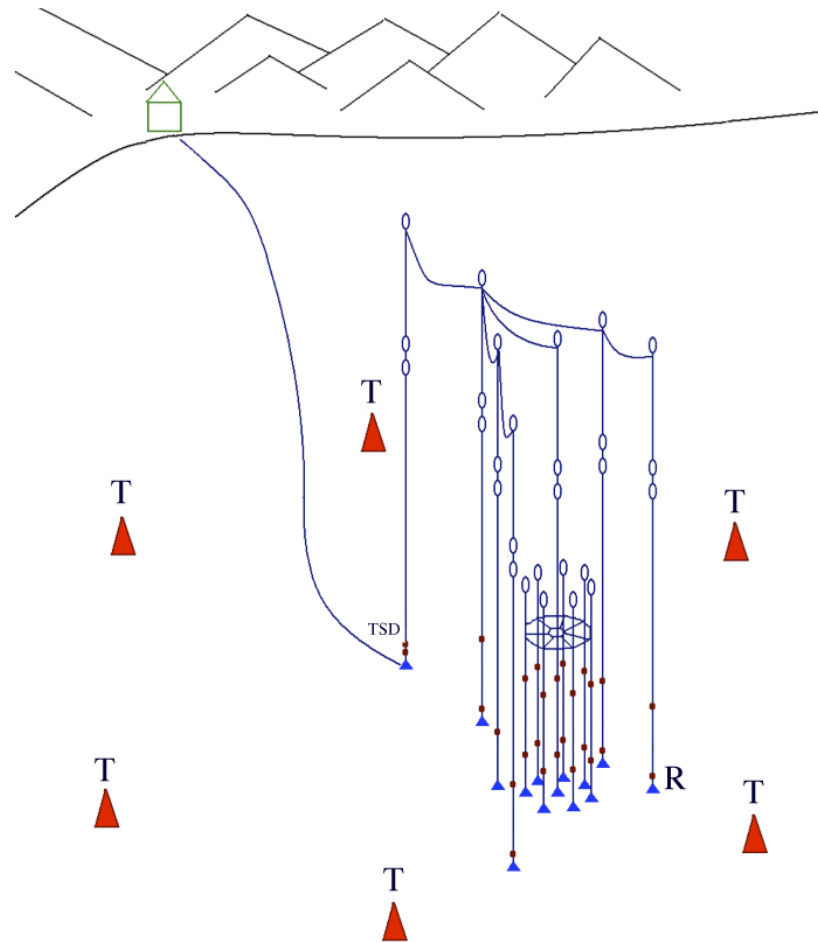


Fig. 5.1.1: A sonar triangulation system of the NT200 neutrino telescope. TSD is the transponders start driver, T marks the transponders, and R – are receivers.

A coordinate measurement is initiated by the shore computer and realized by the following procedure: the TSD produces a coded request to T-transponders; the outgoing sonar pulses mark a path to the T-transponders; having received and decoded the pulses packet with its own address, a T-transponder forms a reply signal; the returning sonar pulses are received by all R-receivers as well as by the TSD. All these modules recorded the times with respect to the original request signal of TSD.

Two TSDs are fixed near the bottom on the *hydrological* string. Receivers are fixed near the upper and lower optical modules on each NT200 strings, on external strings, near the calibration laser light sources, and at several levels on the *hydrological* string. The GASIK uses the pulse-time coding of transponder requests via a hydroacoustic transmission path at a frequency of 28 kHz, and of transponder responses, at a frequency at 32.768 kHz. Spherical piezoelectric elements of 50 mm in diameter are used as electroacoustic transducers. The frequencies of transponder request and response are stabilized by quartz oscillators. There are possibilities to control detection thresholds, as well as initialization times of the TSDs and Receivers by the instructions from the shore. These allow the acoustic sensors to be set at different points of the deep underwater neutrino telescope infrastructure. The architecture of GASIK measuring

systems provides a possibility of increasing the number of measuring points (receivers) at buoy stations if needed.

The coordinate measurement cycle is initiated by the shore control computer that transmits a synchronizing pulse (common start) to the controllers of all TSDs and receivers via cable communication lines. The controllers execute their programs. A TSD emits coded request signals sequentially for each transponder. A corresponding transponder emits a 32.768 kHz response signal of 1 ms duration. The TSD and receiver controllers measure arrival times of TSD request and transponder response signals. The propagation time of acoustic pulse from a TSD to a transponder and back to the TSD is recorded in the TSD counter (τ_{k0} , where κ is the transponder number). Receivers can measure propagation times from a TSD to a transponder and from the transponder to a receiver (τ_{ki} , where i is the receiver number) and from a TSD to a receiver (τ_{0i}). The distance from the position of i -th receiver hydrophone to the position of k -th transponder R_{ki} , is defined as:

$$R_{ki} = (\tau_{ki} - \tau_{k0}/2)C(z),$$

where $C(z)$ is the sound velocity.

To reconstruct the receiver hydrophone coordinates from the GASIK measurement results, the Cartesian coordinate system is used, where x axis is directed from south to north, y axis, from west to east, and z axis is vertically upwards directed; the origin corresponds to a depth of 1367 m (the conventional bottom at the telescope's *hydrological* string position). The spatial position of hydrophone of i -th receiver is defined as the intersection of spheres centered at the transponder positions with radii equal to the R_{ki} from the hydrophone of the k -th transponder to the receiver hydrophone. The receiver coordinates x_i , y_i , and z_i satisfy the set of equations:

$$R_{ki}^2 = (x_i - x_k)^2 + (y_i - y_k)^2 + (z_i - z_k)^2, \quad k = 1, 2, 3.$$

To solve this set of equations, the following iterative procedure is used: subtracting the third equation from the first and second ones, we derive the linear set of equations defining x_i and y_i as linear functions of z_i . Substituting $x_i = x(z)$ and $y_i = y(z)$ into the initial set of equations, we find the equation for z_i . For each iteration $C(z)$ is taken at z which was derived during the previous iteration. This iteration procedure rapidly converges; usually three iterations are enough at a calculation accuracy of 1 cm.

The GASIK is operated since 1994 as a part of Baikal neutrino telescope infrastructure. Analysis of long-term GASIK measurements has shown that NT200 strings mainly displace insignificantly during a year: receivers in the lower parts of the strings at 175 m from the bottom displace by not more than 40 cm, and those fixed immediately above the upper OMs at 260 m from the bottom, by not more than 60 cm (Fig. 5.1.2). The telescope moves in concord: the movement begins and ends almost simultaneously, despite certain freedom of string junction at the upper carrier frame of the telescope. The deviation of upper buoyancy (about 22 m depth) at the telescope-carrier buoy station is usually within several tens of meters. The telescope strings repeat movements of the upper buoy, deviating from the initial position by less than 1 m. Maximum deviation of the upper buoy attained 50 m during autumn storms; the maximally observed deviations are 1.3 m for the telescope top and 1 m for the telescope bottom. The vertical deflection of the telescope was not more than 1 degree in all such

cases. The telescope displaced relative to the initial position as a rigid unit.

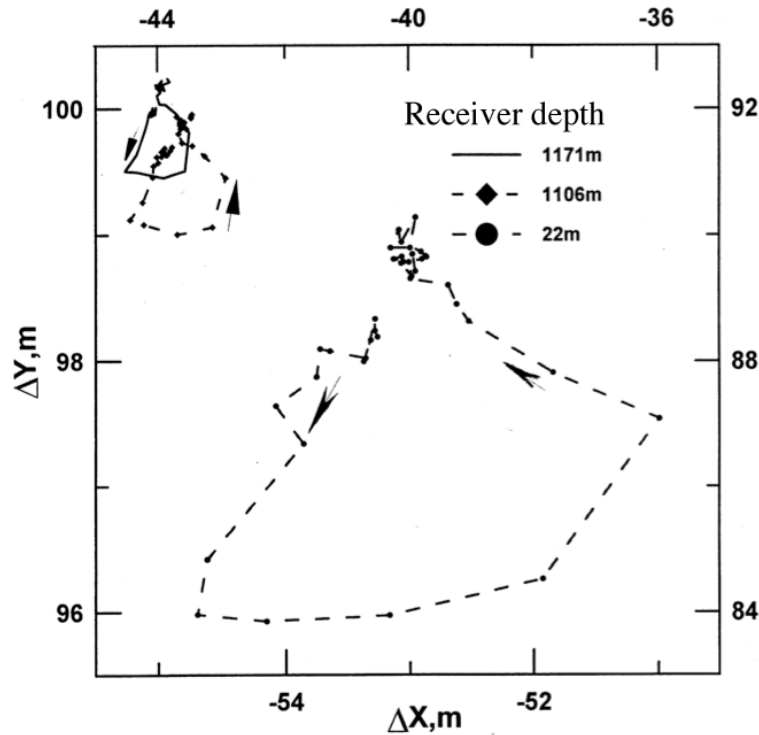


Fig. 5.1.2: Example of the NT200 displacement due to the water currents. The solid and the dashed-dotted curves – receivers at 1171 m and 1106 m depths, respectively (the left and bottom coordinate axes); the dashed curve – receiver at 22 m depth (right and top coordinate axes).

In contrast to the NT200 setup, the strings of the BAIKAL-GVD neutrino telescope, hanged to buoy stations, have not rigid junctions with other strings and will behave as buoy stations of the external strings of the NT200+ telescope. Such separate buoy stations displace significantly more than connected buoy stations of the NT200 neutrino telescope. Displacements of two receivers of the first NT200+ external string fixed at distances of 4 m (R-89) and 190 m (R-95) from the bottom, recorded by GASIK during 2010, are shown in Fig. 5.1.3. Displacements of receivers of the NT200+ external strings before and during the storm of August 17, 2010 are shown in Fig. 5.1.4.

As follows from Fig. 5.1.3, displacements are usually not more than 1–2 m in the period of open water. However, receivers, fixed at a distance of only 190 m from the bottom, displaced by about 10 m in certain days. Such strong deviations of buoy stations are usually caused by surface storms, which can last from several hours to several days. The maximum observed instant deviation velocity was about 14 m/h, and a deviation velocity of 6 m/h was observed for one of receivers during about 50 minutes.

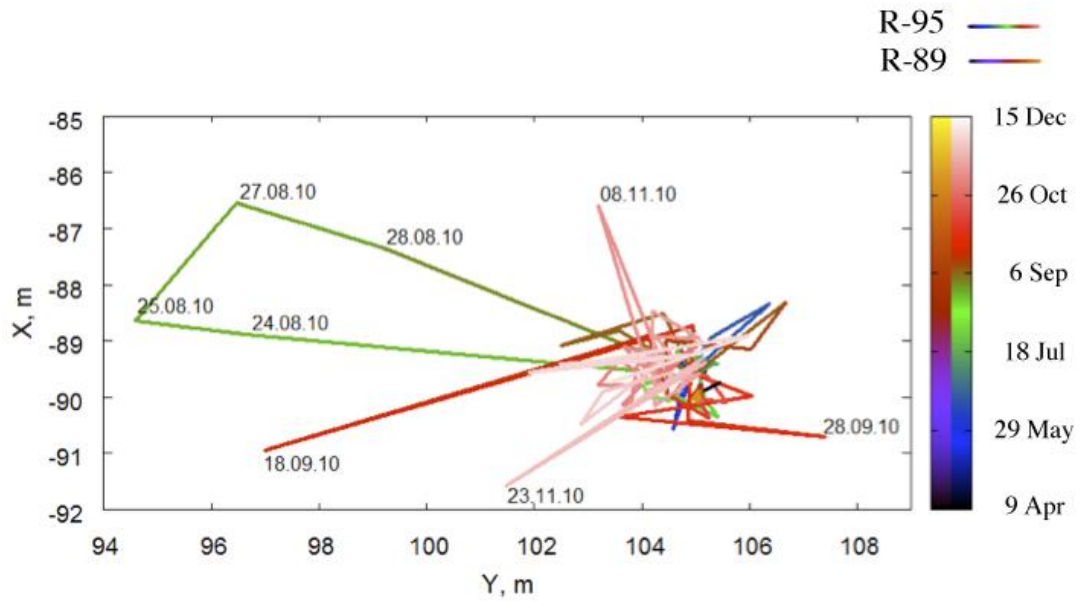


Fig. 5.1.3: Displacements of two receivers of the first NT200+ external string fixed at distances of 4 m (R-89) and 190 m (R-95) from the bottom during April 9 – December 4, 2010.

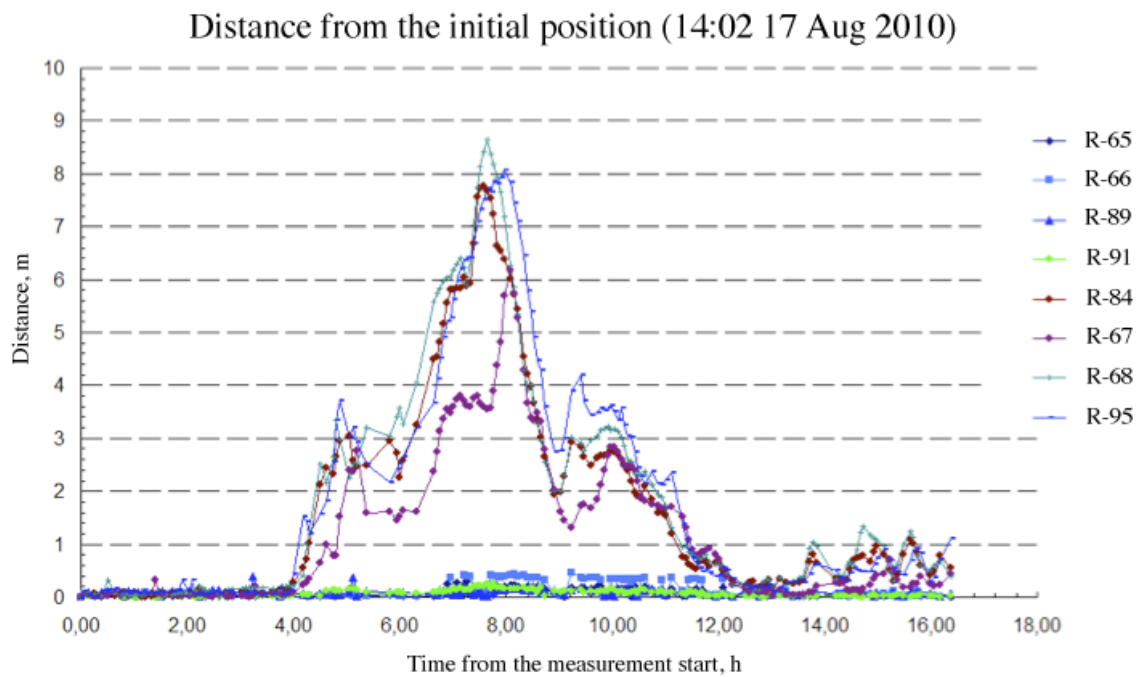


Fig. 5.1.4: Displacements of receivers of the NT200+ strings before and during the storm of August 17, 2010. 1st str.: R-95 (190 m) and R=89 (4 m); 2nd str.: R-67 (189 m) and R-65 (4 m); 3rd str.: R-68 (189 m) and R-66 (4 m); instrumentation string with laser light source: R-84(45 m); hydrological str.: R-91(11 m).

5.2 Positioning System of the BAIKAL-GVD

The architecture of the positioning system of the BAIKAL-GVD neutrino telescope (GASIK-GVD) is an elaboration of the GASIK NT200+ with accounting for the increasing setup sizes and accumulated experience of its operation. The system includes the shore and underwater computers, underwater transponders fixed near the bottom on some BAIKAL-GVD buoy stations and around the telescope, transponder start drivers (TSD), and receivers.

The principal difference of the new positioning system is the use of frequency-modulated (FM) signals instead of monochromatic ones, which were used in the NT200 GASIK. The use of wideband FMs allows suppression of interference effects caused by multipath propagation of acoustic signals in the hydroacoustic channel and more precise measurement of acoustic signal arrival time. Moreover, using of frequency-modulated (FM) signals allows to suppress influence of interference of acoustic signals with different paths which leads in some cases to communication problems between underwater acoustic devices.

Newly developed *transmitter-receivers* (modems) of all-round action for the BAIKAL-GVD positioning system satisfy the following requirements:

- working depth up to 1500 m;
- operating frequency range 20–40 kHz;
- maximum coverage range up to 2500 m;
- data transmission rate 2400--9600 bit/s;
- coordinate measurement accuracy is not worse than 20 cm.

The block-diagram of a hydroacoustic *transmitter-receiver* is shown in Fig. 5.2.1. The processor unit (PU) controls the reception, identification, and transmission of acoustic signals. A signal from the hydrophone (Hp) comes to the input signal amplifier (*input SA*). The input SA unit amplifies a signal within the operating frequency range with the coefficient equal to 1000. The signal from input SA is fed to the PU, where the input packet is identified and the solution about formation of a response packet is made. The response packet in digital form is fed to the output signal amplifier (*output SA*), which amplifies and forms the packet for transmission via the acoustic channel through the Hp. The amplitude of a signal fed to the hydrophone is 48 V and the power is 20 W. The power supply (PS) feeds 5 V to Hp and 12 V to other units. All tasks of detection and formation of acoustic signal packets are solved by the PU, the circuit diagram of which is shown in Fig. 5.2.2. A PIC18F4320 microcontroller operates at a frequency of 20 MHz, specified by a quartz oscillator. The ADM666A current stabilizer chip supplies the controller. An analogous input signal comes to the microcontroller comparator input to measure the signal level. The signal from the comparator output comes to the comparison/capture unit in the capture mode to measure the time of signal arriving. A response signal is formed in the comparison/capture unit in the pulse-width modulation (PWM) mode. All parameters of the capture unit, comparator, and ADC are specified by the microcontroller program. The FM pulses from the outputs of PWM microcontroller come to the inputs of two IR2104S key drivers controlling four IRFZ44N transistors. The PU chip supplies current of 8.5 mA in microcontroller active mode. The circuit diagram of the input signal analyzer and amplifier is shown in Fig. 5.2.3.

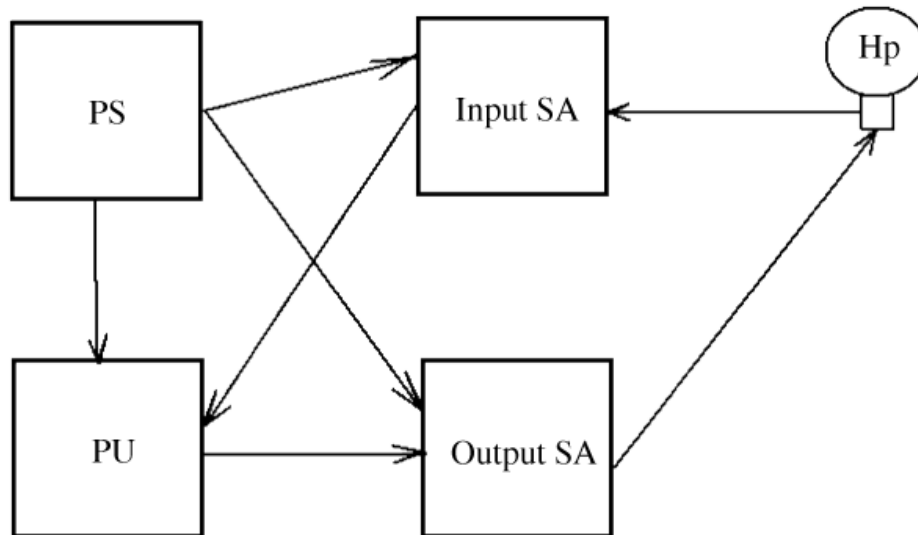


Fig. 5.2.1: Block-diagram of the hydroacoustic transmitter-receiver with the frequency modulation.

The frequency modulation with minimum shift (Minimal Shift Keying - MSK) has been chosen for the GASIK-GVD. The modulation is carried out without phase jumps, and frequency changes at the instants of zero-level carrier intersection. In MSK, the values of frequencies corresponding to logical “0” and “1” differ by the value equal to a half of the data transmission rate. In other words, the modulation index is equal to 0.5:

$$m = |f_1 - f_0|T,$$

where T is one bit transmission time. For example, if the transmission rate is equal to 9600 bit/s, a MSK signal is formed from oscillations with frequencies of 27600 Hz and 32400 Hz, corresponding to logical “0” and “1”. These frequencies fall into the operating frequency range of the hydrophones in use and have been taken as working frequencies in the given device. The HDLC protocol of high-end control of the data transmission channel, which is a published ISO standard and basic for constructing other channel protocol, has been taken as a protocol basis. The protocol data unit format is shown in Fig. 5.2.4.

The universal hydroacoustic *transmitter-receivers*, designed on up-to-date element basis, were successfully tested in situ in Lake Baikal during 2010-2011. They completely support the GASIK-NT200+ operating protocol and also provide operation of the protocol with FM for system modification. The developed *transmitter-receiver* can operate as a transponder and as TSD or receiver in the presence of wire communication.

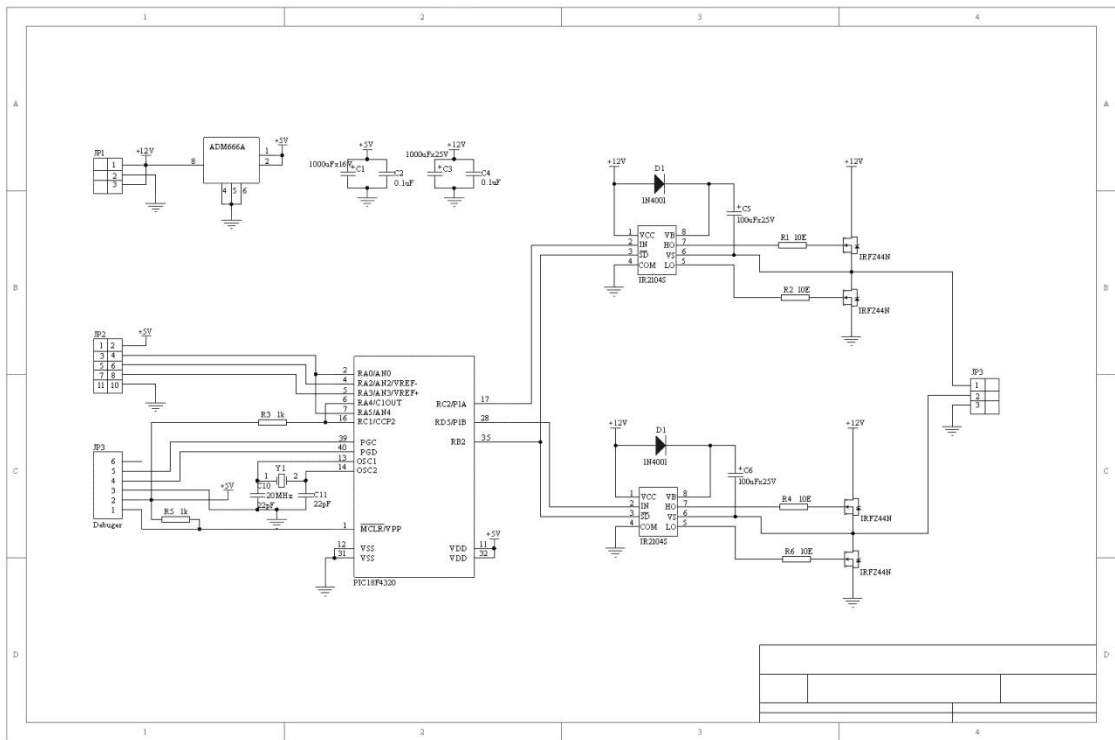


Fig. 5.2.2: Circuit diagram of the PU chip.

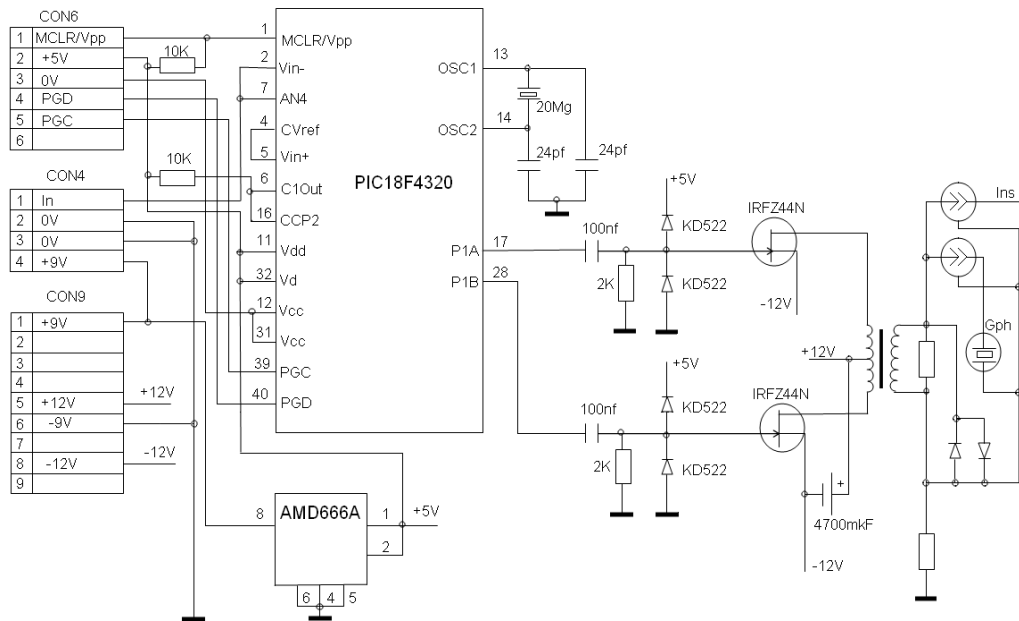
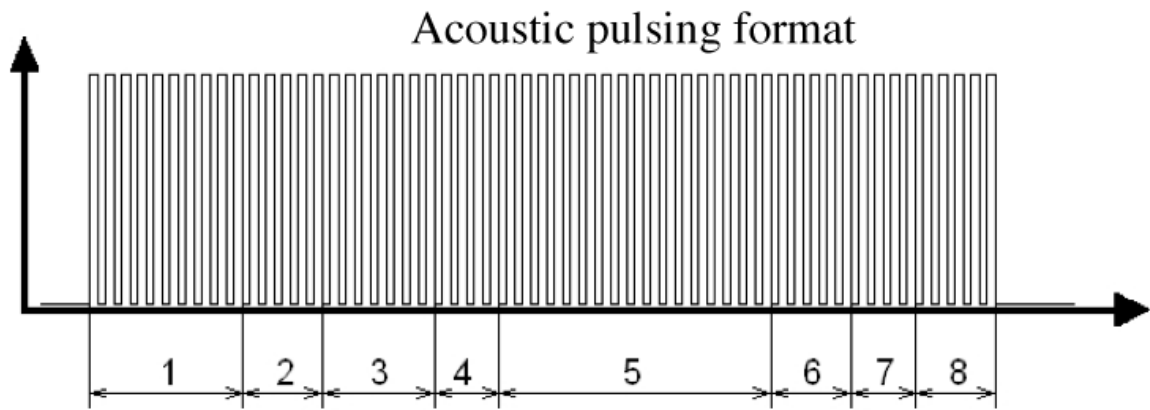


Fig. 5.2.3: Circuit diagram of the input signal analyzer and amplifier.



1. Wake-up signal - 0.3 ms
 2. Frame start flag - 6 bits (011110)
 3. Address field - 10 bits
 4. Control field (instruction) - 4 bits
 5. Data field - 32 bits
 6. Frame-control sequence (CRC) - 7 bits
 7. Frame end flag - 6 bits (011110)
 8. Time-stamp – 6 MSK periods
 - "0" frequency - 32400 Hz
 - "1" frequency - 27600 Hz
- Pulsing length is 8 ms at a transmission rate of 9600 bit/s
 Pulsing length is 29 ms at a transmission rate of 2400 bit/s

Fig. 5.2.4: Protocol data unit format.

6 WATER OPTICAL PROPERTIES

The interpretation of the experimental data taken with an underwater neutrino telescope requires a reasonably precise knowledge of water optical properties. The inherent optical properties (IOPs) generally chosen as a measure for absorption and scattering phenomena depending on a light wavelength λ in natural water are: (I) the absorption coefficient $a(\lambda)$ (or the absorption length $L_a = 1/a$), (II) the scattering coefficient $b(\lambda)$ (or the scattering length $L_b = 1/b$), (III) the attenuation coefficient $c(\lambda) = a(\lambda) + b(\lambda)$ (or the attenuation length $L_c = 1/c$), (IV) the scattering phase function $\chi(\gamma, \lambda)$, where γ is the scattering angle. Since the values of the IOPs in natural water vary with time, a long-term *in situ* monitoring of IOPs is mandatory to operate a neutrino telescope. The measurement of the IOPs is also one of the central tasks in physical oceanology and limnology: light absorption and scattering effects in water can provide important information on the concentration of dissolved organic matter and suspended forms of organic matter, their mutual transformation, the rate of sedimentation, as well as on other important biological and physical processes in natural basins.

A lot of different instruments - commercial and custom designed - have been constructed for measurement of optical water parameters. Most of them use short transmission cells with a fixed length of the light path (see e.g. [57] and references therein). These techniques require careful calibration procedures with pure water or nitrogen before each measurement in order to evaluate the cell characteristics. They are therefore not well suitable for a long-term operation under water. This is the motivation to develop new devices and methods for monitoring the IOPs of water at the sites of neutrino telescopes. In order to avoid the necessity of knowing precisely the parameters of the device, the light path must be variable. In this case, signal amplitude versus distance can be measured and optical parameters determined by a fit.

We have constructed an instrument for long-term *in situ* monitoring of the inherent optical properties of deep water, ASP-15 [58]. The acronym stands for Absorption, Scattering and Phase function meter, working at 15 wavelengths of visible light. ASP-15 can be either operated from the ice cover of Lake Baikal (non-stationary mode using during winter expedition), or installed on stationary, moored buoy-stations (stationary mode, in conjunction with the Baikal neutrino telescope), thus operating remotely controlled from the shore control station.

6.1 Determination of the Absorption Coefficient

The study of the IOPs with ASP-15 is based on the measurement of the light of a point-like isotropic source with time-independent intensity. The light field is characterized by the differential flux of photons defined as $B(\vec{R}, \vec{\Omega}) = dN/(dSd\vec{\Omega})$, where dN is the number of photons, passing an area dS at a spatial point with coordinate \vec{R} in direction $\vec{\Omega}(\theta, \varphi)$ within a solid angle $d\Omega = \sin \theta d\theta d\varphi$. For a point-like isotropic source the differential flux depends only on the distance $R = |\vec{R}|$ from the source and the angle θ between direction vector $\vec{\Omega}$ and coordinate vector \vec{R} : $\cos \theta = (\vec{\Omega}, \vec{n})$, where $\vec{n} = \vec{R}/R$.

Let us define $N_0(R)$, $N_1(R)$ and $N_2(R)$ as:

$$N^o(R) = \int_0^{2\pi} d\varphi \int_0^\pi B(R, \theta) \sin \theta d\theta, \quad (6.1)$$

$$N_1 = \int_0^{2\pi} d\varphi \int_0^{\pi/2} B(R, \theta) \cos \theta \sin \theta d\theta, \quad (6.2)$$

$$N_2 = \int_0^{2\pi} d\varphi \int_{\pi/2}^\pi B(R, \theta) \cos \theta \sin \theta d\theta. \quad (6.3)$$

Here, $N^o(R)$ is the spatial illuminance at distance R from a source, which is derived from an integration of the differential flux $B(\vec{R}, \vec{\Omega})$ over all directions of photons; $N_1(R)d\vec{\sigma}$ and $N_2(R)d\vec{\sigma}$ are the numbers of photons, leaving and entering the spherical surface with radius R through an elementary fixed area $d\vec{\sigma}$ (the orientation of $d\vec{\sigma}$ is given by the vector $\vec{n} = \vec{R}/R$). Given the photon current through a spherical surface $S(R) = 4\pi R^2$:

$$J(R) = 4\pi R^2 \int_0^{2\pi} d\varphi \int_0^\pi B(R, \theta) \cos \theta \sin \theta d\theta = 4\pi R^2 (N_1(R) - N_2(R)), \quad (6.4)$$

the number of photons which are absorbed in the volume $dV = 4\pi R^2 dR$ between two spherical surfaces $S(R)$ and $S(R + dR)$ around the light source, has to be equal to the difference of photon currents through $S(R+dR)$ and $S(R)$:

$$dJ(R) = -a dV \int_0^{2\pi} d\varphi \int_0^\pi B(R, \theta) \sin \theta d\theta, \quad (6.5)$$

where a is the absorption coefficient of light in water. Taking into account eqs.(6.1)-(6.4), the following expression for the absorption coefficient a can be derived from eq.(6.5) [59, 60]:

$$a = - \frac{1}{N^o(R)R^2} \frac{d([N_1(R) - N_2(R)]R^2)}{dR}. \quad (6.6)$$

So, to determine the absorption coefficient a , one has to measure three photometric characteristics, as a function of R : $N_1(R)$, $N_2(R)$ and $N^o(R)$. Some approximations are applicable to make this method more suitable for practical use. For water with a strongly forward-peaked scattering phase function $\chi(\gamma)$ as typical for clean sea and Lake Baikal waters, one has:

$$[N_1(R) - N_2(R)]/N_0(R) \approx 1.$$

Usually, also the following condition turned out to be applicable in natural water:

$$d[N_1(R)R^2]/dR \gg d[N_2(R)R^2]/dR.$$

The absorption coefficient a can be determined by simplifying expression (6.6) to

$$a \approx - \frac{1}{N_1(R)R^2} \frac{d[N_1(R)R^2]}{dR} = - \frac{d \ln[N_1(R)R^2]}{dR} \quad (6.7)$$

and measuring only $N_1(R)$.

With the ASP-15 instrument, we have carried out some thousand measurements of the absorption coefficient of water at various wavelengths in the visible range. Usually, an excellent agreement of experimental data with the exponential law behavior of the $N_1(R)R^2$ according to the expression (6.7) is observed (see the examples in Fig. 6.1). It proves the applicability of the method as well as the quality of the data.

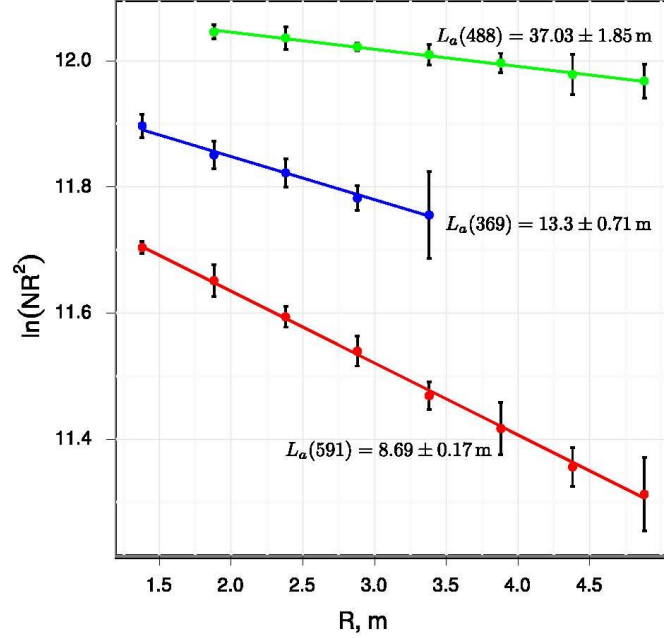


Fig. 6.1: The measured dependence of $\ln(NR^2)$ on distance R , for three different wavelengths.

6.2 Determination of the Scattering Coefficient

The method which is used for determination of the scattering coefficient is the logical continuation of the previous one. For the same conditions and approximations as in the previous part the total number of photons N_t (let us denote it N_t) from an isotropic point-like source hitting the unit area of a detector is:

$$N_t(R) \approx \frac{N_0}{4\pi R^2} \exp(-aR), \quad (6.8)$$

where N_0 is a source intensity.

The number of photons N_t is added up from two samples of photons, which reach the detector. The first sample consists of direct photons, which were not scattered before hitting the detector. Their number N_d decreases with distance from the source as:

$$N_d(R) = \frac{N_0}{4\pi R^2} \exp(-cR), \quad (6.9)$$

where $c = a + b$. Photons from the second sample were scattered before they hit the detector. Placing a screen with diameter D at a fixed distance $r \ll R$ from the isotropic, point-like source, one can measure the number N_s of those scattered photons:

$$N_s(R) \approx N_t - N_d = \frac{N_0}{4\pi R^2} [\exp(-aR) - \exp(-cR)]. \quad (6.10)$$

Measured N_s and N_t , the value of the scattering coefficient b can be estimated as:

$$b \approx - \frac{\ln(1 - N_s/N_t)}{R}. \quad (6.11)$$

So, we do not need to know N_0 , which cannot be kept constant over times typical for stationary mooring. In reality, apart from scattering, diffraction at the edge of the screen will contribute additional photons hitting the detector. In practice the onset of diffraction can easily be determined by moving source and screen with respect to the detector. We have measured $N_s(R)$ and $N_t(R)$ at different distances R and then calculate the value

$$A(R) \approx - \frac{\ln(1 - N_s/N_t)}{R}. \quad (6.12)$$

Fig. 6.2 shows the dependence of $A(R)$ on R , measured at two different depths. The three ranges (I), (II) and (III) as indicated in Fig. 6.2 correspond to direct light (as defined by simple geometry), dominance of diffracted light, and scattered light, respectively. Note that at 4 m depth scattering is so strong, that scattered light overshines any diffraction contribution as soon as the direct-light region is left. At greater depth, scattering is smaller and the R -range of diffraction dominance is clearly identifiable. In other words: $A(R)$ (eq. 6.12) equals b (eq. 6.11) at distance $R > R_b$, where A is constant. R_b increases with decreasing b .

The scattering coefficient may be represented as the sum of the forward and backward scattering coefficients: $b = b_{\text{fwd}} + b_{\text{back}}$. Results of MC-simulations show that for the case of a point-like isotropic source and strongly anisotropic phase functions the flux of photons at distance R from the source is formed mainly by the photons which were emitted within a cone with half angle about 30 - 60 degrees around \vec{R} . This means that our estimation of b coincides with b_{fwd} within the experimental errors. An estimation of b_{back} can be derived from the measured value of $b_{\text{fwd}} \cong b$ and from the value of the asymmetry coefficient K of the scattering phase function, which is defined as:

$$K = \frac{b_{\text{fwd}}}{b_{\text{back}}}.$$

An estimation of K is derived from the ratio K_{exp} of detected photons which were emitted by unscreened and screened isotropic source, respectively. It was shown that K_{exp} is a good estimation of K with an accuracy of about 15%.

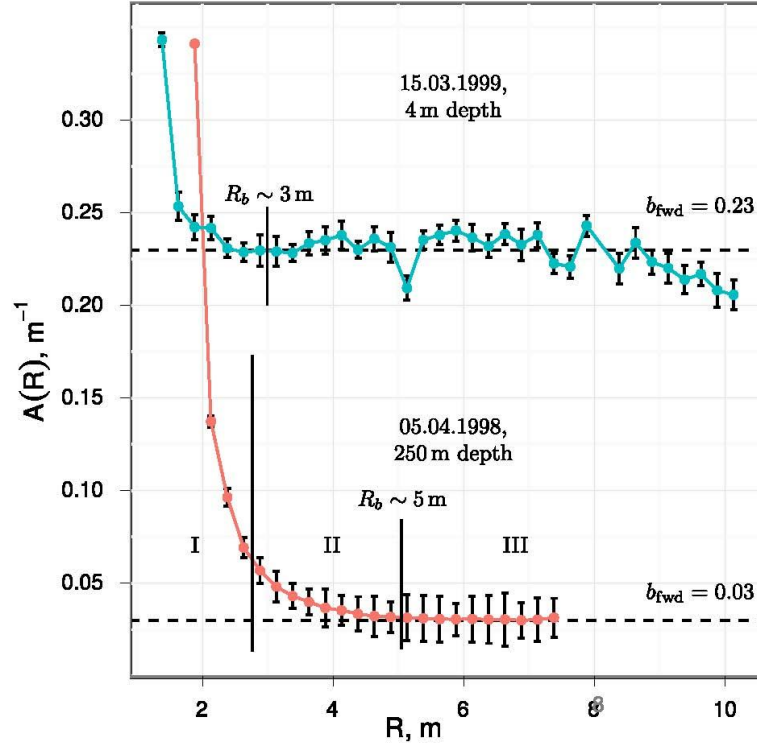


Fig. 6.2: Dependence of the value $A(R)$ on the distance R between source (shadowed by a screen) and detector, at depths 4 m and 250 m.

6.3 Determination of the Scattering Phase Function

In the single-scattering approximation, the number of photons $N(\alpha, R)dSd\Omega$ (Fig. 6.3) hitting a detector area element dS within a solid angle $d\Omega$ at an angle α from the source-detector axis is [61]:

$$N(\alpha, R)dSd\Omega = b \frac{N_0 dSd\Omega}{R \sin \alpha} \int_0^{\pi-\alpha} \chi(\alpha + \theta) \exp\left[-cR \frac{\sin \alpha + \sin \theta}{\sin(\alpha + \theta)}\right] d\theta. \quad (6.13)$$

Here N_0 is the source intensity, $\chi(\alpha+\theta)$ is the scattering phase function. For small α one can derive from the (6.11) the following expression:

$$\chi(\alpha) \approx -\frac{R}{bN_0} \exp(cR) \frac{d[N(\alpha, R) \sin \alpha]}{d\alpha}. \quad (6.14)$$

Eq. (6.14) is used for an estimation of the scattering phase function by measuring the number of photons under different angles α .

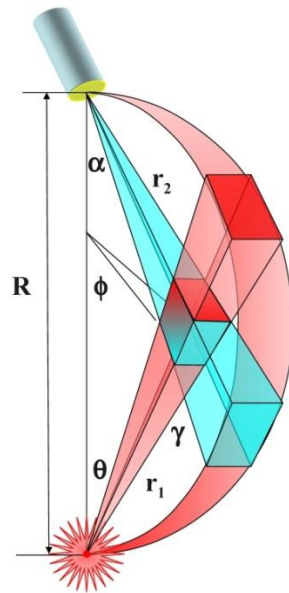


Fig. 6.3: Definition of angles and distances for single-scattered photons from an isotropic light source.

6.4 Long-Term Monitoring of Water Optical Properties

A sketch of ASP-15 is shown in Fig. 6.4. The water-tight container which houses the electronics block, two PMTs, light filters and a step motor is made from an aluminum tube with diameter 200 mm, 1000 mm length and a wall thickness of 30 mm. The ends of the tube are closed with two flat aluminum lids with thickness 40 mm. The total weight of the equipped container is about of 60 kg in air. There are two organic glass illuminators in the middle part of the tube.

Outside of the container, in the water, there are two light receiving channels: channel 1 with a wide aperture which is used for a and b measurements, and channel 2 with a narrow 0.5° aperture for the measurement of the scattering phase function. Channel 1 is equipped with a milk glass window with 40 mm diameter and 5 mm thickness. This window is followed by a long tube with black inner surface, which limits the aperture for the light hitting the interference filters to 10° . Channel 2 is equipped with a mirror and a shutter with 30 cm length and 15 mm diameter, which are rotated by a step motor over an angular range of 360° , with a step of $2'$. Photons reflected by this mirror pass the glass window, a collimator with an aperture of 0.5° and a light filter, and eventually hit PMT-2. The shutter protects the receiver 2 from direct light during the measurement of the scattering phase function.

PMTs of type FEU-130 operating in photon rate counting mode are used as receivers. Non-linearities of the receivers are less than 1% over a dynamic range up to 10^5 Hz and can be remotely controlled by two LEDs with adjustable brightnesses. The PMT dark current is about 30Hz.

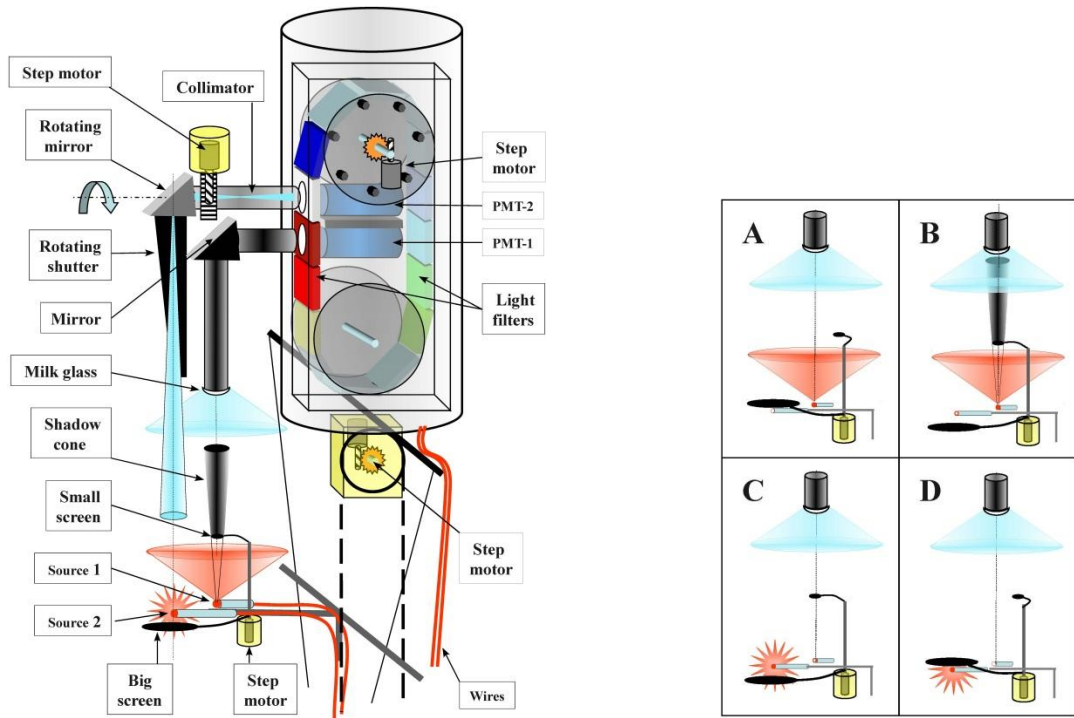


Fig. 6.4: Left: The ASP-15 device (including the light sources with screens, moveable up to 8 m away from the receiving unit). Right: Outline of the operation modes.

There are 15 interference light filters with bandwidth 3-5 nm in the range 350-690 nm. Light filters are arranged in plastic frames and connected to a caterpillar-like structure. A step motor moves the caterpillar which changes the light filters in front of PMT-1 and PMT-2. Also there is an empty frame in the caterpillar, which is used for the measurement of the scattering phase function.

On the outer side of the bottom lid, a step motor with a gear filled with oil is mounted. The motor rotates a block with a strained cable loop of 15 m length. A light-weight platform mounted on the cable has two light sources and two shadowing screens. Light sources and screens can be moved vertically from $R = 0.5$ m to $R = 15$ m with respect to the light receiving channels.

Tiny halogen lamps KGMN-27 in hermetical quartz tubes are used as light sources. Supply voltage and current of the lamp is 27 V and 100 mA, respectively. The optimal lamp brightness depends on the used light filter and is controlled by 8-bit digital-to-analogue converter. It is chosen in a way that the linear dynamic range of the PMT is not exceeded. The electrical current through the lamp is stabilized at a level of 0.01%. The light source 1 is covered with a light-tight cup with an aperture $d = 0.8$ mm through which light is emitted within a cone with full angle of about 60° . The axis of the light cone is directed towards the center of channel 1. Between the source 1 and the milk glass window, at a fixed distance $r = 30$ cm from the source, a small shadowing screen with diameter of $D = 3$ mm (shadowing angle 0.5°) is arranged.

The size of the isotropic light source 2 is about 10 mm. Source 2 can be shadowed by a big screen with diameter 3 cm, which is placed at a distance of 3 mm from the source. Source 2 is located below channel 2. Both screens can be moved simultaneously in the horizontal plane for shading the light sources. The movement of screens is performed by the tiny step motor.

The power is supplied over one wire and the armoring of a 7 km long multi-core cable on the bottom of Lake Baikal. The voltage of the power supply is 300 V, the maximal current is 300 mA.

The deployment of ASP-15 for long-term operation, as well as lifting for preventive maintenance and the performance of methodological and research measurements are made in March-April each year from the ice cover of Lake Baikal. Instrument operation, data acquisition and transmission are carried out by a controller and power line modem. The modem uses PWM (Pulse Width Modulation) for signal transmission via a 7-km cable to shore. The measurement of optical parameters of the water is performed by the shift operator or remotely via the Internet.

6.5 Measurement Procedures

The absorption spectrum

To measure the absorption spectrum, the isotropic light source 2 (see Fig. 6.4) is moving automatically over distances which make the best use of the dynamic range of the device and are specific for each of the light filters. The measurement of $N(R)$ is made at ten distances and $a(\lambda)$ is determined for each filter. During the measurement, the stability of the light source intensity is about 0.1%. This process is remotely performed by shift operator at the shore and runs automatically over all filters.

The scattering spectrum

To measure the scattering spectrum, the distance R_b (see Fig. 6.2) has to be determined by evaluating the dependence of $A(R)$ vs. R for each of the light filters. Then both light sources are moved to a distance $R = R_b$, source 1 is turned on, $N_t(\lambda)$ (Fig. 6.4 right, step A) and $N_s(\lambda)$ (Fig. 6.4 right, step B) are measured and the scattering spectrum is calculated according to eq. (6.12). After that, source 1 is turned off and source 2 is turned on, followed by the measurement of the total and the backscattered light from this source (Fig. 6.4 right, steps C and D). The series of these four measurements allows estimating $b = -\ln(1-B/A)/R$ and $K = nB/D$, and calculating $b_{\text{back}} = b/K$. Here the normalization coefficient n is the ratio of source intensities, $n = C/A$, and A, B, C, D are the results of the measurements in the respective steps defined in Fig. 6.4, right panel. Again, this process is remotely performed by the shift operator at the shore and runs automatically over all distances and filters.

The scattering phase function

First, the frame without a filter is moved in front of PMT-2. Then, both light sources are moved to their minimum distance to receiver 2, source 2 is turned on and source 1 is turned off. The instrument is ready to measure the scattering phase function. Then the measurement is done by rotating the mirror in steps of 2' between 0° and 360°. This process is performed remotely from shore, but requires the manual control of an expert.

6.6 Light Absorption in Lake Baikal Water

Typical distribution of the Baikal water absorption coefficient at a depth of 1000 m versus λ is usually within the blue region in Fig. 6.5. As is seen from the figure, the spectra observed deviate from the mean by not more than 10%. The absorption coefficient usually slightly varies with depth (by 20–30%). Such relatively low variability in the absorption coefficient is connected with the stability of the mean concentration of soluble organic matter due to the dynamic equilibrium of the processes of organics brining, its assimilation by microorganisms, and their decay and sedimentation. Significant changes in the Baikal ecosystem are required for noticeable variations in the optical parameters of the water medium. The average absorption length in the spectral minimum (488 nm) is 22.7 m. The spectra of anomalously low absorption coefficient, observed in 1992 and 2001, are also shown in Fig. 6.5 for comparison. A similar decrease in the absorption coefficient was observed in other years as well (see, Fig. 6.6). This figure clearly shows the periods of anomalously low absorption coefficient and, hence, concentrations of soluble organic matter.

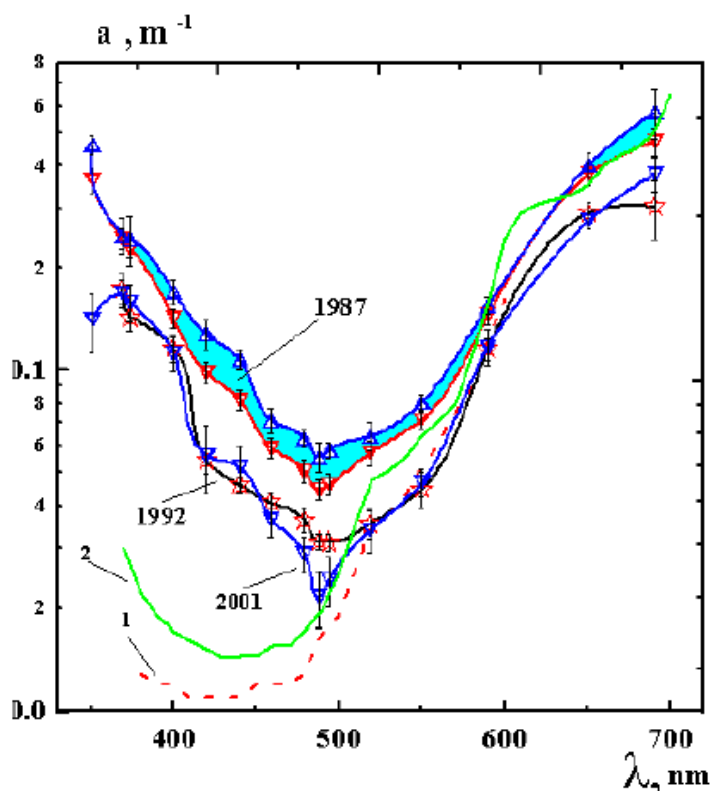


Fig. 6.5: Spectral dependences of the Baikal water absorption coefficient measured in different years. Spectra 1 and 2 have been obtained in measurements of the absorption coefficient in clean seawater [61, 62].

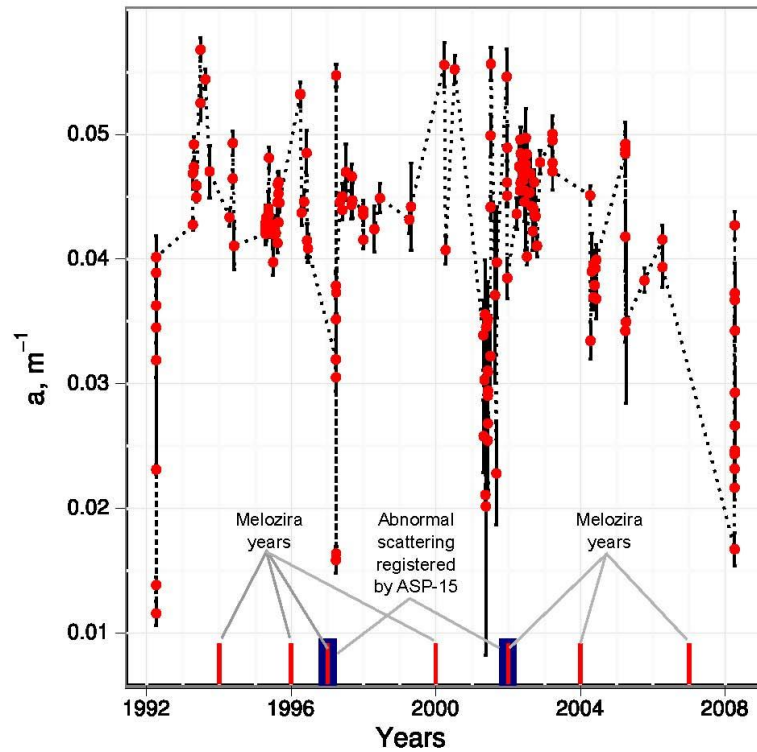


Fig. 6.6: Long-term behaviour of the absorption coefficient as measured between 1992 and 2008 at wavelength of 488 nm. Marks indicate periods of anomalously increased production of the seaweed *Melozira Baikalensis*.

6.7 Light Scattering in the Baikal Water

The variation of light scattering in Lake Baikal is much stronger than that of absorption. It changes with depth and time. At a given depth, variations in time may reach an order of magnitude. Fig. 6.7 shows the depth dependence of the scattering coefficient for $\lambda = 488$ nm as measured at March 3 2000. The profile changes from year to year, but the maximum gradient is always over the first 50 m of depth. In the deep zone (500-1100 m), b usually decreases by about a factor of 2, followed by a small increase close to the bottom of the lake. The typical scattering length is about 30 – 50 m during more than 80% of the calendar time at large depths, where BAIKAL-GVD optical modules are assumed to be located. Examples of scattering spectra at a depth of 800 m are presented in Fig. 6.8.

The asymmetry coefficient $K(\lambda)$ of the scattering phase function varies from 5 to 10 in deep water and from several tens to several hundreds in surface water. It is related to the size distribution of suspended particles.

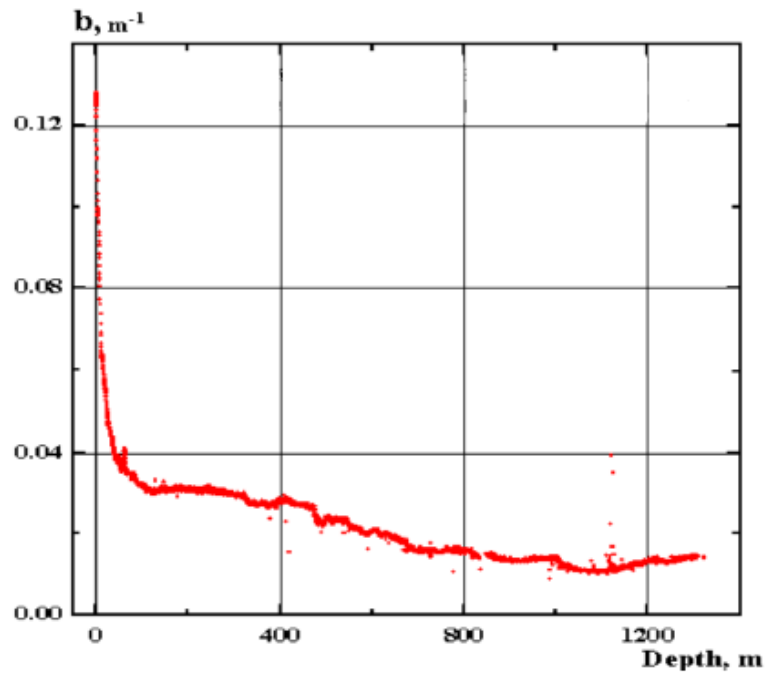


Fig. 6.7: Depth dependence of the light scattering coefficient near the NT200 site.

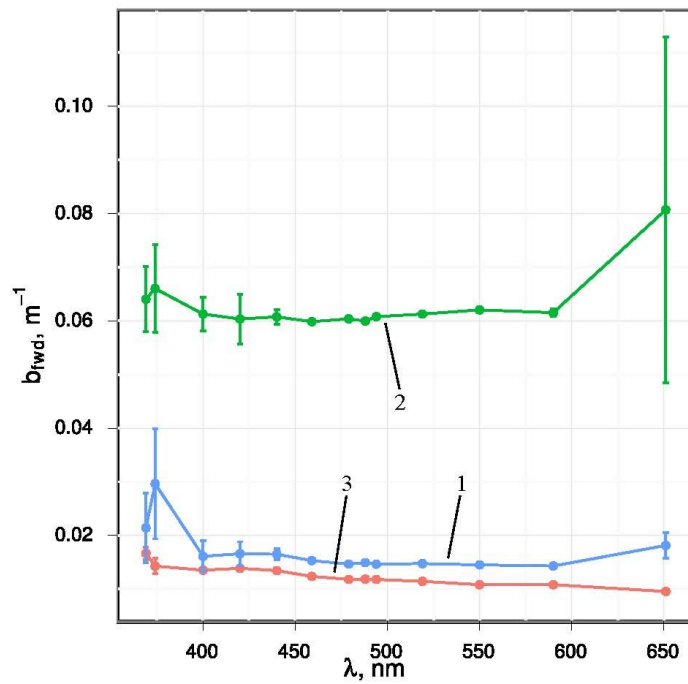


Fig. 6.8: Spectral dependence on the scattering coefficient b , measured at 800m depth in spring 2001. Curve 1 - April 4; 2 - April 6; 3 - April 8.

6.8 Scattering Phase Function

The scattering phase function for deep water in Lake Baikal is very forward-peaked - similar to clean sea water. Fig. 6.9 shows the scattering phase function (not normalized) for deep (top curve) and shallow (bottom curve) water. We used white light in order to be sensitive at large angles. The bottom curve in Fig. 6.9 decreases much faster with the angle than the top one, since the size of suspended material in surface layers is larger than in the deeper ones. The typical value of the average cosine of the scattering angles is about $\overline{\cos \gamma} = 0.9$ for deep Baikal water.

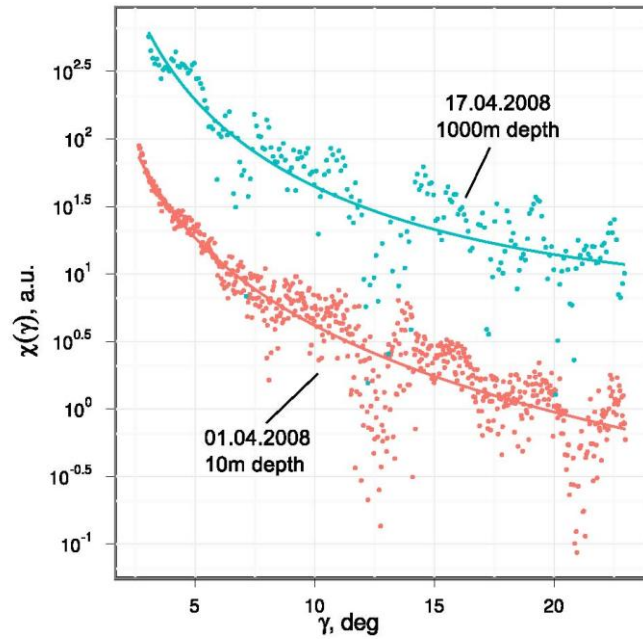


Fig. 6.9: Top curve: scattering phase function for white light (arbitrary units) at 1000m depth; bottom curve: the same for surface water.

The important parameter for interpreting results of neutrino telescopes is the so-called effective scattering length, $L_b(\text{eff})$. The effective scattering length is defined as

$$L_b(\text{eff}) = L_b / (1 - \overline{\cos \gamma}).$$

Actually there is a method to determine absorption length and effective scattering length with the help of the neutrino telescope itself. We have performed a corresponding experiment in 1997 [44] where we illuminated the photo-multipliers of the telescope by a distant, pulsed laser. From the dependence of the measured amplitudes and times on the distance between the laser and various photomultipliers, L_a and $L_b(\text{eff})$ at 475 nm wavelength could be determined, with $L_a = 22$ m and $L_b(\text{eff}) = 480$ m. Assuming $\cos \gamma = 0.9$, this corresponds to $L_b = 48$ m, which is well in the range of values determined with ASP-15. The agreement between the two complementary methods confirmed our trust in both methods.

7 Deployment

7.1 Cable Network

The layout of BAIKAL-GVD and schematic view of underwater communication network are shown in Fig.7.1-7.4. The main components of the cable network are:

- Main electro-optical cables (MEOCs), used for the connection of each GVD cluster DAQ-center to shore for power, data and control signal transmission;
- Interlink cables from cluster DAQ-center to sections on strings;
- OM-cables from section central module to each OM.

The first MEOC has been deployed in 2011 in Lake Baikal. The MEOC-cable is shown in Fig.7.5. It is a load-bearing cable with the protection polyethylene coating, which comprises three pairs of standard single-mode optical fibers in the copper tubes and three isolated copper conductors.

Load-carrying combined cable (see, Fig. 7.6) is used as interlink cable for connection of the strings with the cluster DAC-center. The cable comprises two coaxial pairs, screened twisted pair and three copper conductors.

The R.F. cable with 9 thin conducting wires and an Elastopan sheath (Fig. 7.7) is used for connecting optical modules with the central modules of sections.

All deep underwater cables of GVD were especially designed and manufactured by the “Pskov-GEOKABEL” (Russia) [63].

7.2 Carrier Structures

The carrier structures of the deep underwater neutrino telescopes in Lake Baikal are based on subsurface buoy stations (BSs). Under the lake surface the buoy stations are connected by subsurface jumper cables. The following types of buoy stations are used in the BAIKAL-GVD (Fig.7.8):

- SBS - string buoy stations, on which the active parts of telescope are located (Fig. 7.9);
- CBS - cable buoy stations, which are used to hold the sea ends of the MEOCs under the lake surface;
- DAQ-BS - buoy stations on which the DAQ-centers of each cluster are located;
- IBS, intermediate buoy stations, which are used as mechanical supports of subsurface cable lines;
- HBS, hydrometric buoy station, on which the equipment for monitoring the water parameters are placed.

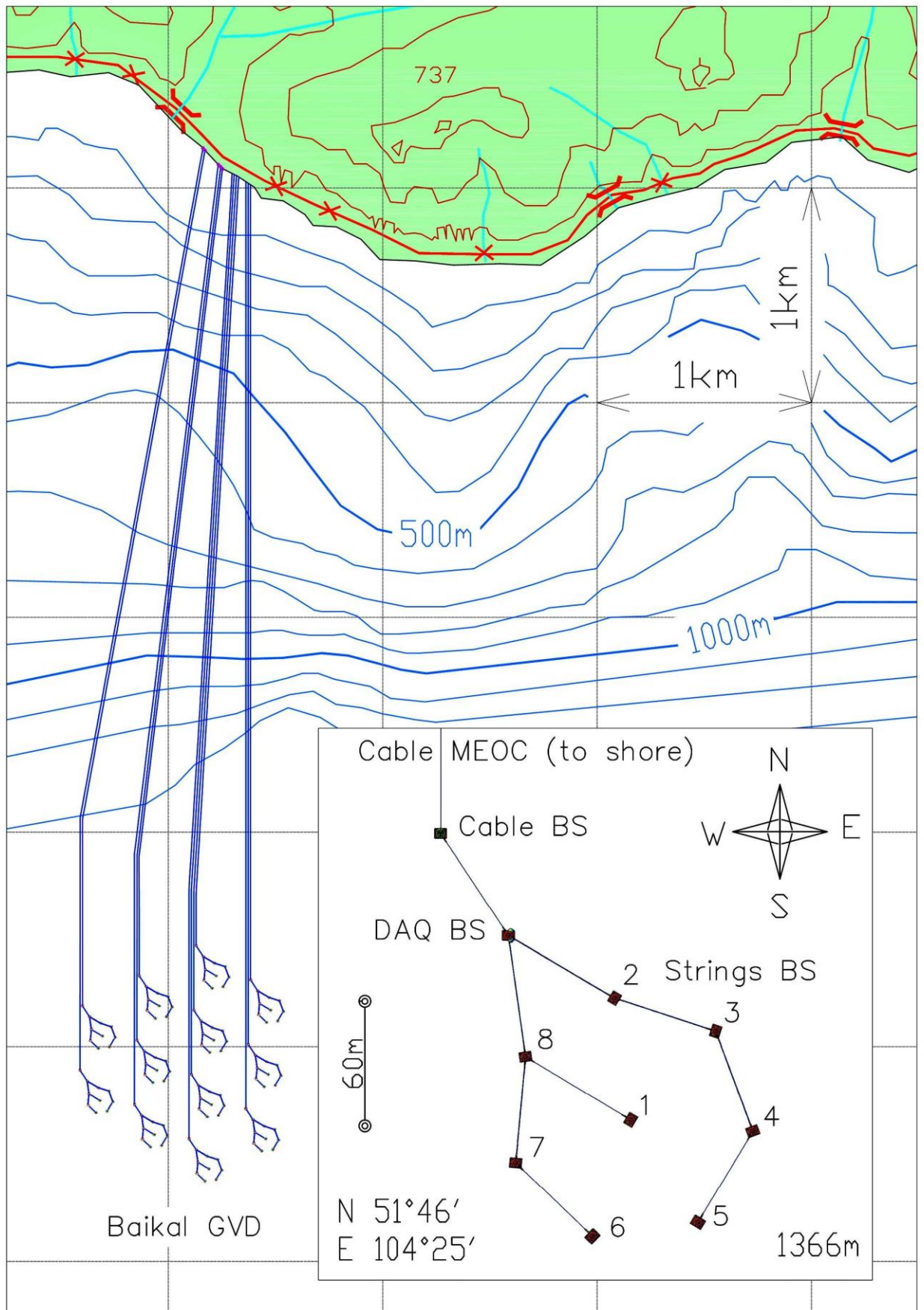


Fig. 7.1: Schematic view of the arrangements of the BAIKAL-GVD buoy stations and cable lines.

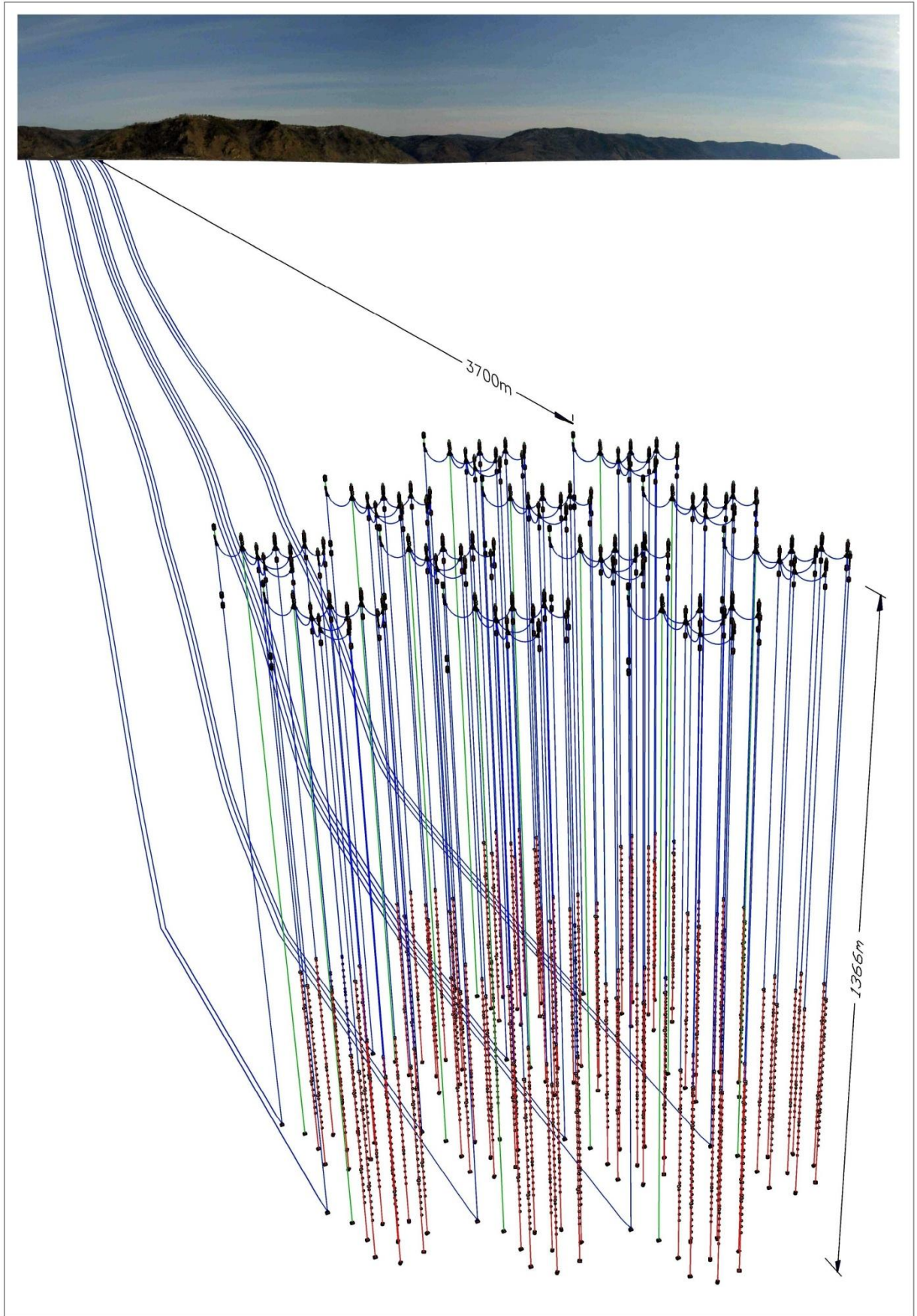


Fig. 7.2: Schematic view of the arrangement of the BAIKAL-GVD.

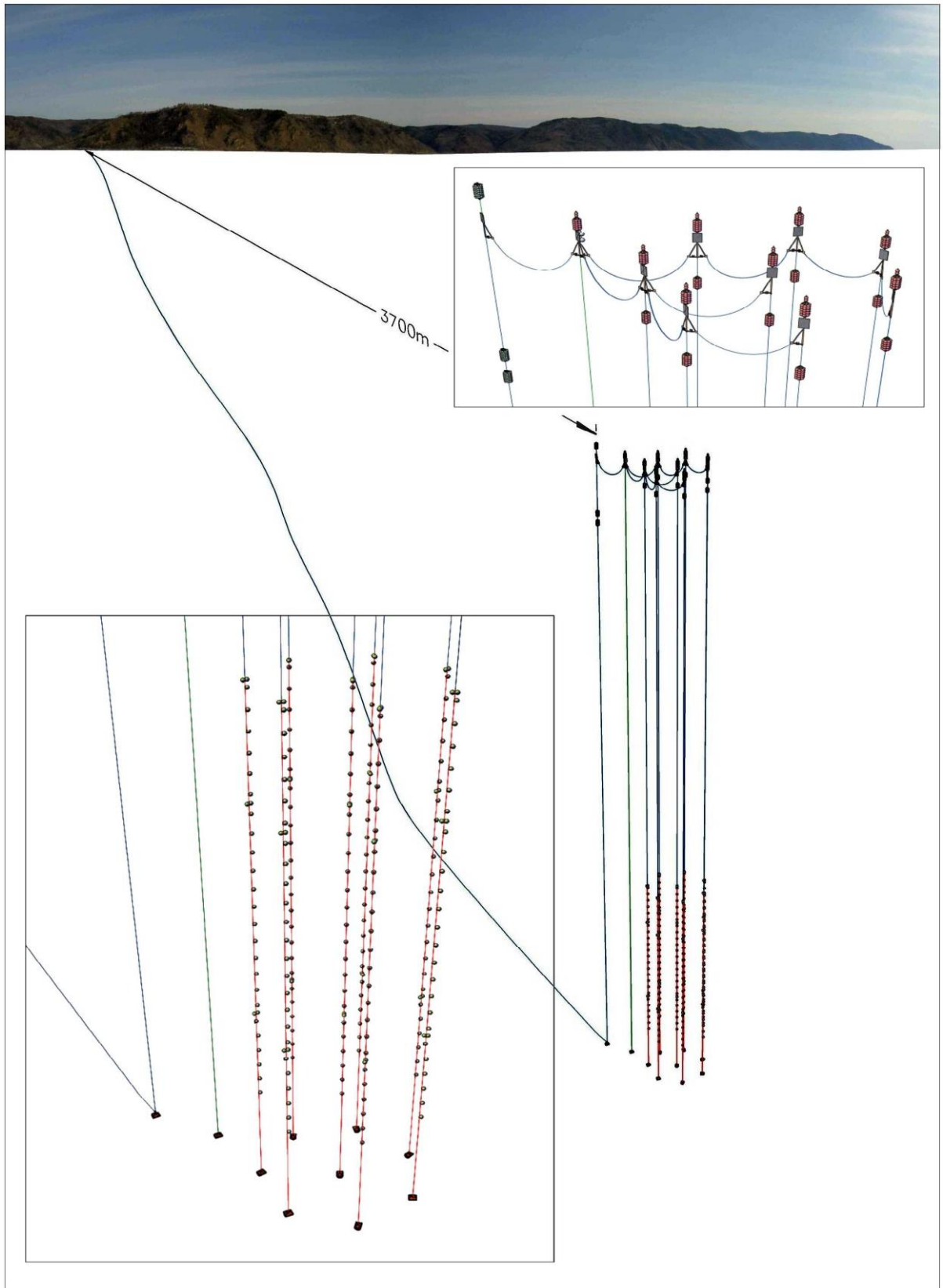


Fig. 7.3: Schematic view of the BAIKAL-GVD cluster.

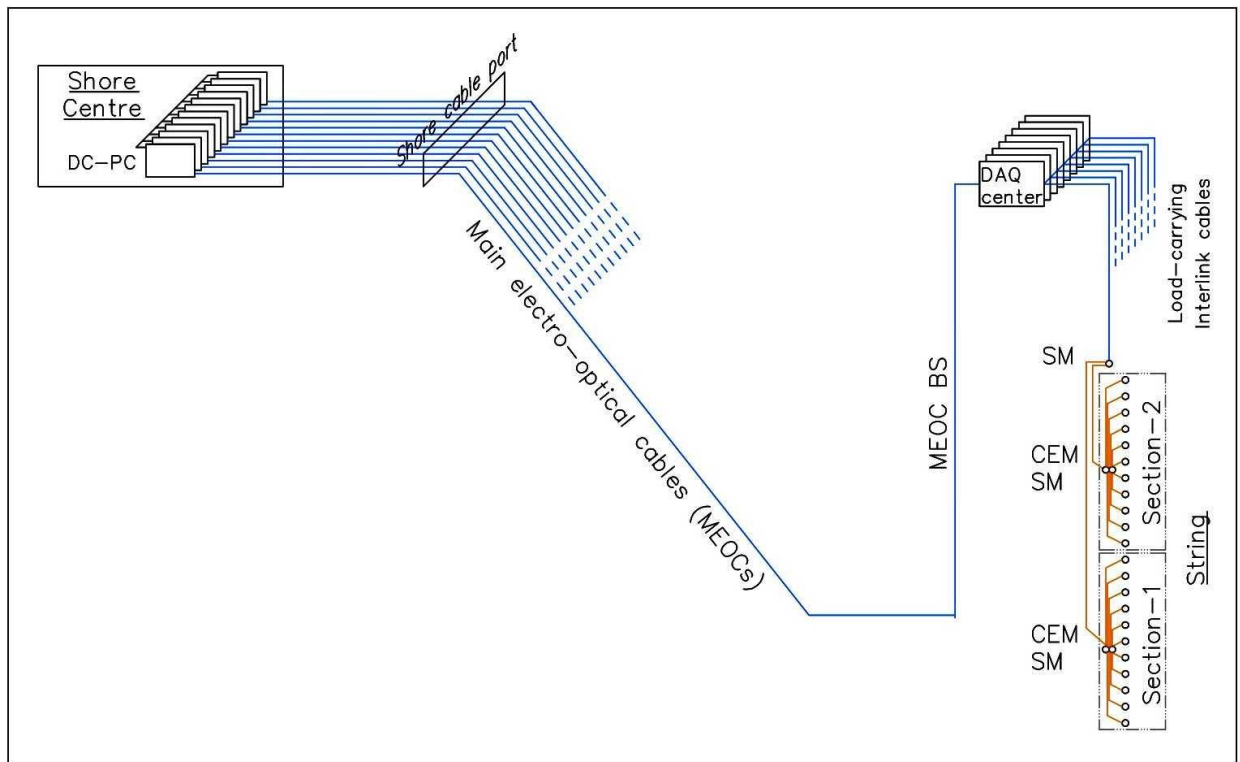


Fig. 7.4: Schematic view of the cable network.

7.2.1. Main elements of buoy stations

Ropes and underwater cables, including load-carrying ones

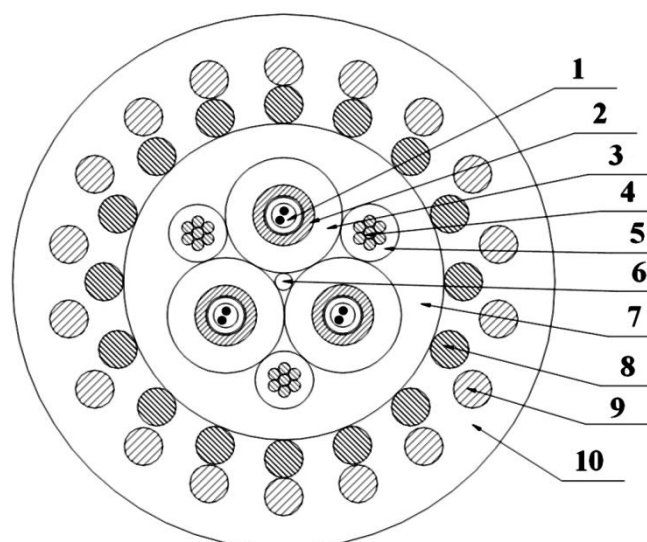
Cables of modern design are used in the BAIKAL-GVD telescope as a buoy lines. These cables, in contrast to cables with external armor, weigh much less and have an environment-protected sheath. These allow substantially increase the cable lifecycle and reduce the required buoyancy of buoy stations.

Sea parts of MEOCs are used as buoy lines of cable buoy stations. In the SBS stations, a stainless steel rope is used in the lower parts of the buoy lines on which modules with recording and service equipment are located. It is also used for grounding in the BAIKAL-GVD power supply. In the upper part of SBSs the interlink cables are used as buoy lines. Synthetic ropes and cords are used as upper parts of buoy lines on buoy stations. They are also applied as rigging and technological accessories when assembling.

Cable clamps and tips

A unified cable clamp with a working surface in the form of a hexagonal right prism was specially developed in 1986 for cable-rope buoy stations deployed in Lake Baikal. This clamp supports reliably load-carrying cables with a two-layer external armor and does not damage their conducting wires. Special stainless steel clamps are used for stainless steel ropes.

KG 3x0,75+3x(1,8+2OOb)-70-90 AJ



No№	Name of design elements	The material and dimensions of design elements	Diameter, mm
1.	The optical communication channel.	Two standard single-mode fiber in the shell, hydrophobic filler	1,2
2.	The shell of the fiber optic module - Conductor B.	Copper tube 1,3/2,0 (1,8mm ²)	2,0
3.	The isolation of the Conductor B.	Propylene copolymer 02015-302KM-004 white, Δ=0,9mm	3,8
4.	Current-conducting strand - Conductors A.	Copper, mm 7x0,38 (0,75 mm ²)	1,14
5.	The isolation of Conductor A.	Propylene copolymer 02015-302KM-004 white, Δ=0,38mm	1,9
6.	Filling element.	Steel Ø 0,8 mm	
7.	Cover.	Polyethylene HDPE 273-81K, Δ=1,05 mm	10,3
8.	A first armour layer.	Galvanized high-carbon steel wire, 16x1,25 mm	12,8
9.	A second armour layer.	Galvanized steel wire, 18x1,25 mm	15,3
10.	Outer jacket	Polyethylene HDPE 273-81K Δ=1,1mm	17,5

Electrical characteristics:

Electrical resistance of Conductor A, max 25.2 / km
 Electrical resistance of Conductor B (copper tube), no more 11.0 Ohm / km;
 Insulation resistance of not less 15000MOM * km;

Optical characteristics:

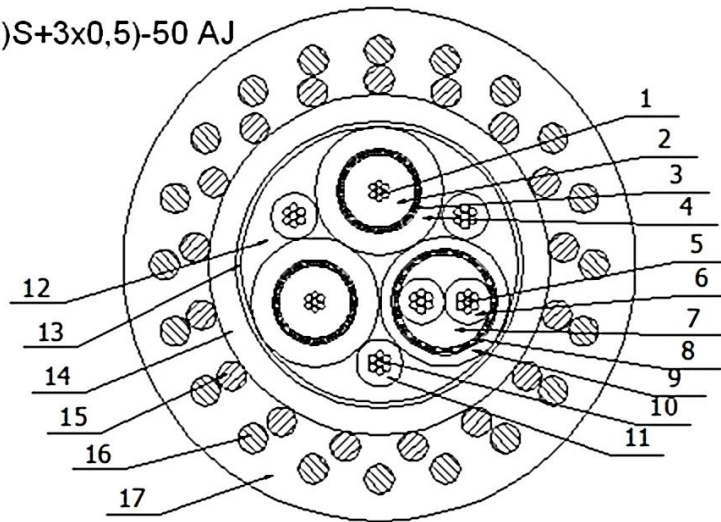
Diameter of optical fiber 9/125 micron
 Attenuation at a wavelength of 1.55 micron, max 0.7 dB / km

Mechanical characteristics:

Breaking strength of not less 70 kN
 Maximum working load of not more than 15 kN
 Maximum allowable hydrostatic pressure 15Mpa
 Cable weight in the air - not more 530 kg / km.
 Cable weight in water - not more than 290 kg / km.

Fig. 7.5: Main electro-optical cable.

KG (2Kx0,75 50+(2x0,5)S+3x0,5)-50 AJ



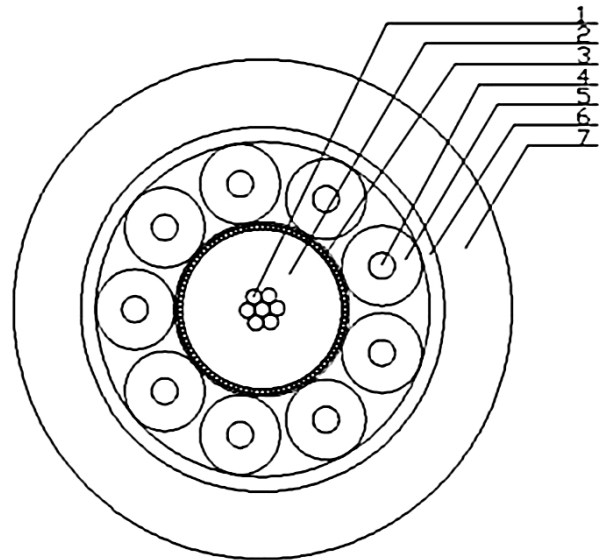
№	Structural elements	Material of structural elements, sizes	Diameter, mm
1.	Conductors A.	Soft copper, 7x0,25 (0,35 mm ²)	0,75
2.	Insulation	HDPE 271-70K Δ=0,97mm	2,7
3.	Coaxial screen	Soft copper, 0,1x6x13	3,0
4.	Insulation	HDPE 271-70K 0.8 mm	4,8
5.	Conductors B.	Soft copper, 7x0,30 (0,5 mm ²)	0,90
6.	Insulation	HDPE 271-70K Δ=0,42mm	1,75
7.	Filler	Sevilene	3,6
8.	Coaxial screen	Soft copper, 0,1x6x13	4,0
9.	Insulation	LDPE 107-61K Δ=0,45mm	4,8
10.	Conductors C.	Soft copper, 7x0,30 (0,5mm ²)	0,90
11.	Sealant	Polyisobutylene	1,75
12.	Winding	Non-woven material 3E6035	10,3
13.	First layer	Steel galvanized wire 17x1.1	10,8
14.	Inner jacket.	HDPE 271-70K Δ=0,6mm	12,0
15.	A first armour layer.	Galvanized high-carbon steel wire, 17x1,1 mm according to GOST 7372-79	14,2
16.	A second armour layer.	Galvanized steel wire, 20x1,1 mm	16,4
17.	Outer jacket.	HDPE 273-81K Δ=0,8mm	18,0

Main parameters:

Electrical resistance of Conductor A, not more	.57 Ohm / km;
Electrical resistance of Conductor B, not more	.40,5 Ohm / km;
Electrical resistance of Conductor C, not more	.40,5 Ohm / km;
Insulation resistance of not less	15000 MOhm*km;
Wave resistance of the coaxial pair	50±5 Ohm
Attenuation of the coaxial pair for the frequency of 5 MHz , not more	40 Db/km
Wave resistance of twisted pair	100±15 Ohm
Attenuation of the twisted pair for the frequency of 10 MHz , not more	50 Db/km
Working temperature	-50°C - + 60°C
Breaking strength, not less	50kN
Cable weight in the air	560 kg/km
Cable weight in water	305.5 kg/km

Fig. 7.6: Interlink cable.

KST (K50+9x0,15)



№	Structural elements	Material of structural elements, sizes	Diameter, mm
1	Current-conducting strand - Conductors A	Soft copper 7x0,3мм (0,5mm ²)	0,9
2	Insulation	HDPE 271-70K Δ =1,15 mm	3,2
3	Coaxial screen	Soft copper, 96x0,1mm ² , PET band	3,5
4	Current-conducting strand - Conductors B	Soft copper 1x0,45мм (0,15mm ²)	0,45
5	Изоляция проводника питания	Полиэтилен ПНД 271-70К, Δ =0,57 мм.	1,6
6	Filler	Longitudinal sealing, Water blocked band of Non-woven material	7,4
7	Jacket.	Thermoplastic polyurethane Elastollan-1180, Δ =1,3mm.	10,0

Main parameters:

Electrical resistance of Conductor A, no more	40,5 Ohm / km;
Electrical resistance of Conductor B, no more	129,6 Ohm / km;
Insulation resistance of not less	1000 MOhm*km;
Wave resistance of the coaxial pair	50±10 Ohm
Cable weight in the air	105 kg/km
Cable weight in water	27 kg/km

Fig. 7.7: OM-cable.

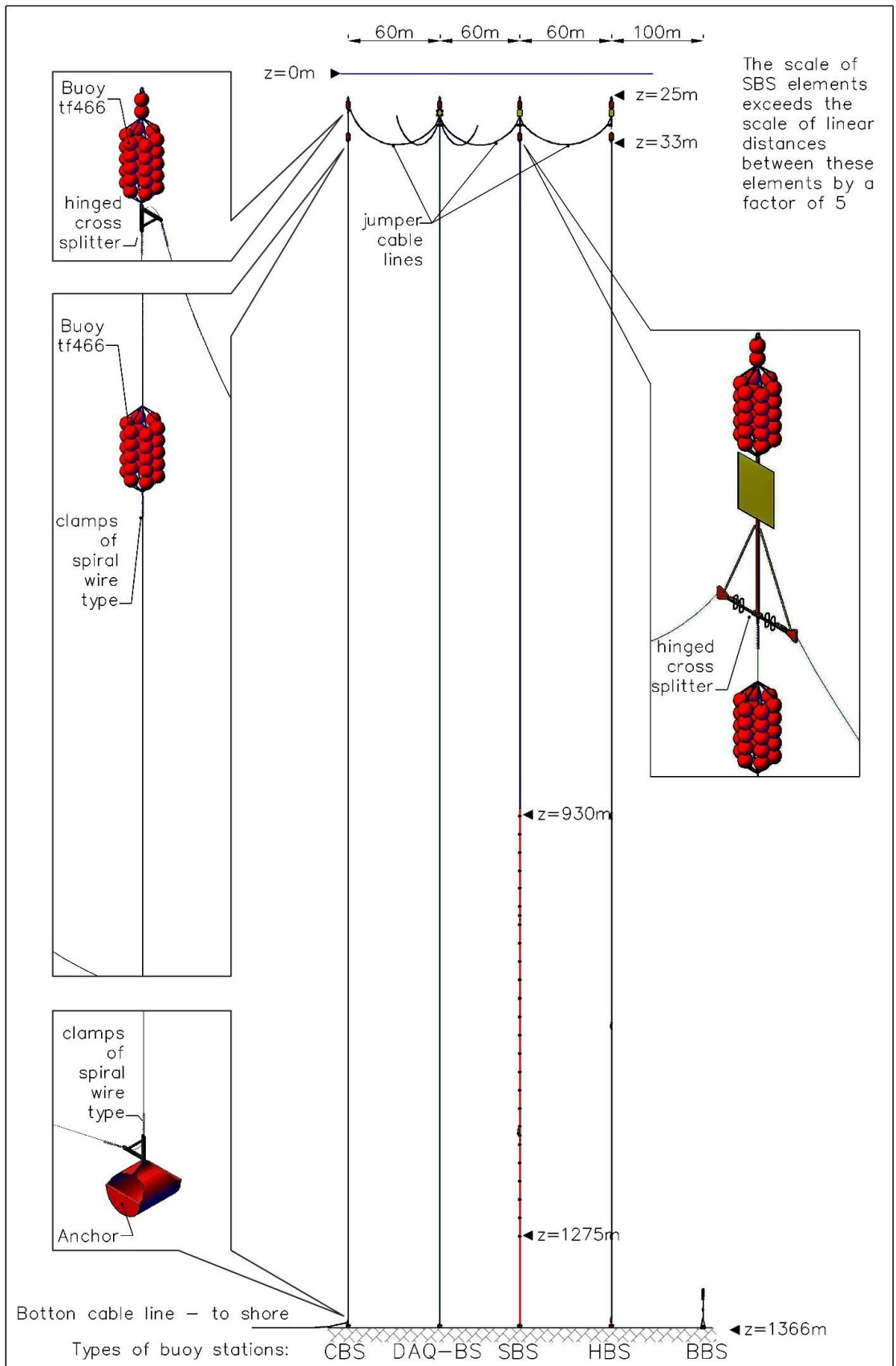


Fig. 7.8: Types of buoy stations.

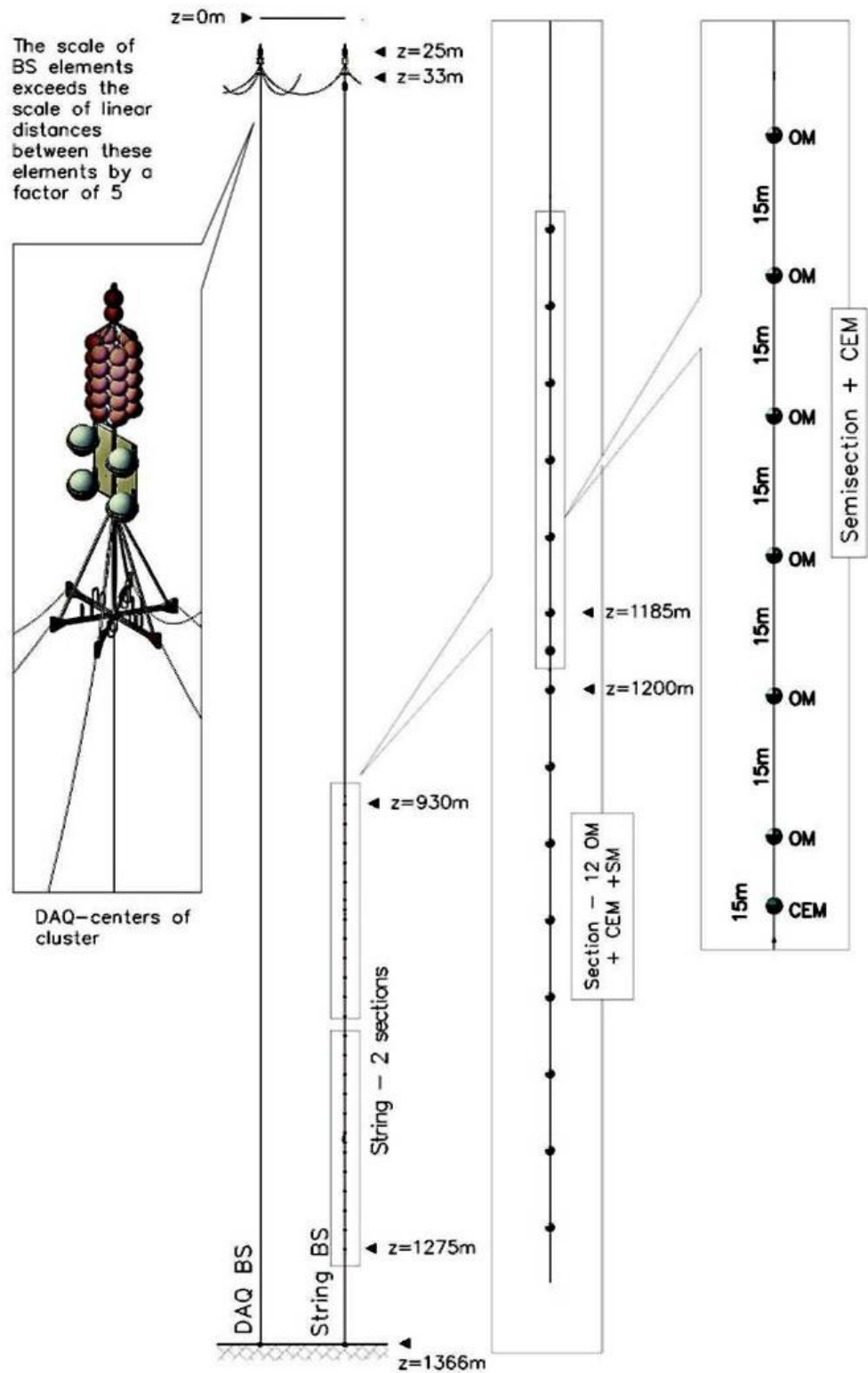


Fig. 7.9: String and DAQ buoy stations.

Dead-end supporting clamps of spiral type are used as load-bearing mounting elements on buoy lines and jumper cable lines composed of cables with a reinforced plastic sheath. These clamps are highly reliable and adjustable; they are characterized by a multiple safety factor and do not affect much the reinforced cable sheath.

Intermediate and top buoys of buoy stations

It is assumed to replace aluminum floats, which are currently used as buoyancies for the top (operating horizons up to 25 m) or intermediate buoys in the buoy stations of the BAIKAL-GVD, with plastic Trawl floats no.446 (ENGEL-NETZE GMBH & CO KG, Germany). These floats are much less expensive and more technologically efficient in assembly. They are proposed to be used in bunches on cords, up to ten pieces in each. The bunches are fixed to the upper ring of the cross splitter to form a top buoy or to the thimble of the spiral clamp under the cross splitter to form an intermediate buoy. Plastic floats have been successfully used as top buoys on the limnological and geophysical autonomous buoy stations in Lake Baikal since 2003.

7.3 Deployment of Carrier Structures

The main feature of the assembly works described here is the use of Lake Baikal ice cover. The unique properties of the Baikal ice and favorable meteorological and landscape conditions (practical absence of water currents and ice field drift) make it possible to perform assembly works for six to eight weeks (from February to the beginning of April) each year. Due to these factors and the application of specially developed mounting and cable-laying equipment, the telescope underwater mechanical structures of almost any required resizes and configurations can be deployed. The assembly accuracy can be as high as 20-50 cm at depths of 1300-1500 m, due to the low assembly rate and, correspondingly, low dynamic loads.

To date, a more than 30-year experience in deployment and maintenance of equipment in Lake Baikal has been accumulated. All necessary equipment, capable of operating reliably under the ice conditions of Lake Baikal, has been developed. It includes the winches with a high capacity (up to 4 km for 18-mm cables) and a hoisting capacity up to 3500 kg; a complex of ice-cutting and cable-laying machines; mobile rooms on sledges; mobile diesel generators up to 50 kW; a set of field power cables; cable conveyors; cargo sledges; etc. There are also cars and trucks for transporting people and loads and towing equipment fixed on sledges.

Deployment of buoy stations

A buoy station is deployed using a winch with a buoy line (previously marked out and trialed by the nominal load) on a reel. The buoy line is burden with the anchor. As the buoy line is reeled off, all elements of the station, including the measurement equipment with cable connections, are mounted on it. Throughout the entire deployment process the working capacity of the recording equipment and electronic systems is tested and the length and tension of buoy line cable is monitored. When submerging, a test touch of the bottom by the anchor is performed to ensure the location of the top buoy at the expected depth. Then the cross splitter is installed, the horizontal subsurface cable

jumpers are connected, the necessary equipment is assembled on the cross splitter and connected to the cables, and the top buoy is fixed. The station is suspended on the adjusting rope and is submerged until the anchor touches the bottom, after which the final tests of equipment are performed.

The buoy station is dismantled as follows. First, the lifting rope is fixed (through a latch hook) by diver at the ring on the top buoy, which is located at a depth of 25 m, and led to the winch. Then lifting is performed in a sequence reverse to the buoy station deployment procedure described earlier.

Deployment of bottom cable lines (MEOCs) and cable buoy stations

Bottom cable lines are deployed from the lake ice cover, using a complex of special cable-laying machinery, which has been developed and fabricated by the Nizhny Novgorod State Technical University. This complex comprises the following units:

- leveler, which serves to remove undulations and hummocks from the ice surface along the cable path;
- disk milling machine for digging trenches in ice;
- cable handler;
- cable winch with an autonomous electric power generator to drop or lift the cable.

The cable-laying complex moves along the cable path with the aid of a crawler transporter or a tractor. The cable buoy station (CBS) is used for delivering the sea end of the MEOC under the lake surface for following connection with the cluster DAQ-center. CBS comprises the part of bottom cable as its buoy line. For CBS deployment the cable loop with anchor in the middle is immersed in synchronously from two ice holes, which are located approximately in the range of the path laid and are spaced by about 300 m. The sea end of the loop is lowered using a winch, while the shore end is laid from the hoist of the cable-laying complex through the cable handler. In this way, one can position the anchor of a cable buoy station with an accuracy of few meters. When the anchor contacts the bottom at the expected point, the milling machine start to cut a slit in the ice cover, into which the cable layer drops the cable from the hoist. The hoist and the layer move synchronously through the slit after the milling machine at a distance of 100 m behind it. Under these conditions, cable put down to the slit and laid on the lake bed corresponding to the layering data-tables. The layering data-tables contain also the calculated values of cable inclination angles during submerging in the water from the cable-laying machine and the cable tension. These parameters are also controlled during deployment.

Near the shore, at a depth about of 5 m, the cable is fixed to the shore anchor (along with the 200 m long piece of cable), and the shore end of the cable is led to the shore through the cable port.

During laying, the sea end of the bottom cable line remains on the adjusting winch. After deploying more than 2000 m of the bottom cable, this winch winds up the cable and lifts the anchor of the cable buoy station at about of 150 m height. Then intermediate buoys and a cross splitter are mounted at the specified horizons on the buoy line of the cable station, and the top buoy is fixed. Finally, the station is installed on the lake bed and its exact coordinates are measured.

Mounting subsurface cable jumpers

The subsurface cable jumpers are used to connect neighboring buoy stations; they are fixed on cross splitters on these stations. The jumpers are mounted under ice using special equipment: "under-the-ice tractor", which has a positive buoyancy and moves under the ice either by operator's commands, or applying a special underwater torpedo (which is self-guided to an installed ultrasonic beacon).

Near-bottom beacon buoy stations

Near-bottom beacon buoy stations are used to install the near-bottom autonomous equipment (beacons - transponders of hydroacoustic positioning system) and have a short (30-50 m) buoy lines with a small buoy at the end. There is a special "collar" under the buoy; when the buoy station must be lifted, it can be hooked by this "collar" by means of a special dismantling device: a horizontal bar with hooks suspended.

7.4 Works in the Lake Ice Camp

The period of the assembly works on Lake Baikal is primarily determined by the condition of its ice cover. Generally, freezing-over on the southern Baikal begins at the end of January. Furthermore, the ice thickness increases at a rate of 3-5 cm per day and reaches 40 - 50 cm by the middle of February. Works with application of heavy machines can be carried out on an ice cover of this thickness.

The works on ice begin with deployment of the ice camp. First, the main reference point (landmark) of the ice camp is set with accuracy of about 50 cm, using a theodolite and locating the position with respect to three shore reference points with known coordinates. Then, based on the set of reference points, the locations of all underwater buoy stations are marked out by means of a theodolite and a geodimeter.

An ice camp is organized to carry out the expedition works. The camp keeps trailers and lodges (assembly, laboratory, storage, and household modules), winches, electric power generators, and a cable power supply and communication network. The works in the ice camp last generally from 6 to 8 weeks. The end of the expedition is determined by the ice condition and corresponds to the beginning of April (generally, from April 5 to April 10). The ice camp's gradual evacuation begins either at the end of March or at the beginning of April.

8 EXPECTED BAIKAL-GVD PERFORMANCE

8.1 High-Energy Muons

8.1.1 Cherenkov radiation of muons

A quantitative theory of the Vavilov-Cherenkov effect within classical electrodynamics was developed in 1937 by I.E. Tamm and I.M. Frank [64]. Charged particles moving faster than light in a medium with index of refraction $n(\lambda)$, i.e. $v > c/n$, emit Cherenkov radiation per path length and per photon wavelength λ with intensity of

$$\frac{d^2 n_\gamma}{d\lambda dx} = 2\pi\alpha \left(1 - \frac{1}{\beta^2 n^2}\right) \frac{1}{\lambda^2}, \quad (8.1.1)$$

where α - the fine-structure constant and $\beta=v/c$ is the particle velocity in units of the velocity of light in a vacuum. A remarkable feature of the Cherenkov radiation is that the photons are emitted at an essentially fixed angle θ_c

$$\cos \theta_c = \frac{1}{\beta \cdot n}.$$

The speed of Cherenkov photons v_c is equal to the group velocity of light of the corresponding wavelength in the medium:

$$v_c = \frac{c}{n_g(\lambda)}, \quad n_g(\lambda) = n(\lambda) - \lambda \frac{dn}{d\lambda}. \quad (8.1.2)$$

The photon wavelength interval 350-600 nm is the operating range of the Baikal neutrino telescope's photo-sensors. The lower edge is determined by glass transmission of the pressure housing of optical modules, while the upper edge is determined by the increase in absorption coefficient in water, the decrease in Cherenkov radiation intensity, and the decrease in photo-sensor quantum sensitivity with increasing wavelength in the red spectral region. The spectral dependence of the reciprocal velocity $1/v_c(\lambda)$ of Cherenkov photons in the Baikal water [65] is shown in Fig. 8.1.1 (left panel). The velocity $v_c(\lambda)$ is seen to grow with photon wavelength. The delay time dependence on path length of the 350 nm photons relative to 600 nm ones in the Baikal water is shown in Fig. 8.1.1 (right panel). The spectral dependence of the velocity of Cherenkov radiation in water causes the light signal from muons to be dispersed with time.

The muon energy range accessible for investigation with neutrino telescopes extends from tens of GeV to ultra-high energies. The light flux emitted when a muon passes in a medium includes the Cherenkov radiation initiated by the muon electric charge, the Cherenkov radiation of the δ -electrons produced when the medium's atoms are ionized by the muon, and the Cherenkov radiation of the showers resulting from e^+e^- pair production or the bremsstrahlung and photonuclear muon-medium interactions. The Cherenkov radiation of δ -electrons with energy $E_\delta < 20$ MeV is quasi-continuous along the muon trajectory with an intensity that is approximately 8% of muon one. The angular

distribution of these photons extends in the entire range of angles relative to the muon trajectory and has a maximum in the direction of muon motion.

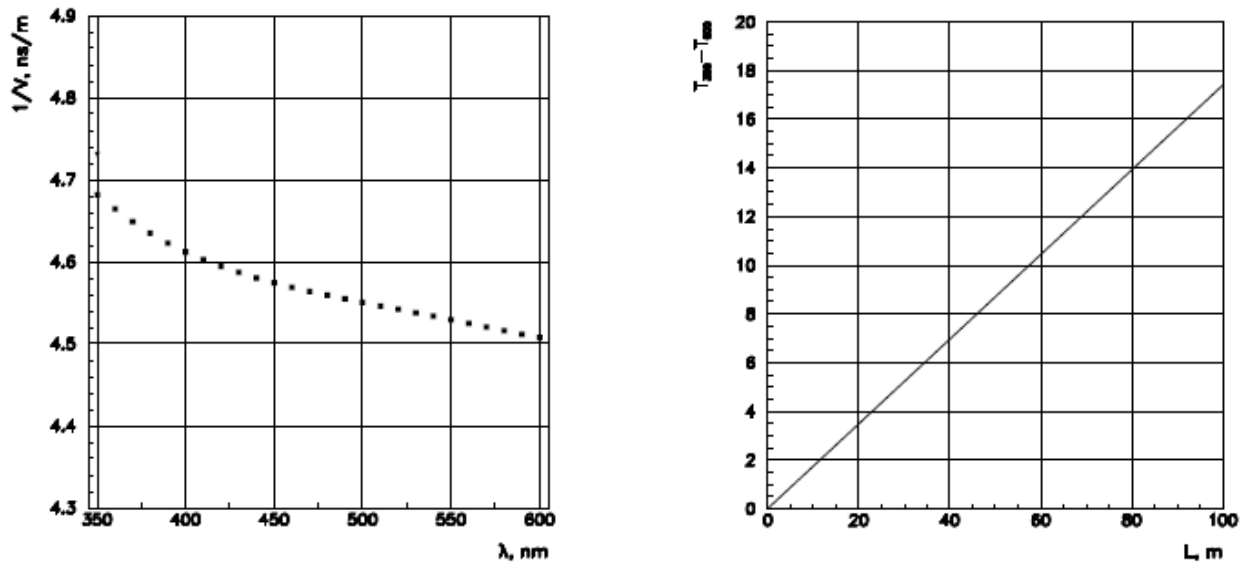


Fig. 8.1.1: Left panel - the spectral dependence of the reciprocal velocity of light in the Baikal water. Right panel - the difference between the arrival times of the photons with wavelengths of 350 and 600 nm in the Baikal water versus the path length.

Thus, the light field initiated by a muon in a medium can be separated into two components. First component is emitted continuously with a constant linear density as the muon moves along its trajectory. The linear density and angular distribution of the photons from this source are determined by the Cherenkov photons from the muon and δ -electrons. Second component is formed by local (roughly point-like) sources on the muon trajectory and describes the Cherenkov radiation of the showers resulting from e^+e^- pair production as well as from the bremsstrahlung and photonuclear muon-medium interactions.

8.1.2 Muon events simulation

The selection of events from neutrino induced upward going muons, suggests a fairly reliable estimation of the expected background from atmospheric muons. The procedure for simulating events from atmospheric neutrinos and background events from atmospheric muons in an array can be arbitrarily divided into the following steps:

- of the atmospheric muon flux at sea level;
- simulation of neutrino interactions in water or rock and production of secondary muons;
- muon propagation to the array level;
- simulation of the array response to the Cherenkov radiation of muons by taking into account the features of array measuring systems.

The CORSIKA5.7 code [66] was used to simulate the flux of atmospheric muons at sea level (the hadronic interaction was simulated using the QGSJET model [67], the chemical composition of the primary cosmic rays corresponded to that proposed in [68]).

The intensity of the muon flux at sea level with energies above 300 GeV (the threshold energy for a muon to pass about 1 km in water) obtained in the simulation turned out to be a factor of 1.6 lower than the intensity expected from the fitting of the existing experimental data [69, 70]. The cause of this discrepancy has not been established at present. Therefore, when comparing the experimental and expected event count rates in the array, we increase the latter by a factor of 1.6, i.e., in fact, normalize it to the muon flux at sea level measured in other experiments.

When simulating the muon flux from atmospheric neutrinos, we used the neutrino spectrum from [71] as the primary one. Since the detection threshold energy of the muons from neutrinos satisfying the trigger conditions that provide unambiguous reconstruction of the muon track parameters is ~ 10 GeV, the processes of neutrino-matter interaction via the channels of quasi-elastic scattering and one-pion production may be neglected. The cross sections for deep inelastic neutrino-matter interaction were calculated using the CTEQ4M parton distribution function [72]. The muon propagation through water and rock was simulated with the MUM (MUons + Medium) code [73]. Comparison of the derived muon flux at the array level with other (including analytical) calculations based on various models of the atmospheric neutrino spectrum (see, e.g., [74]) and interaction models revealed $\pm 10\%$ difference in absolute value of the muon flux from neutrinos and a less than 4% deviation in spectrum shape. Both these discrepancies are attributable mainly to a difference in the atmospheric neutrino spectra used.

When taking into account the oscillations of the muon neutrinos as they propagated from the point of production in the atmosphere to the point of interaction in rock or water, we used the muon neutrino survival probability based on two-neutrino oscillation model by assuming the mass states to be completely mixed:

$$P_{\nu_\mu \rightarrow \nu_\mu} = 1 - \sin^2 \left(1.27 \cdot 10^{-6} \frac{\Delta m^2}{10^{-3} \text{eV}^2} \frac{L}{1 \text{km}} \frac{1 \text{TeV}}{E_\nu} \right),$$

where $\Delta m^2 = 2.5 \cdot 10^{-3} \text{eV}^2$ and L is the distance from the point of neutrino generation to the point of observation. In this case, the point of neutrino production was chosen at an altitude of 15 km from the Earth's surface.

We simulated the propagation of the Cherenkov radiation from muons in water and the OM response to this radiation using the codes specially developed for these purposes [75]. As a muon propagates in water, the energy losses through the production of δ -electrons with energies below 20 MeV are considered as continuous and the light field from these δ -electrons is added to the muon light field. The production of δ -electrons with energies above 20 MeV, the production of e^+e^- pairs and bremsstrahlung γ -ray photons, and the photonuclear interaction events are simulated along the muon track in accordance with the cross sections for these processes. The light field from cascades of various energies is simulated by dividing the cascade curve into 1-m-long segments. The wavelength dependence of the absorption coefficient is taken into account in the simulation. Since the light scattering in the Baikal water affects weakly the delay time and amplitude of the light signal when recording the photons from distances of less than 50 m, the scattering in the muon code is disregarded. When solving the problems in which the contribution of the Cherenkov radiation from great distances is important (calculating the array response to high-energy showers and magnetic monopoles), the light scattering in water is taken into account using the technique described in [76]. The

average number of photoelectrons produced at the photo-sensor photocathodes is calculated by taking into account the individual sensitivity of a given OM and its orientation relative to the photon arrival direction. The exact number of emitted photoelectrons is calculated from the Poisson distribution with allowance made for their average number derived previously. The photo-sensor trigger time was determined by taking into account the photo-sensor time jitter.

8.1.3 Atmospheric muons

Atmospheric muons primarily form a natural background when the neutrino fluxes are recorded. At the same time, they can be used as a calibration source of various types of events. To calculate the expected count rate of events from atmospheric muons, we used a sample of pregenerated events from primary cosmic rays the muons from which have an energy higher than is needed to reach the detector level for a given zenith angle.

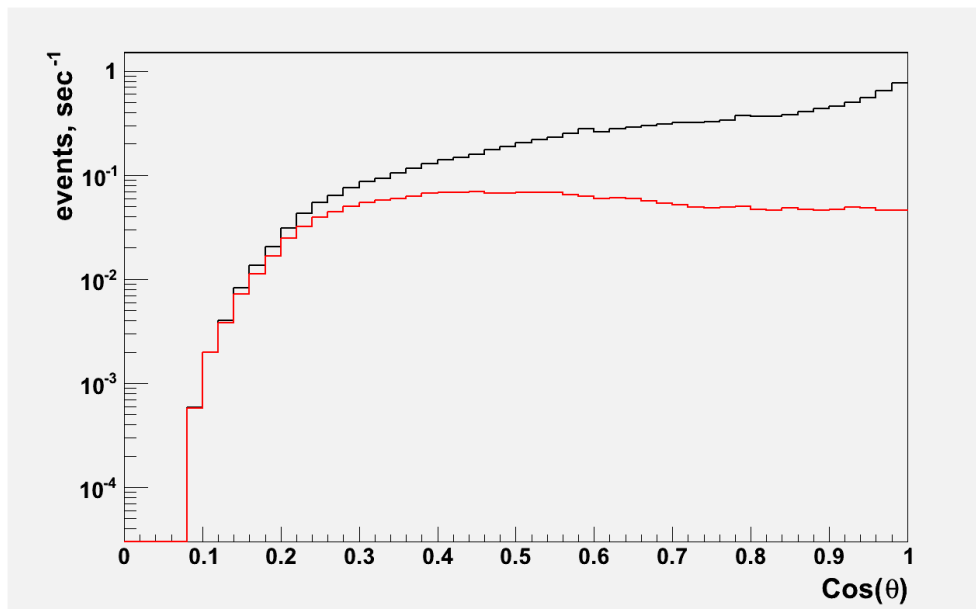


Fig. 8.1.2: The angular distribution of events from atmospheric muons. The upper histogram - all events. The lower histogram - the events from single muons.

The expected count rate of events from atmospheric muons satisfying the cluster trigger condition (the triggering of two neighboring photo-sensors within a time windows of 100 ns with the corresponding amplitude thresholds (see Section 4.5.2)) is 170 Hz for the entire array (2304 OMs). For the trigger allowing the muon track reconstruction (the triggering of 6 or more OMs on 3 or more strings - the 6/3 trigger), the expected count rate is 10.5 Hz. The angular distribution of events for the 6/3 trigger is presented in Fig. 8.1.2 (upper curve). In the case of an array with a low density of the spatial distribution of photo-sensors, which is true for BAIKAL-GVD, the probability of detecting the events induced by muon bundles can exceed considerably the probability of detecting single muons. For BAIKAL-GVD configuration with 2304 OMs, the expected count rate of events from single muons is approximately 2.2 events per second, which accounts for about 20% of the total number of expected events for the 6/3 trigger. However, this is sufficient for the calibration of the telescope's sensitivity based on atmospheric muons.

The angular distribution of events from single muons is presented in Fig. 8.1.2 (lower curve). As can be seen from this figure, the fraction of the events from single muons increases from the zenith to the horizon. For example, at zenith angles $\cos(\theta) < 0.4$, the contribution of the events from single muons becomes dominant.

Information about the expected count rate of the shower events initiated by atmospheric muons is needed to test the algorithms for selecting and reconstructing high-energy showers. The count rate of such events with a shower energy > 10 TeV and the number of hit photo-sensors > 10 is about of $4 \cdot 10^{-3}$ events per second.

8.1.4 Atmospheric neutrinos

To simulate the array response to muons induced by the atmospheric neutrinos, we used the models described in Section 8.1.1. The expected count rate of muons from atmospheric neutrinos from the lower hemisphere with energies $> E_\nu$ (black curve) and $< E_\nu$ (red curve) are presented in Fig. 8.1.3 for the 6/3 trigger condition (for 2304 OMs array). The expected number of events from atmospheric muon neutrinos is approximately 4300 events per year. A more detailed distribution of the expected event count rate at low neutrino energies is shown in Fig. 8.1.4 (left panel). As can be seen from this figure, the threshold energy range for atmospheric neutrinos detection is about 30-80 GeV. Because of the relatively high threshold, the oscillation effect reduces the total number of expected events per year by ~ 100 events. 90% of expected events are produced by neutrinos from 90 GeV-14 TeV energy range.

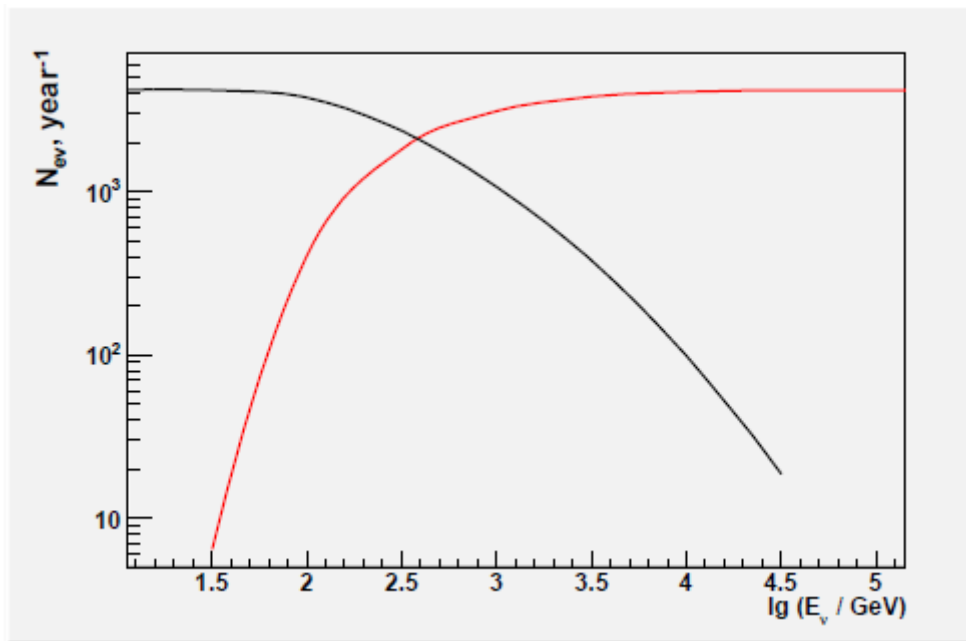


Fig. 8.1.3: The expected count rate of muons from atmospheric neutrinos from the lower hemisphere with energies $> E_\nu$ (black curve) and $< E_\nu$ (red curve).

The zenith angle distribution of events from the lower hemisphere is presented in Fig. 8.1.4 (right panel). The difference in count rate depending on the zenith angle is attributable to array configuration peculiarities (see Section 5.2.2): the geometrical area is

about 0.8 km^2 for muon trajectories close to the direction to the nadir and approximately 0.35 km^2 for horizontal muons. An additional factor that increases the effective area near the direction to the nadir is the downward orientation of the telescope's OMs.

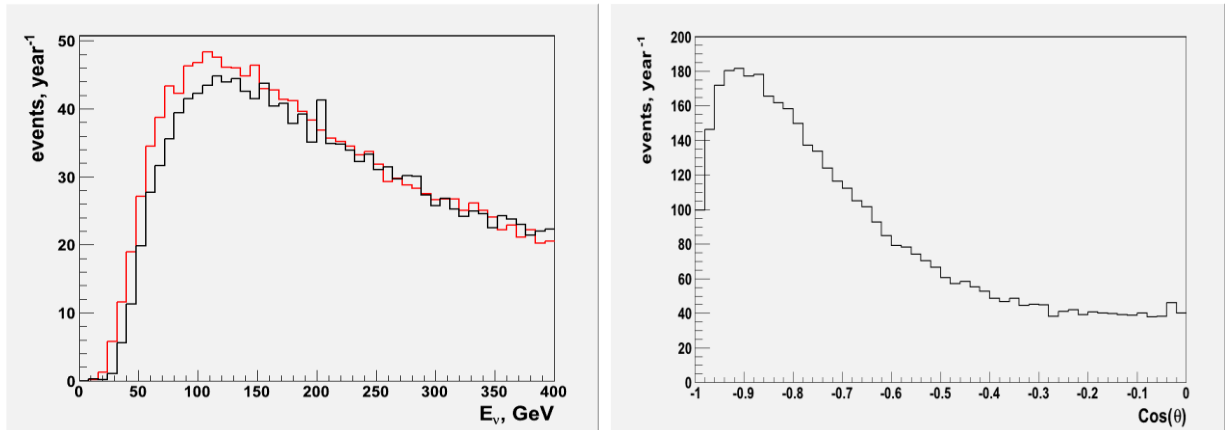


Fig. 8.1.4: Left panel – neutrino energy distribution in the low energy range (the red curve - without oscillations; the black curve - with oscillations). Right panel - the zenith angle distribution of events from upward going atmospheric neutrinos.

The sharp decrease in count rate at an angle of 180° is attributable to the 6/3 trigger condition, i.e., the requirement that at least 3 strings of the telescope are triggered. Since the minimum separation between the strings is about 60 m and since the muons have mostly low energies, the probability of detecting such events is low. It should be noted that the zenith angle of nearly vertical muon trajectories from below can be reconstructed by taking into account the amplitude and time information from the OMs of one string, which leads to an increase in the effective muon detection area.

8.1.5 The PMT noise and water background rejection

Analysis of the data collected with the prototype strings operated during 2008-2010 shows that the count rates of individual OMs are about 20 kHz. The photo-sensors are mainly triggered either from PMT intrinsic noise (PMT dark current) or from water luminescence caused by various factors. The photo-sensors triggered from noise pulses may distort significantly the telescope's time response and, accordingly, will affect the muon track reconstruction accuracy. Therefore, before reconstructing the muon track, it is necessary to identify and exclude the photo-sensors triggered from noise pulses.

To develop the *rejection* procedure that allows the noise-triggered photo-sensors to be identified and excluded from the subsequent analysis, we simulated the telescope's response taking into account the noise pulses. In our simulation, the noise of the PMTs has been assumed to be 20 kHz. The amplitude distribution of noise pulses was obtained by analyzing the data from the prototype strings (see Fig. 8.1.5). From the sample of generated events induced by muons with different fixed energies, we selected those that satisfied the 6/3 trigger condition (6 or more hit photo-sensors on 3 or more strings).

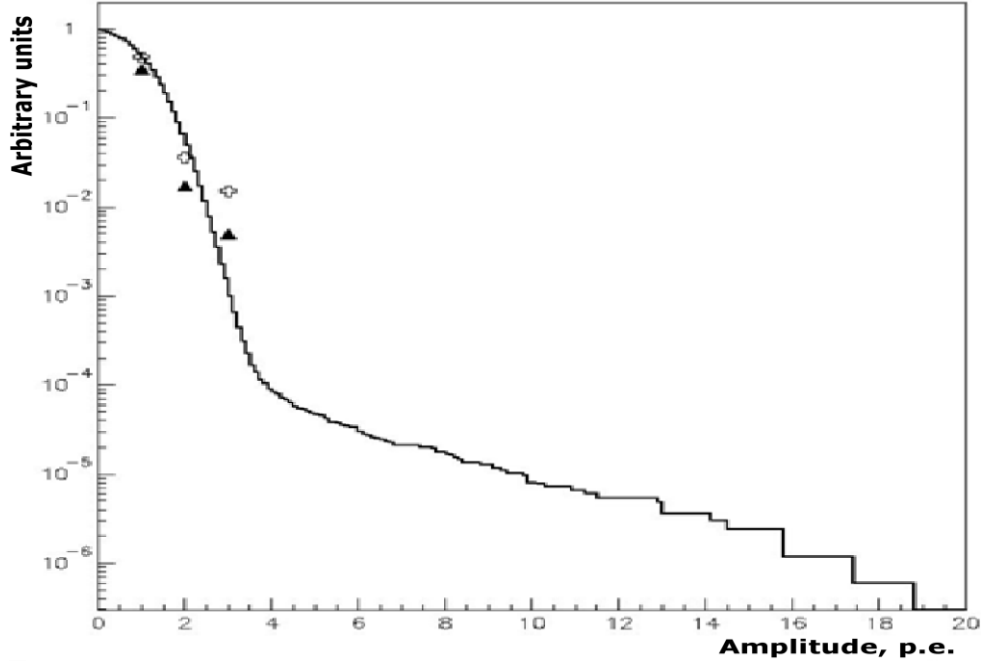


Fig. 8.1.5: The amplitude distribution of noise pulses.

It was shown that for 10 TeV muons, the average number of photo-sensors hit by Cherenkov photons is 10.8, while the average number of photo-sensors triggered from noise pulses is 19.4. The hit multiplicity distributions induced by Cherenkov photons and noise are shown in Fig. 8.1.6.

The developed *rejection* procedure assumes the fulfillment of the following conditions: the difference between the hit times of any pair of photo-sensors should be smaller than the propagation time of the light between these photo-sensors (the *causality criterion*), i.e., the following relation must hold:

$$|\Delta t_{ij}| < r_{ij}/v_g + \delta,$$

where Δt_{ij} is the difference between the trigger times of the i th and j th photo-sensors, r_{ij} is the distance between the photo-sensors, v_g is the light group velocity, and δ is a constant equal to 5 ns that is introduced to compensate for the photo-sensor time jitter. The pairs violating the causality criterion are identified by a pairwise examination of all the triggered photo-sensors. In the next step, the photo-sensor containing the maximum number of pairs violating the causality criterion and having an amplitude of less than 3 photoelectrons is excluded. The photo-sensor exclusion procedure is repeated until all pairs of the remaining photo-sensors will satisfy the causality criterion.

Once the photo-sensor rejection procedure has been applied, the average number of photo-sensors triggered from noise pulses was 2.7, while the average number of photo-sensors triggered from Cherenkov photons was 10.7. The hit multiplicities after the application of the rejection procedure are shown in Fig. 8.1.7.

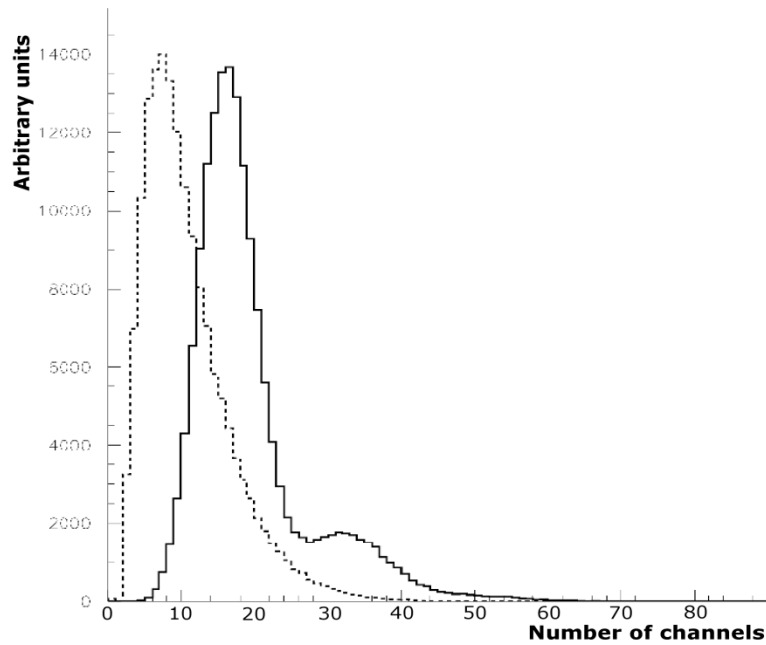


Fig. 8.1.6: The hit multiplicity distributions of events from 10 TeV muons. Solid line - the noise pulses; dotted line - Cherenkov photons.

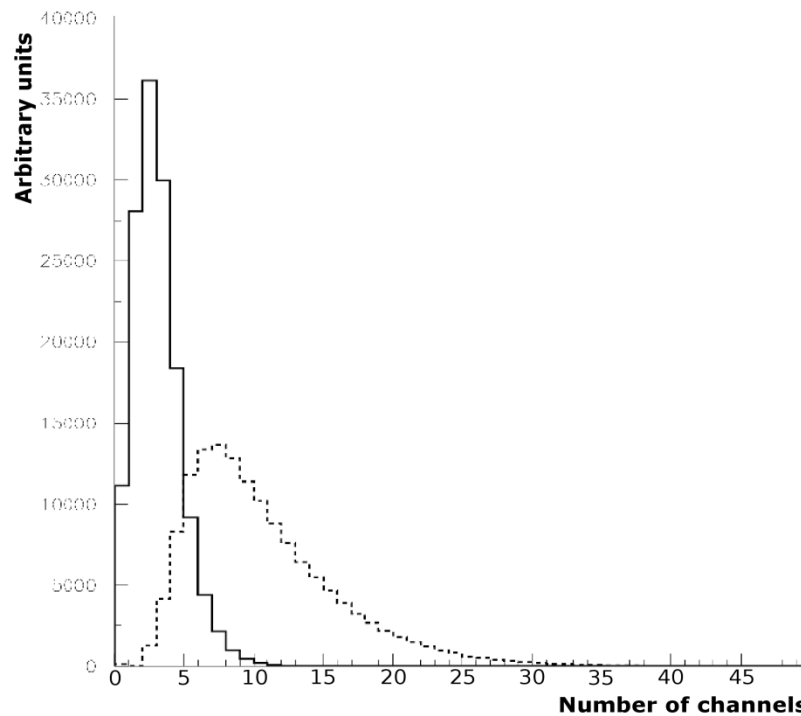


Fig. 8.1.7: The hit multiplicity distributions after the application of the rejection procedure. The solid histogram - the photo-sensors triggered by noise pulses. The dotted histogram - the photo-sensors triggered by Cherenkov photons.

As a result of described rejection procedure application, some fraction of the photo-sensors hit by the Cherenkov photons of secondary showers generated by muons is also eliminated from the subsequent analysis. The average number of such photo-sensors is 0.4, 0.98, and 3 for muon energies of 1, 10, and 100 TeV, respectively. Table 8.1.1

presents the average number of photo-sensors triggered from noise pulses, N_{noise} , and from Cherenkov photons, N_{cher} , before and after the rejection procedure for muons with energies of 1, 10, and 100 TeV. It can be seen from the table that the fraction of the photo-sensors triggered from the background for low-energy muons is more than 50% of their total number. This inevitably leads to a reduction in the reconstruction accuracy of the muon track parameters. Therefore, for the next stage of suppressing the influence of noise pulses, we use information about the deviation of the photo-sensor trigger time from that expected in the model of a plane propagation front of Cherenkov radiation from muons. The latter is used as the zeroth approximation in the muon track reconstruction procedure.

Table 8.1.1. The average number of photo-sensors triggered by noise and Cherenkov photons.

Energy	Before rejection		After rejection	
	N_{noise}	N_{cher}	N_{noise}	N_{cher}
1 TeV	16.8	2.9	4.02	3.0
10 TeV	19.4	10.8	2.7	10.7
100 TeV	21.2	26.8	3.2	24.6

The noise trigger suppression procedure is performed as follows: after the event reconstruction in the model of a plane front, the deviation of the time of each triggered photo-sensor from the theoretically expected one is checked. If this deviation for the photo-sensor exceeds 100 ns in absolute value, the trigger amplitude < 3 p.e., and the photo-sensor has no triggered neighbor on the string, then this photo-sensor is excluded from subsequent analysis. The results of this procedure are presented in Table 8.1.2 for muons from atmospheric neutrinos and muons with a fixed energy. As can be seen from this table, the relative contribution from the noise triggers decreases, which entails an increase in the muon reconstruction accuracy.

Table 8.1.2. The average number of photo-sensors after the application of the noise hit rejection procedures.

Energy	N_{cher}	N_{noise}
Atm.	6.9	1.9
1 TeV	5.8	1.7
10 TeV	11.5	0.9
100 TeV	25.4	1.0

8.1.6 Reconstruction

The muon track reconstruction algorithm which was used earlier for the NT200 data analysis is based on the assumption that the Cherenkov photons are emitted exactly at the Cherenkov angle - the so-called *bare* muon model. This model is efficient in reconstructing single muons with energies below several TeV. As the muon energy increases, using the *bare* muon model leads to a reduction in the reconstruction accuracy, because additional accompanying particles are produced in the muon-water electromagnetic interaction processes, causing the light flux from the muon to increase. The light arrival time distribution at the photo-sensor will change with increasing muon energy from a delta function (for the *bare* muon model) to a quasi-exponential one. To develop the algorithm for reconstructing the tracks of high-energy muons with the BAIKAL-GVD data, we calculated the temporal distributions of photons (with respect to arrival time of “direct” photons) from muons of various energies for different photo-sensor orientations and distances with respect to the muon. It was shown that the shape of the temporal distributions to be independent on the photo-sensor orientation with respect to the muon in the range up to 100-150 ns, where the behavior of the distributions are particularly important. These distributions were then fitted by the following expression

$$F(t, a, b) = t^a \exp(bt) / (|b|^{(-1+|a|)} \Gamma(1 - |a|)),$$

where t is the time in ns, a and b are parameters dependent on the muon energy and the distance from the OM to the muon track. However, the derived analytical expression does not include the PMT time jitter, which can be described by a Gaussian distribution with a characteristic deviation $\sigma \sim 2-5$ ns. The time distribution function including the photo-sensor jitter is the convolution of $F(t, a, b)$ and $N(t, 0, \sigma)$. As a result, the expression for the time distribution takes the form

$$\begin{aligned} FL(t, a, b, s) = & \frac{1}{\sqrt{\pi}s\Gamma(1 - |a|)} 2^{-1+\frac{a}{2}} e^{-\frac{t^2}{2s^2}} \left(\frac{1}{s^2}\right)^{\frac{1}{2}(-1-a)} |b|^{1-|a|} \\ & \times \left(\Gamma\left[\frac{1+a}{2}\right] H1F1\left[\frac{1+a}{2}, \frac{1}{2}, \frac{(bs^2+t)^2}{2s^2}\right] \right. \\ & \left. + \sqrt{\frac{2}{s^2}} (bs^2+t) \Gamma\left[1+\frac{a}{2}\right] H1F1\left[\frac{2+a}{2}, \frac{3}{2}, \frac{(bs^2+t)^2}{2s^2}\right] \right), \end{aligned}$$

where *H1F1* is the hypergeometric function 1F1 and $s=\sigma$. The derived time distributions are used for developing the photo-sensor temporal hit probability functions. Subsequently, these hit probability functions are used to construct the likelihood function for all of the triggered photo-sensors. The behavior of the temporal hit probability functions for the photo-sensor located at a distance of 10 m from the muon for various muon energies are presented in Fig. 8.1.8.

The muon track parameters are reconstructed by maximizing a likelihood function of the form

$$L(\rho, \theta, \varphi, E_\mu, t) = \prod_{hit} P_{time}(\rho, \theta, \varphi, E_\mu, t) \times \prod_{hit} P_{phit}(\rho, \theta, \varphi, E_\mu, t) \times \prod_{non} P_{pnon}(\rho, \theta, \varphi, E_\mu, t),$$

where $P_{time}(\rho, \theta, \varphi, E_\mu, t)$ is the temporal hit probability function for the triggered photo-sensor, $P_{phit}(\rho, \theta, \varphi, E_\mu, t)$ is the total hit probability for the triggered photo-sensor, and $P_{pnon}(\rho, \theta, \varphi, E_\mu, t)$ is the probability for the non-hit photo-sensor to be not exposed to Cherenkov radiation. The amplitude information is not used deliberately in the likelihood functions, because the fluctuating pattern of the bremsstrahlung and photonuclear processes accompanying the muon propagation in a medium introduces additional distortions into the model.

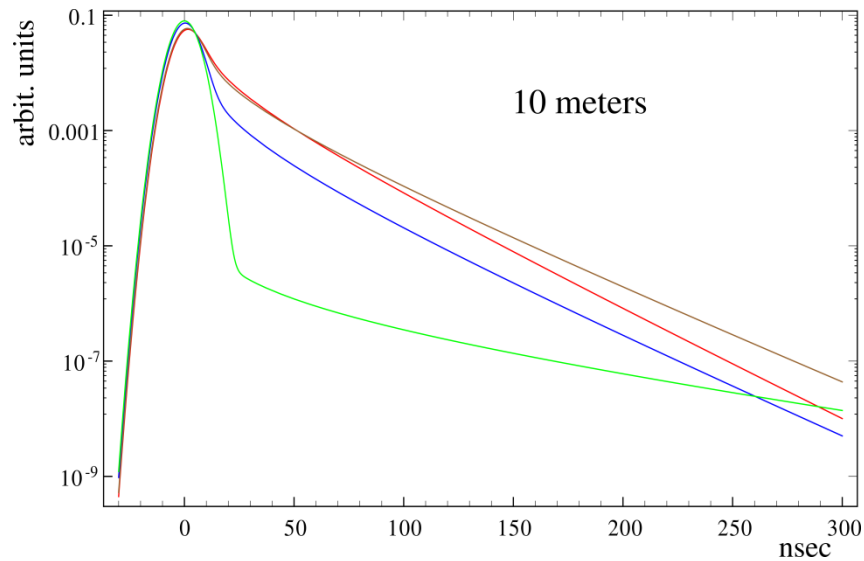


Fig. 8.1.8: The temporal hit probability functions for photo-sensor located at a distance of 10 m from the muon track. The green, blue, magenta, and red curves are for muon energies of 1000, 100, 10, and 1 TeV, respectively.

Since the reconstruction algorithm is under development, here we present only preliminary results on estimating the angular reconstruction accuracy and, as an accompanying result, our estimates of the muon energy reconstruction accuracy obtained by the technique described above.

Figure 8.1.9 shows the fraction of events with reconstruction mismatch angle less than a given value ψ for 10 TeV muons. The muon track reconstruction accuracy weakly depends on a muon energy, hence for energy range from hundreds of GeV to hundreds of TeV the reconstruction accuracy (median value of mismatch angle distribution) is about 0.3° . This result was obtained without any constraints on the muon track reconstruction quality parameters, as was done when processing the NT200 data.

As has been noted above, the likelihood function used to reconstruct the track parameters contains the muon energy as a parameter. Figure 8.1.10 presents the reconstructed energy of simulated 10 TeV muons. Although this algorithm was not optimized for the muon energy reconstruction, the derived distribution is not shifted with respect to the simulated muon energy with a resolution of 0.4 in logarithm. Thus, the described reconstruction procedure allows one to estimate the muon energy at a

satisfactory level and to obtain the zeroth approximation for the specialized energy reconstruction algorithm.

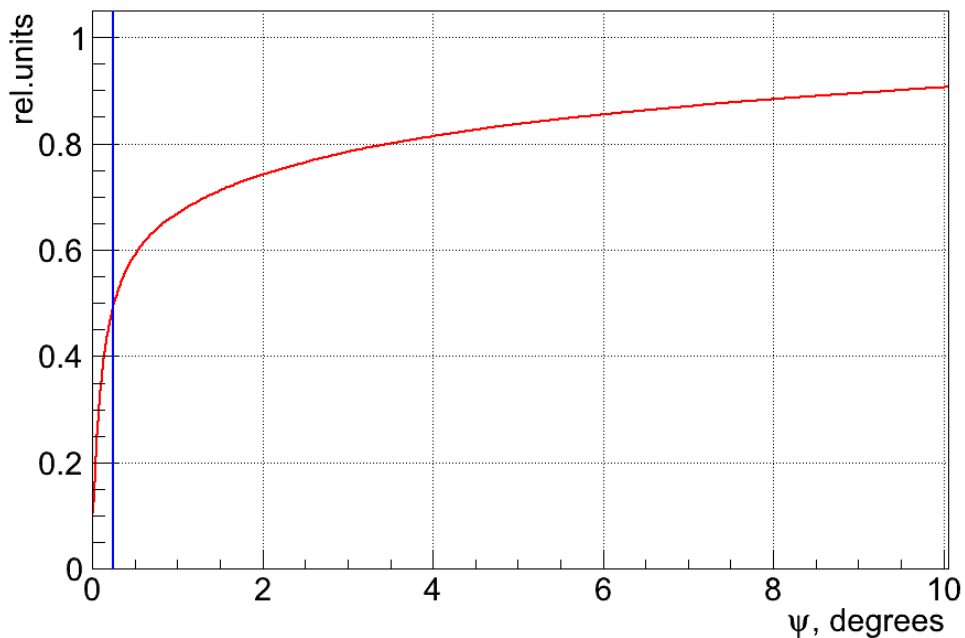


Fig. 8.1.9: The fraction of events reconstructed with mismatch angle less than a given value ψ for muons with energy of 10 TeV. The blue line pointed out the median value of the mismatch angle distribution.

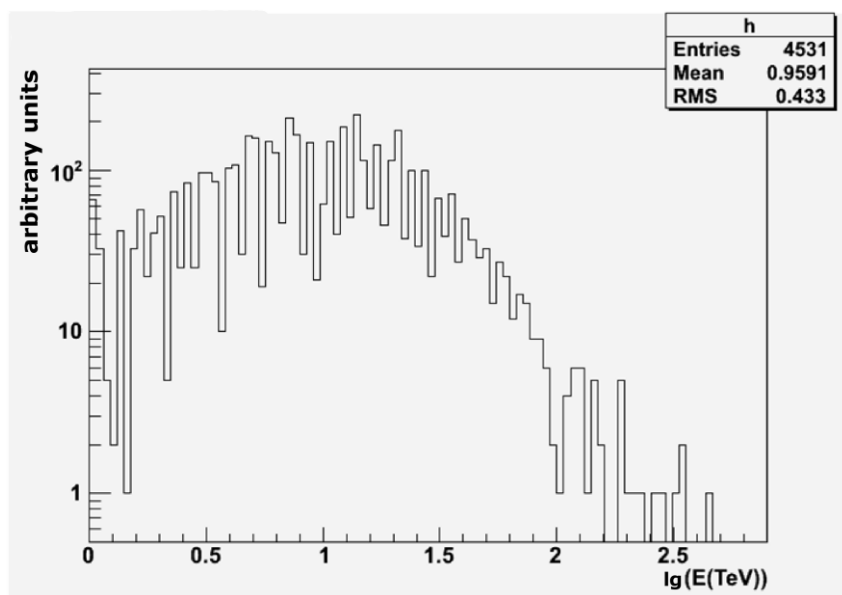


Fig. 8.1.10: The reconstructed energy of simulated 10 TeV muons.

8.2 High-Energy Showers

8.2.1 Simulation

High-energy showers are the sources of Cherenkov radiation with characteristic spatial, angular, and temporal distributions of the generated photons that are formed in the course of shower development. The development of a shower can be reproduced most completely by a MC simulation. However, implementing this procedure requires much computer time. When simulating the response of neutrino telescopes to the Cherenkov radiation of showers, it is appropriate to use analytical fits to the longitudinal distribution of charged particles along the shower axis and a universal angular distribution of Cherenkov photons (see, e.g., [77-82]). The lateral size of an electromagnetic shower is characterized by the Moliere radius (for water, $r_m \approx 9.3$ cm) and, being small, it has virtually no effect on the photo-sensor response in deep underwater experiments.

Generation of shower Cherenkov radiation

The total number of Cherenkov photons from an electromagnetic or hadronic shower is proportional to the total charged particle's tracklength L_{ch} and, accordingly, the shower energy E_{sh} :

$$N_{tot}^{ch} = n_{ch} L_{ch} = B E_{sh}, \quad (8.2.1)$$

where n_{ch} is the linear density of photons emission in the wavelength range under consideration. In particular, in the photon wavelength interval 350-600 nm, which is the operating range of detection of the Cherenkov radiation by the photo-sensors of neutrino telescopes, $n_{ch} = 240$ γ/cm . In the case of an electromagnetic shower, the coefficient of proportionality is $B = (1.04 \div 1.16) 10^5$ GeV^{-1} , depending on the variant of MC calculation [81,82]. In a case of hadronic showers particle's tracklength L_{ch} can be represented as [83]

$$L_{ch} = 625 f(\epsilon) \frac{E_{sh}}{1 GeV} \text{ cm}, \quad \epsilon = \log_{10}(E_{sh}/1 TeV), \quad (8.2.2)$$

$$f(\epsilon) = -1.27 \cdot 10^{-2} - 4.76 \cdot 10^{-2}(\epsilon + 3) - 2.07 \cdot 10^{-3}(\epsilon + 3)^2 + 0.52\sqrt{\epsilon + 3}.$$

Accordingly, the coefficient of proportionality B in Eq. (8.2.1) can be derived as

$$B = 0.86 \cdot 625 \cdot f(\epsilon) n_{ch} \text{ GeV}^{-1}, \quad (8.2.3)$$

where the factor 0.86 allows for the decrease in n_{ch} for nonrelativistic electrons in a hadronic shower [81].

The number of Cherenkov photons $N_{ch}(x, \theta, t) dx d\Omega dt$ emitted at time t from an interval dx along the shower axis near point x in a spatial angle $d\Omega$ at an angle θ to the shower axis can be represented with a sufficient accuracy as

$$N_{ch}(x, \theta, t) dx d\Omega dt \cong N_{e^\pm}(x) \Psi_{ch}(\theta) n_{ch} \delta(t - x/c) dx d\Omega dt \quad (8.2.4)$$

where $N_{e^\pm}(x)$ is the density of electrons and positrons along the shower axis, $\Psi_{ch}(\theta) \sim$ is the angular distribution of Cherenkov photons. In the case of electromagnetic showers, we use the analytical fit to $N_{e^\pm}(x)$ ($E_{sh} > 5$ GeV) proposed by Belenkii in [77]:

$$N_{e^\pm}(x) = \left(\frac{E_{sh}}{E_c}\right)^S S^{-1.5X} \exp(-2.49S + 0.5(S-1)X + 0.025), \quad (8.2.5)$$

$$S = \frac{3X}{X + 2 \ln(E_{sh}/E_c) - 2.4}, \quad E_c = 72 \text{ MeV}, X = x/X_0, X_0 = 36.1 \text{ cm}.$$

In the case of hadronic showers, we use the fit to $N_{e^\pm}(x)$ proposed in [70, 84]:

$$N_{e^\pm}(x) = S \frac{E_{sh}}{E_c} \left(1 - \frac{\lambda}{X_{max}}\right) \exp\left(\frac{X_{max} - x}{\lambda} - 1\right) \left(\frac{x}{X_{max} - \lambda}\right)^{X_{max}/\lambda} \quad (8.2.6)$$

where $X_{max} = X_r \ln(E_{sh}/E_c)$, and the parameters S , X_r , λ , and E_c derived by comparing (8.2.6) with the MC-simulation are given in Table 8.2.1.

Table 8.2.1. The parameters used in Eq. (8.2.6).

Initial particle	Proton	Pion	Kaon
S	0.11842	0.036684	0.0298
$x_r(\text{cm})$	39.502	30.802	30.997
$\lambda(\text{cm})$	113.03	115.25	119.61
$E_c(\text{GeV})$	0.17006	0.052507	0.048507

Expression (8.2.5) is a satisfactory fit to the spatial distribution of particles from an electromagnetic shower at energies of the order of several PeV or lower. When the distribution $N_{e^\pm}(x)$ is calculated at high energies, the decrease in the electron bremsstrahlung cross section and the e^+e^- pair production cross section due to the collective influence of the medium's atoms (the Landau-Pomeranchuk-Migdal (LPM) effect [85]) should be taken into account. For electromagnetic showers with $E_{sh} > 2 \cdot 10^7$ GeV and for hadronic showers with $E_{sh} > 10^9$ GeV the rise in shower length with energy due to LPM-effect was approximated as $E_{sh}^{1/3}$ according to [86].

The relative angular distribution of Cherenkov photons summed over the tracks of all charged particles from the shower $\Psi_{ch}(\theta)$ (see Fig. 8.2.1 and [87]) at $E_0 > 100$ GeV is virtually independent of the shower energy. The angular distributions of the Cherenkov photons emitted from different shower segments near the maximum of the cascade curve differ only slightly from the total distribution $\Psi_{ch}(\theta)$ [82]. This allows $\Psi_{ch}(\theta)$ to be used as a universal angular distribution of the Cherenkov photons emitted from any shower segment.

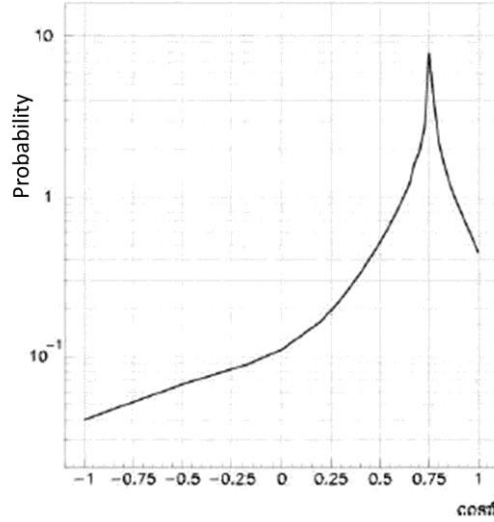


Fig. 8.2.1: The angular distribution of Cherenkov radiation from high-energy electromagnetic showers averaged over all charged particle tracks.

Thus, the number of Cherenkov photons emitted from a segment Δx along the shower axis near x can be represented as

$$N_{ch}(x, \Delta x, \theta, t) = BE_0 \Psi_{ch}(\theta) \delta(t - x/c) \int_{x-\Delta x}^{x+\Delta x} \tilde{N}_{e^\pm}(x') dx', \quad (8.2.7)$$

where $\tilde{N}_{e^\pm}(x)$ is the normalized distribution of e^\pm along the shower axis described by (8.2.5) for an electromagnetic showers or (8.2.6) for hadronic showers.

The algorithm for simulating the generation of Cherenkov radiation from high-energy showers appears as follows. The longitudinal shower length is divided into segments Δx and the shower is considered as a superposition of point sources of Cherenkov radiation located at the center of each segment Δx with the intensity $N_{ch}(x, \Delta x, \theta, t)$ derived from (8.2.7).

Light propagation and OM response

The propagation of the Cherenkov radiation of showers from the source to the photo-sensor is determined by the absorption and scattering of light in water. A characteristic feature of the high-energy showers Cherenkov radiation is a pronounced anisotropy of the angular distribution of emitted photons. In a medium without scattering, the anisotropy of the source's radiation diagram is responsible for the anisotropy of the spatial-angular distribution of photons in the medium. Generally, the scattering of light in the medium causes the spatial, angular, and temporal distributions of photons to be distorted compared to those in a medium without scattering. As an illustration of the anisotropy of the spatial distribution of photons, Fig. 8.2.2 shows the time-integrated distributions of the average number of photoelectrons as a function of $\cos\theta$ in a hypothetical photo-sensor identical in parameters to the photo-sensor of the Baikal NT200 telescope but with a uniform angular sensitivity. The photo-sensors are located at distances $R=20$ m and $R=200$ from a point-like shower of unit intensity of Cherenkov photons. The polar angle θ is measured from the direction opposite to that of the shower

axis. As can be seen from these figures, the spatial distribution retains the prominent peak attributable to the anisotropy of the angular distribution of Cherenkov radiation from showers at distances up to 200 m or more from the source. Compared to the case without scattering, the spatial distribution at fairly large distances from the shower is broadened, while the number of photons at the peak of the distribution at distances of ~ 100 and 200 m decreases approximately by a factor of 2 and 3, respectively.

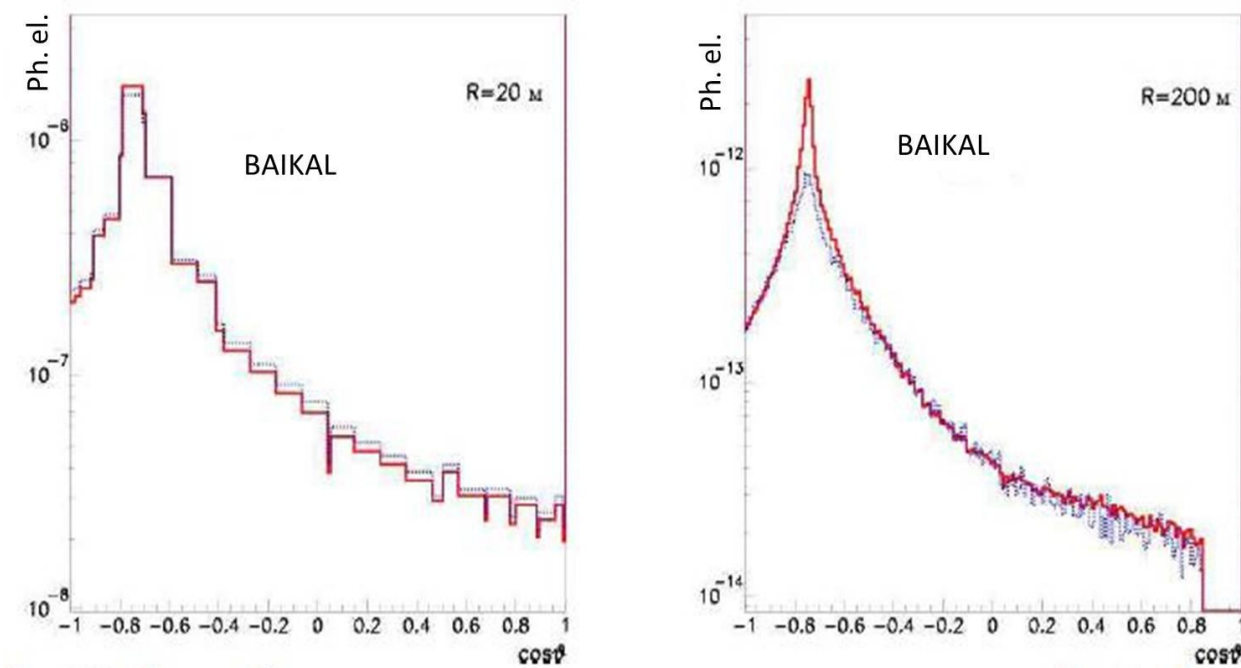


Fig. 8.2.2: The response of a spherical optical module located at $R = 20$ m (left panel) and $R=200$ m (right panel), (see text). The solid and dotted histograms correspond to the simulations without and with allowance for the light scattering in water.

In media with weak scattering and a sharp scattering phase function, which the Baikal water belongs to, the time-integrated angular distribution of Cherenkov photons from a local source (e.g., a point shower) at any spatial point has a prominent peak in a direction away from the source formed by unscattered (direct) photons or those scattered through small angles. As a result, the response of the Baikal telescope's OM oriented toward the source exceeds that of the OM turned away from the source by a factor of 50-100. Because of the wide viewing angle of OMs based on large hemispherical PMTs, the overwhelming majority of the telescope's OMs triggered from the Cherenkov radiation of shower record direct photons or those scattered through small angles.

The main factors affecting the formation of the temporal distribution of Cherenkov radiation from showers in the vicinity of a photo-sensor are: the spectral dependence of light velocity and the absorption coefficient, the scattering of light in water, and the spatial size of the shower. For OM orientations toward the shower (in the model of a point source), when the direct photons make a major contribution to the response, the temporal distribution is determined by the light velocity dispersion. In this case, the width of the temporal distribution is 4-12 ns in Baikal water, depending on the distance to the shower. The scattering for the OMs faced toward the shower begins to have an effect at distances $R > 100$ m and increases with R , widening the temporal distribution compared to the case without scattering. In the Baikal water, in the cases of OM orientations where

the response is mainly formed by direct shower photons, the extent to which the shower size affects the temporal distribution depends on the relative positions of the shower and OM. When the OM is in front of the shower, the influence of the shower size on the temporal distribution is insignificant and the shower may be considered as a point source located near the maximum of the cascade curve. Using the time information of the OMs from this spatial region, one can reconstruct the shower coordinates in the model of a point source with a good accuracy. When the OM is located behind the shower, the temporal distribution of photons at the point of detection depends on the shower energy and its distance from the OM and can lead to a fairly significant broadening of the temporal distribution.

The characteristic features of the generation and propagation of Cherenkov radiation in the Baikal water listed above, on the one hand, and the functional peculiarities of the photo-sensors used in neutrino telescopes, on the other hand, allow one to implement a fairly efficient algorithm for reconstructing the parameters of high-energy showers using the time and amplitude information from the neutrino telescope's photo-sensors. This algorithm is based on comparison of the experimental information with the expected amplitude-time response of the telescope and assumes a detailed simulation of the emission, propagation, and detection of Cherenkov photons from showers. The MC simulation is performed with the standard computational software package of the Baikal collaboration. One of the important parts of these computational tools is the software package that allows the temporal distribution of the average number of photoelectrons in a photo-sensor as a function of its spatial location and orientation with respect to the shower to be calculated. The calculation yields a five-dimensional table for the average number of photoelectrons $n_{pe}(\rho, z, \theta, \varphi, \tau)$ in a volume of $\sim 10^8$ m³ around the shower. The variables ρ and z characterize the OM position relative to a point-like shower - the distance from the OM to the shower axis ρ and the coordinate along the z axis oriented in the direction opposite to that of the shower axis. The polar angle θ (measured from the direction coincident with the z direction) and the azimuth angle φ characterize the orientation of the OM with respect to the shower. The variable τ characterizes the time delay of the recorded photons relative to the arrival time of the direct photons.

8.2.2 Reconstruction

Reconstruction of the shower vertex

The procedure for reconstructing the parameters of high-energy showers - the shower energy, direction, and vertex - is performed in two steps. In the first step, the shower vertex coordinates \vec{r}_{sh} are reconstructed using the time information from the telescope's triggered photo-sensors. In this case, the shower is assumed to be a point source of light. The values of the parameters corresponding to the χ^2 -minimum value of are chosen as the shower coordinates $((x, y, z)$ in a rectangular coordinate system or (r, θ, φ) in a spherical coordinate system):

$$\chi_t^2 = \frac{1}{(N_{hit} - 4)} \sum_{i=1}^{N_{hit}} \frac{(T_i(\vec{r}_{sh}, t_0) - t_i)^2}{\sigma_{ti}^2}, \quad (8.2.8)$$

where t_i and T_i are the measured and theoretically expected trigger times of the i th photo-sensor, t_0 - the shower generation time, σ_{ti} - the uncertainty in measuring the time, and N_{hit} is the hit multiplicity. As has already been noted above, in the case of detecting the Cherenkov radiation of high-energy showers in the Baikal water, the bulk of the photo-sensors are triggered from direct photons or those scattered through small angles. This simplifies considerably the shower coordinate reconstruction procedure. More specifically, the propagation time of the direct photons from the shower to the corresponding photo-sensor can be chosen as the theoretically expected time T_i . The reconstruction quality can be increased by applying additional event selection criteria based on the limitation of the admissible values for the specially chosen parameters characterizing the events.

Reconstruction of the shower energy and direction

In the second step, the shower energy and direction are reconstructed by applying the maximum likelihood method and using the shower coordinates reconstructed in the first step. The values of the variables θ , φ , and E_{sh} corresponding to the minimum value of the following functional are chosen as the polar and azimuth angles characterizing the direction and the shower energy:

$$L_A = - \sum_{i=1}^{N_{hit}} \ln p_i \left(A_i, E_{sh}, \vec{\Omega}_{sh}(\theta, \varphi) \right). \quad (8.2.9)$$

The functions $p_i(A_i, E_{sh}, \Omega_{sh}(\theta, \varphi))$ are the probabilities for a signal with amplitude A_i (measured in photoelectrons) from a shower with energy E_{sh} and direction Ω_{sh} to be recorded by the telescope's i th triggered photo-sensor:

$$p_i = \sum_{n=1}^{\infty} P(n/\bar{n}) \int_{A_i - \frac{\alpha}{2}}^{A_i + \frac{\alpha}{2}} \xi_i(A, n) dA, \quad (8.2.10)$$

where $P(n/\bar{n})$ is the probability of detecting n photoelectrons at a mean \bar{n} for the Poisson distribution, $\xi_i(A, n)$ is the probability density function for recording the amplitude A at an exposure level of n photoelectrons, and α is the scale-division value of the amplitude coder in photoelectrons. The mean \bar{n} are determined by simulating the responses of the telescope's OMs to the Cherenkov radiation of a shower with energy E_{sh} and direction Ω_{sh} with allowance made for the light propagation in water, the relative positions and orientation of the OMs and the shower, and the effective OM sensitivity.

8.2.3 Shower angular and energy resolutions

As has already been noted above, the efficiency of investigating astrophysical neutrino fluxes depends both on the sensitivity of the neutrino telescope and on its resolution with respect to the measurement of the energy and direction of secondary muons and showers. To investigate the energy and angular resolutions of the telescope's configuration with respect to the detection of high-energy showers, its response to the

Cherenkov radiation of showers had been simulated and then the showers energy, direction, and vertex coordinates were reconstructed.

Figures 8.2.3 and 8.2.4 illustrate the efficiency of reconstructing the coordinates, energy, and direction of high-energy showers. Figure 8.2.3 (left panel) presents the distribution of events in variable $dr = |\vec{r} - \vec{r}_{rec}|$, where \vec{r} and \vec{r}_{rec} are the simulated and reconstructed vertex coordinates of a shower with energy $E_{sh}=10^6$ GeV relative to the telescope's center. The mean of this distribution is 5.5 m. The energy resolution for showers with $E_{sh}=10^6$ GeV is shown in Fig. 8.2.3 (right panel). The shower energy reconstruction accuracy is about of 19-21% in $\log_{10}(E_{rec}/E_{sh})$. The direction resolution of showers with $E_{sh}=10^6$ GeV is shown in Fig. 8.2.4. The median value of the mismatch angle ψ distribution is 4.5° and its mean value is 6.2° .

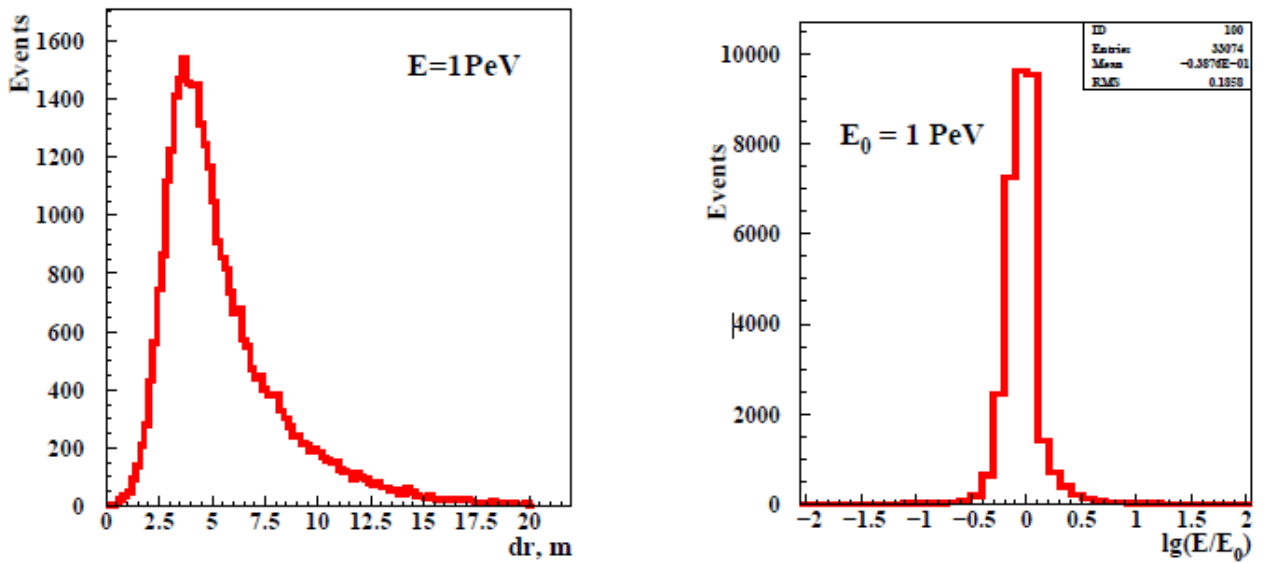


Fig. 8.2.3: Left panel – the 1 PeV shower vertex resolution. Right panel - the 1PeV shower energy resolution.

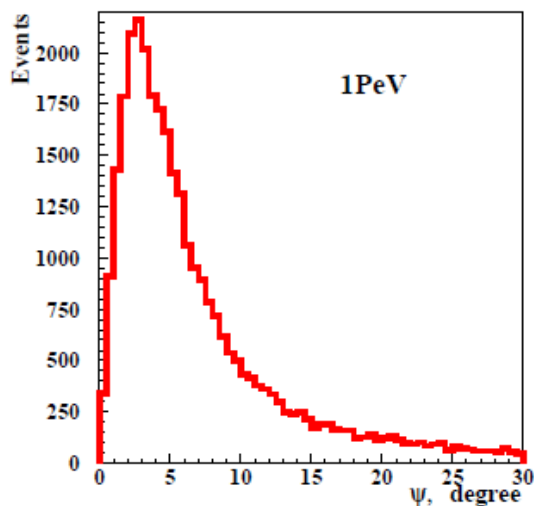


Fig. 8.2.4: The mismatch angle ψ between the simulated and reconstructed shower directions.

The reconstruction efficiency depends on the multiplicity of hit OMs N_{hit} , which increases with shower energy. In Fig. 8.2.5 (left panel), the dependences of vertex resolution on hit multiplicity for four shower energies (the energies are given in Fig. 8.2.5

near the corresponding distributions) are shown. Vertex reconstruction accuracy improves with increasing number of hit photo-sensors. The shower vertex reconstruction accuracy for 70% of the events is $\sim 2-4$ m, depending on the shower energy. The dependences of energy resolution on hit multiplicity for different shower energies are shown in Fig. 8.2.5 (right panel).

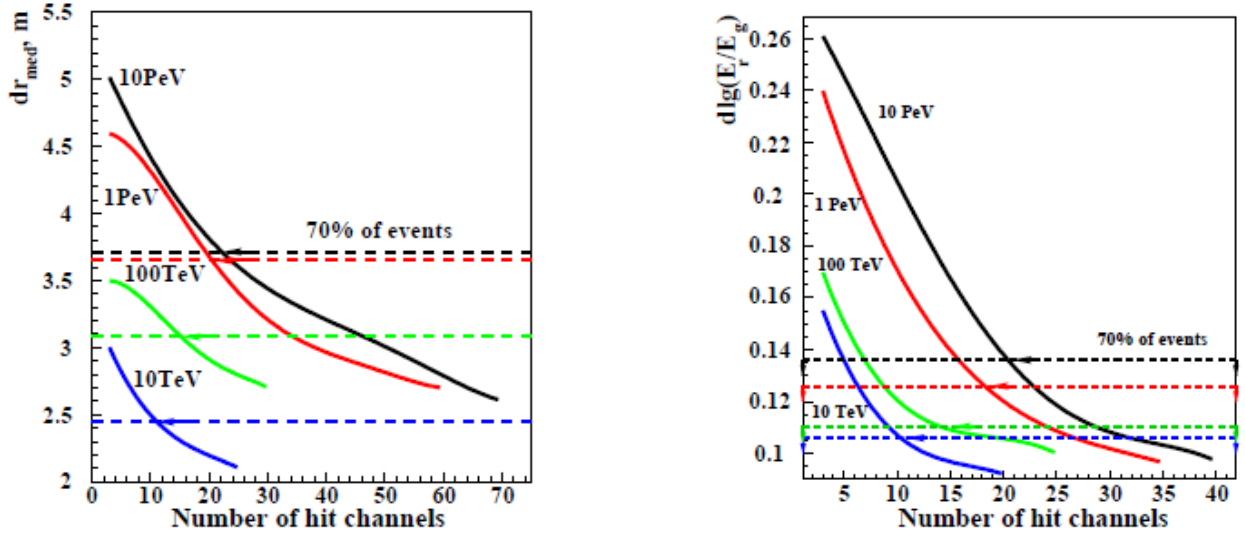


Fig. 8.2.5: Left panel – dependence of vertex resolution on hit multiplicity for various shower energies. Right panel – dependence of energy resolution on hit multiplicity for various shower energies.

The accuracy of energy reconstruction for 70% of the events is 8-13% in $\log_{10}(E_{rec}/E_{sh})$ or 20-35% in shower energy. The median mismatch angle dependence on hit multiplicity is shown in Fig. 8.2.6. This distribution is virtually independent of the shower energy. The accuracy of reconstructing the shower direction for 70% of the events is 3.5-6.5 degrees.

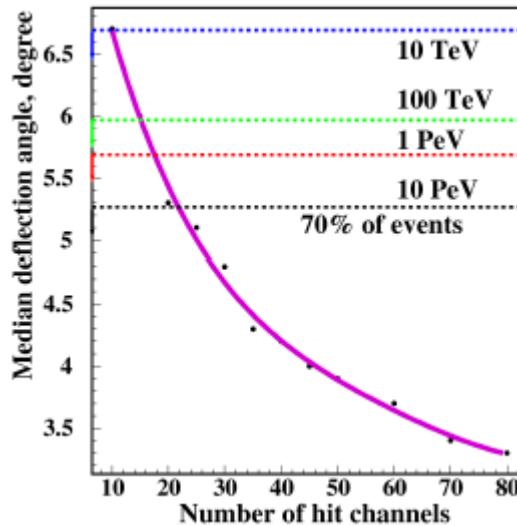


Fig. 8.2.6: Median mismatch angle ψ_{med} dependence on hit multiplicity.

Thus, the telescope's configuration chosen as a result of our optimization calculations has energy and angular resolutions adequate for the requirements of the

studies of the energy spectrum, global and local anisotropies, and composition in neutrino flavours of the astrophysical neutrino fluxes.

8.2.4 The diffuse neutrino flux detection efficiency

Apart from the efficiency of detecting secondary showers by the array itself, the efficiency of detecting astrophysical neutrino fluxes by the BAIKAL-GVD telescope also depends on the shape of the neutrino energy spectrum and the direction of neutrino arrival at the array. The neutrino flux that reaches the telescope's neighborhood from below the horizon undergoes attenuation and transformation of the primary energy spectrum when passing through the Earth. The degree of flux distortion is different for different neutrino flavours and depends on the zenith angle of the neutrino propagation. In Fig. 8.2.7 (left panel), the effective area for the detection of an isotropic flux of electron neutrinos is shown for various ranges of zenith angles (2304 OMs). At energies above 100 TeV, the flux from below the horizon is suppressed through the interaction of neutrinos with the Earth's matter. In Fig. 8.2.7 (right panel), the energy dependence of detection probability is shown for various power-law spectra. The indices of the power-law spectra are given near the corresponding distributions. The effective detection energy range is shifted toward higher energies as the spectral index decreases.

Figure 8.2.8 shows the expected energy distributions of events from an isotropic power-law flux of electron-neutrinos $F(E)=10^{-7}E^{-2}$ GeV⁻¹ cm⁻² s⁻¹ sr⁻¹ for one year exposure and selection requirement 10/3 (≥ 10 hit OMs on ≥ 3 strings). Assuming zero expected background for exposure of three years, the limit on the total diffuse flux for all flavours of neutrinos with a spectrum $\sim E^{-2}$ at the 90% confidence level will be $E^2F=5\cdot 10^{-9}$ GeV cm⁻²s⁻¹ sr⁻¹.

In searching for local neutrino sources based on the detection of muon neutrinos for an energy spectrum E_ν^{-2} typical for the cosmic-ray acceleration at shock waves, the expected limit under the assumption of zero background in a three years of data collection will be $E^2F=2\cdot 10^{-12}$ TeV cm⁻² s⁻¹ at the 90% confidence level for declinations from -90° to -38° .

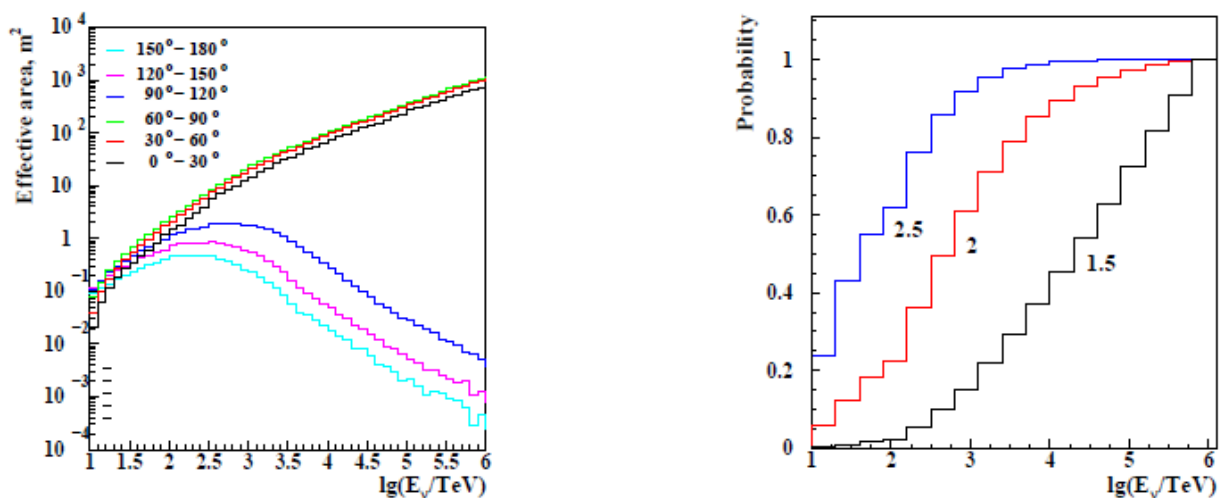


Fig. 8.2.7: Left panel – dependence of effective area on neutrino energy for different arrival directions. Right panel – energy dependence of detection probability for various energy spectra.

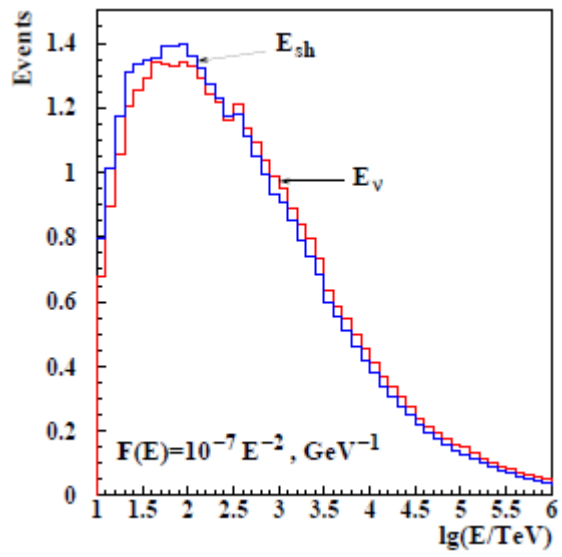


Fig. 8.2.8: The distributions of expected events from electron-neutrinos in energy of neutrinos and secondary showers for exposure time of one year. A source strength for electron-neutrinos and antineutrinos for a level $E^2 F(E)=10^{-7} \text{ GeV cm}^{-2} \text{ c}^{-1} \text{ sr}^{-1}$ is assumed.

9 FINAL CONFIGURATION of the BAIKAL-GVD

As was mentioned earlier, design and architecture of measuring, trigger and communication systems of the BAIKAL-GVD have a modular structure. This allows rather easy extension of array by adding additional unified units. The design and performance of the BAIKAL-GVD basic elements and systems have been discussed previously as parts of array with 2304 OMs, comprising 12 clusters. At present the array with roughly four times larger instrumented volume is considered as a basic one.

The basic configuration of telescope with 10368 optical modules consists of 27 clusters – functionally independent sub-arrays, which are connected to shore by electro-optical cables (see, Fig. 9.1-9.4). Each cluster comprises eight 705 m long strings of optical modules – seven peripheral strings are uniformly arranged at a 60 m distance around a central one. Each string comprises 48 OMs spaced by 15 m at depths of 600 m to 1300 m below the surface. OMs on each string are combined in four sections – detection units of telescope. The distances between the central strings of neighboring clusters are $H=300$ m. The clusters are spaced over an area of approximately two square kilometers. The water volume instrumented by OMs is about of 1.4 km^3 .

Muon effective areas for two GVD configurations are shown in Fig. 9.5. The curves labeled by GVD*4 and GVD relate to configurations with 10368 OMs and 2304 OMs, respectively. Muon effective area for basic configuration (6/3 condition) rises from 0.3 km^2 at 1 TeV to 1.8 km^2 asymptotically. Muon direction resolution (median mismatch angle) for basic configuration is about of 0.25° .

Shower effective volumes for GVD configurations are shown in Fig. 9.6. The curves labeled by GVD*4 and GVD relate to configurations with 10368 OMs and 2304 OMs, respectively. Shower effective volumes (10/3 condition) for basic configuration are about of $0.4\text{--}2.4 \text{ km}^3$ above 10 TeV. The accuracy of shower energy reconstruction is about of 20-35% depending on shower energy. The accuracy of reconstructing the shower direction is about 3.5-6.5 degrees.

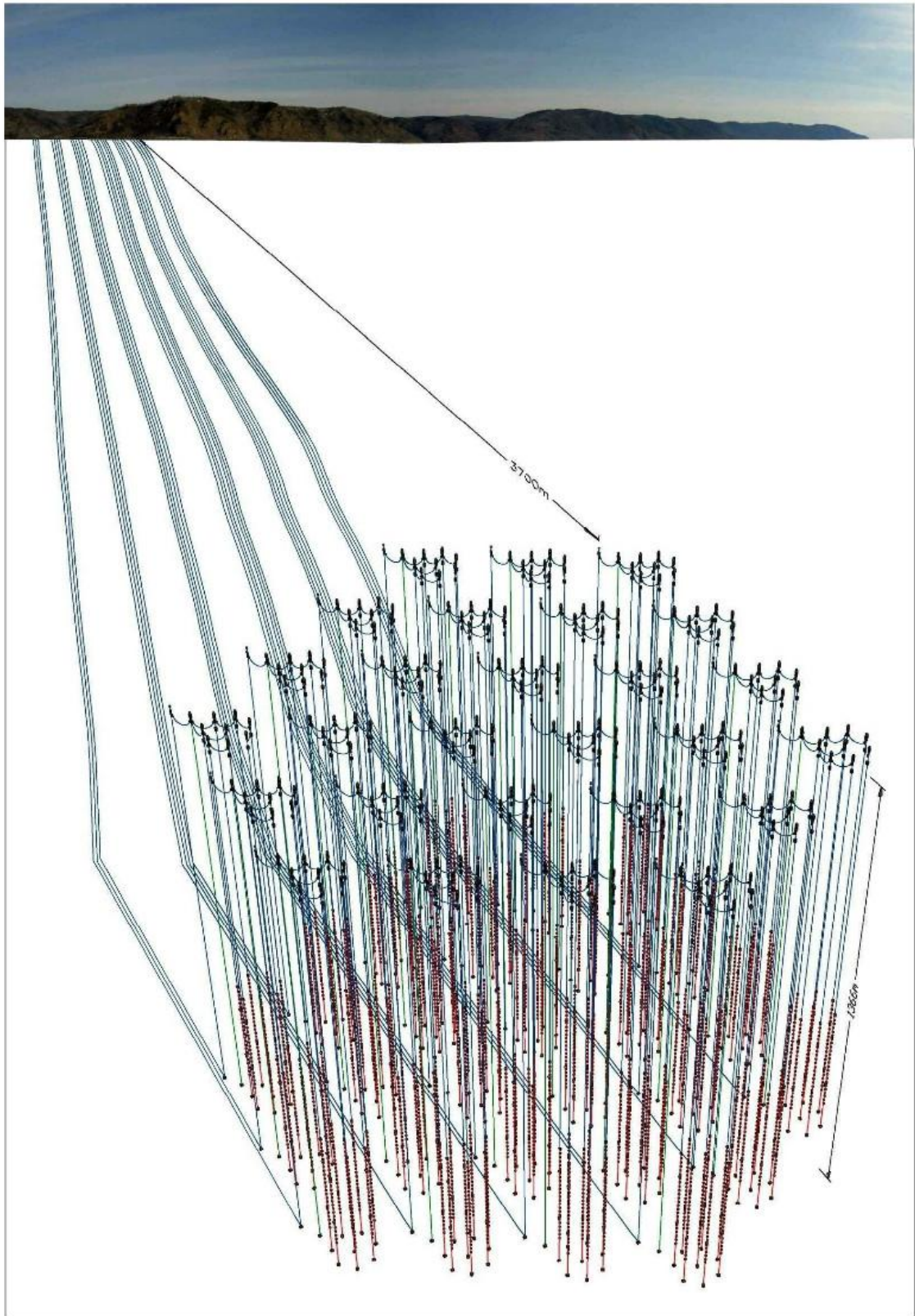


Fig. 9.1: Artistic view of BAIKAL-GVD with 27 clusters.

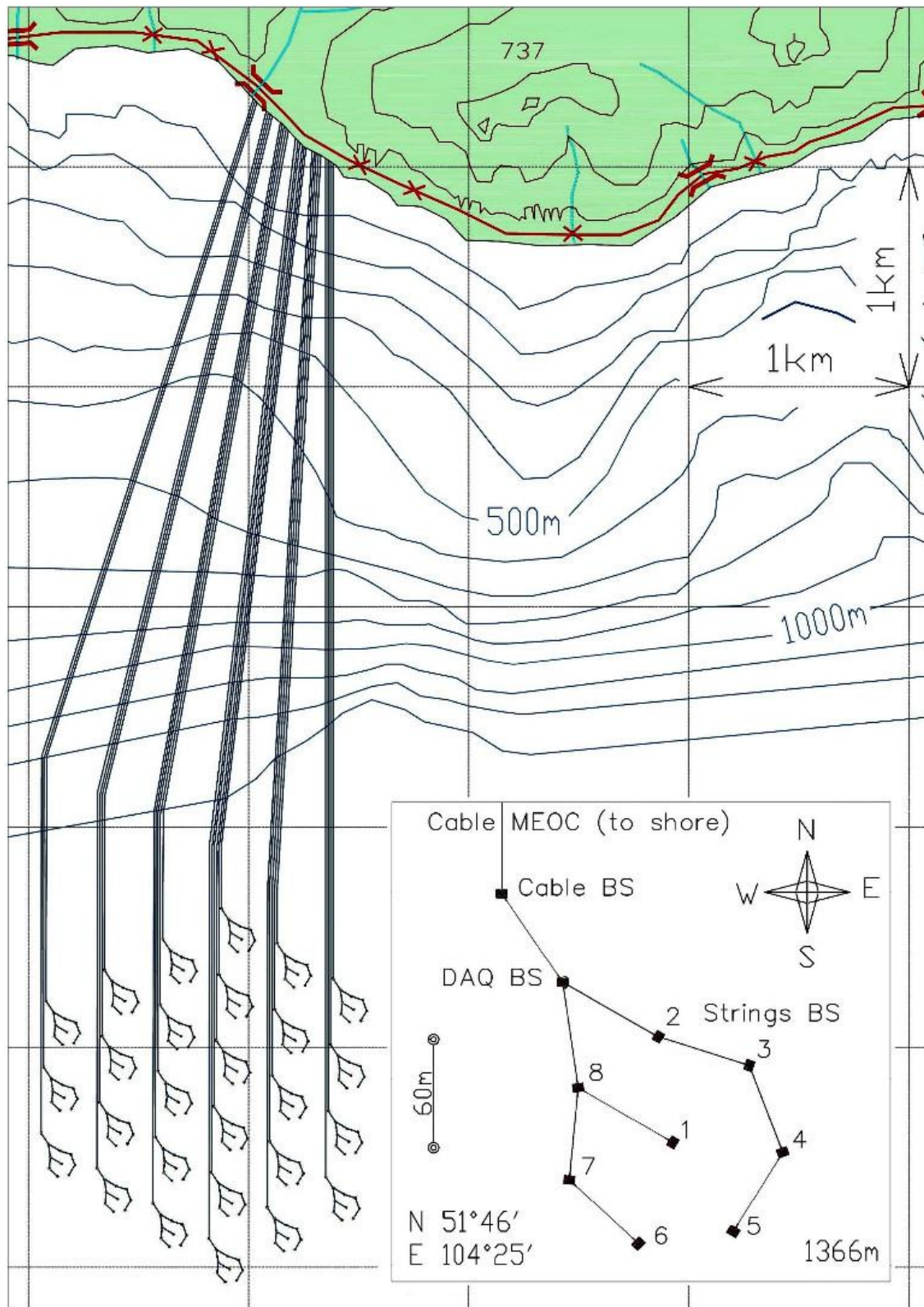


Fig. 9.2: Layout of BAIKAL-GVD with 27 clusters. In the right panel layout of one cluster is shown. Here MEOC – main electro-optical cable to shore; BS – buoy stations.

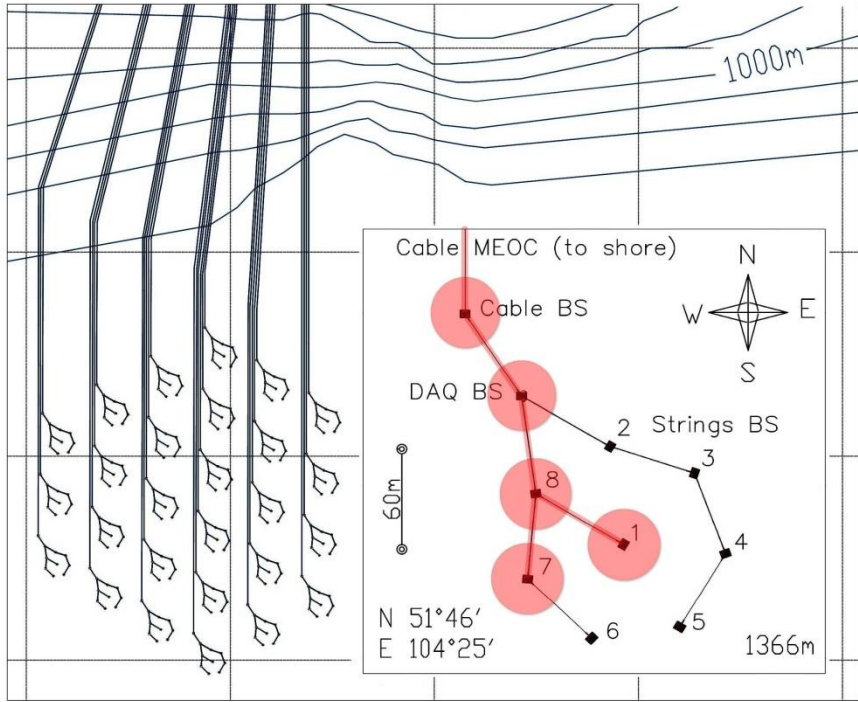


Fig. 9.3: The same as in Fig. 9.2. In the right panel filled circles indicate deployed Cable, DAQ and three String buoy stations of the first GVD cluster.

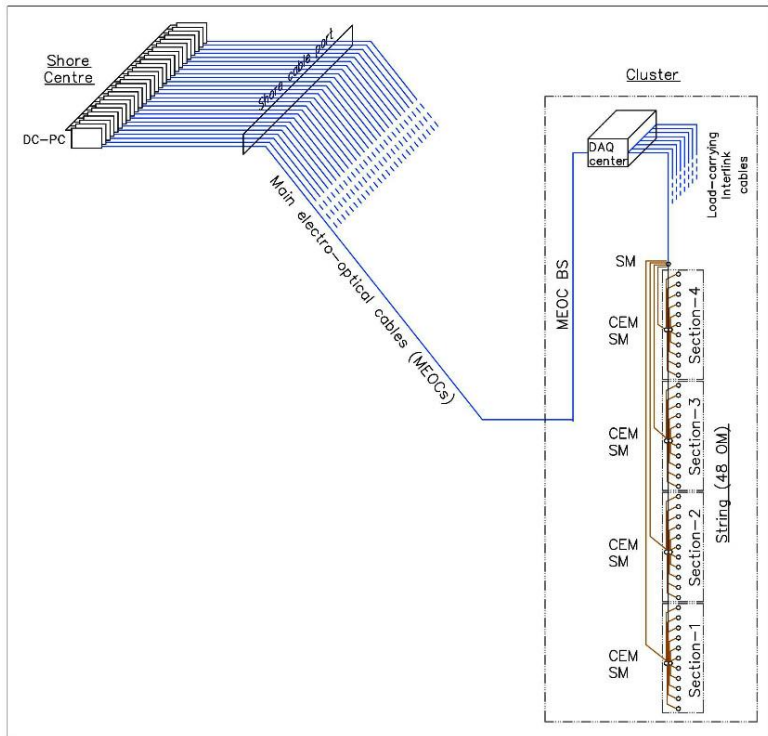


Fig. 9.4: Schematic view of the cable network.

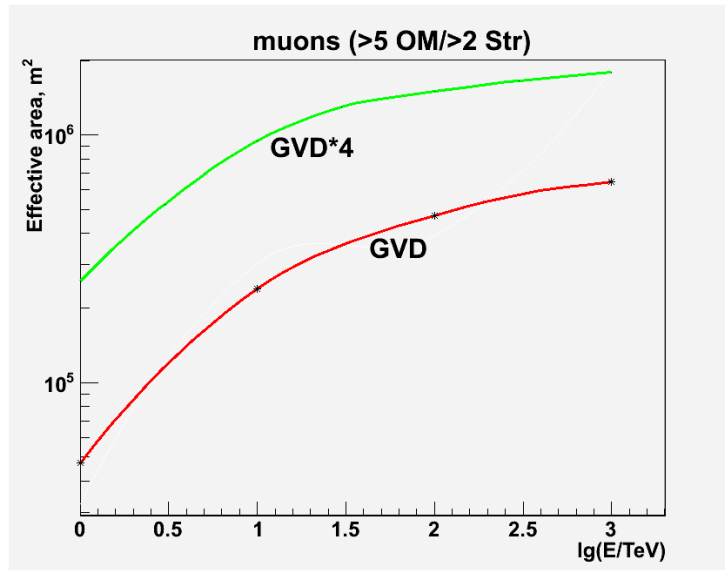


Fig. 9.5: GVD effective area for muon detection. The curves labeled by GVD*4 and GVD relate to configurations with 10368 OMs and 2304 OMs, respectively.

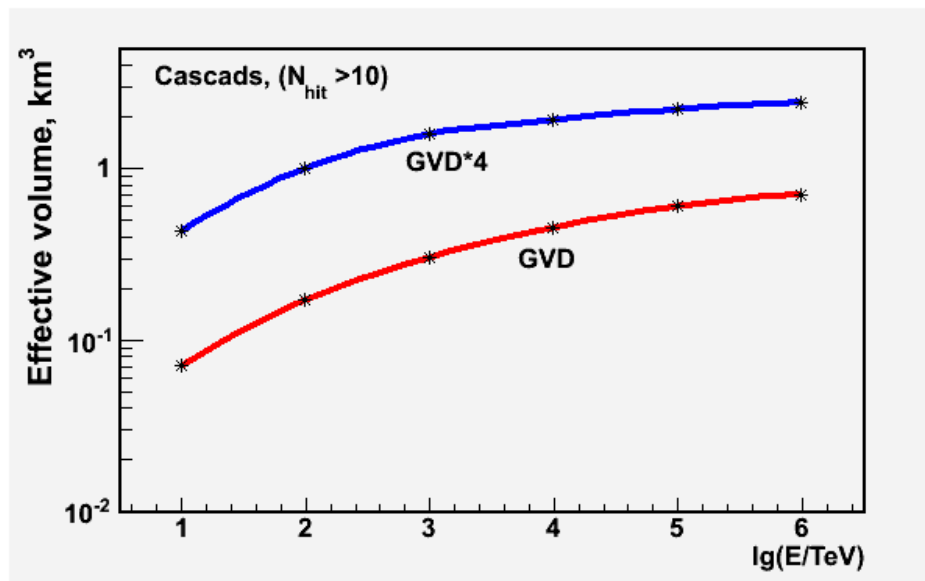


Fig. 9.6: GVD effective volume for shower detection. The curves labeled by GVD*4 and GVD relate to configurations with 10368 OMs and 2304 OMs, respectively.

BIBLIOGRAPHY

- [1] Markov M.A., Proc. of 10th ICHEP, Rochester, (1960) 572.
- [2] Berezhinsky V.S. and Zatsepin G.T., Sov. Phys.- Uspekhi, 122 (1977) 1.
- [3] Learned J.G. and Mannheim K., Ann. Rev. Nucl. Part. Sci. 50 (2000) 679.
- [4] Katz U. and Spiering Ch., Prog. Part. Nucl. Phys., 67 (2012) 651.
- [5] Fukuda Y., Hayakawa T., Ichikawa E. et al., Phys. Rev. Lett. 81 (1998) 1562.
- [6] Dirac P.-A. M., Proc. Roy. Soc. A133 (1931) 60.
- [7] Frank I.M., Vavilov-Cherenkov radiation. Moscow, Nauka, (1988) 192.
- [8] 'tHooft G., Nucl. Phys. B (Proc. Suppl.). 79 (1974) 276.
- [9] Polyakov A.M., JETP Lett. 20 (1974) 194.
- [10] Domogatskii G.V. and Zheleznykh I.M., Sov. J. Nucl. Phys. 10 (1969) 702.
- [11] Parker E.N., Astrophys. J. 160 (1970) 383.
- [12] Turner M.S. et al., Phys. Rev. D26 (1982) 1296.
- [13] Rubakov V.A. JETP Lett. 33 (1981) 644.
- [14] Callan C.G. Phys. Rev. D26 (1982) 2058.
- [15] Bezrukov L.B. et al. Sov. J. Nucl. Phys. 52 (1990) 86.
- [16] The Baikal Neutrino Telescope NT-200. Project Description: Tech. rep. Moscow: INR RAS, 1992.
- [17] Avrorin A.V. et al. Preprint INR RAS 1265/2010, 2010.
- [18] Andres E. et al. Astropart. Phys. 13 (2000) 1.
- [19] Ageron M. et al., Nucl. Inst. Meth. A656 (2011) 11.
- [20] Abbasi R. et al. Nucl. Inst. and Meth. A601 (2009) 294.
- [21] Katz U.F. Nucl. Inst. and Meth. A602 (2009) 40.
- [22] Proc. 1976 DUMAND Summer Workshop / Ed. by A. Roberts. Honolulu: 1977.
- [23] DUMAND Coll., P. Bosetti et al., DUMAND II: Proposal to construct a deep-ocean laboratory for the study of high energy neutrino astrophysics and particle physics, Tech. Rep. HDC-2-88, Hawaii DUMAND Center, University of Hawaii (1988).
- [24] Bolesta J.W. et al. Proc. 25-th ICRC Durban. 7 (1997) 29.
- [25] Resvanis L.K. et al., Nucl. Phys. Proc. Suppl. 35 (1994) 294.
- [26] Aggouras G. et al., Nucl. Inst. and Meth. A552 (2005) 420.
- [27] Aggouras G. et al., Astropart. Phys. 23 (2005) 377.
- [28] NEMO homepage: <http://nemoweb.lns.infn.it>.
- [29] Capone A. et al., Nucl. Inst. and Meth. A602 (2009) 47.
- [30] IceCube homepage: <http://www.icecube.wisc.edu/>
- [31] Ahrens J. et al., Astropart. Phys. 20 (2004) 507; arXiv:astro-ph/0305196.
- [32] Bagley P. et al. (KM3NeT Coll.) 2008, Conceptual design report, ISBN 978-90-6488-031-5, www.km3net.org.
- [33] Bagley P. et al. (KM3NeT Coll.) 2010, Technical design report, ISBN 978-90-6488-033-9, available from: www.km3net.org.
- [34] Ackermann M. et al., J. Geophys. Res., 111 (2006) D13203.
- [35] Balkanov V. et al. Nucl. Inst. and Meth. A498 (2003) 231.
- [36] Tarashchanskii B.A., Gaponenko O.N. and Dobrynin V.I., Atmos. Oceanic Opt. 7 (1994) 819.
- [37] Gaponenko O.N., Mirgazov R.R. and Tarashchanskii B.A., Izv. Atmos. Oceanic Opt. 9 (1996) 677.

- [38] Budnev N.M. et al., Atmospheric and ocean optics. 18 (2005) 109.
- [39] Bezrukov L.B. et al., Proc. XI. Conf. on Neutrino Physics and Astrophysics, Nordkirchen, Germany: 550
- [40] BAIKAL-Collaboration, Eds. Sokalski, I. and Spiering, Ch. (1992), The Baikal Neutrino Telescope NT-200, Tech. Rep. Baikal-92-03, DESY/INR.
- [41] Alatin S.D. et al., Nucl. Phys. B (Proc. Suppl.) 28A (1992) 491.
- [42] Bagduev R. et al. Nucl. Inst. and Meth. A420 (1999) 138.
- [43] Belolaptikov I.A. et al., Nucl. Phys. B (Proc. Suppl.) 35 (1994) 290.
- [43] Balkanov V.A. et al., Astropart. Phys., 12 (1999) 75.
- [44] Balkanov V. et al., App. Opt., 38 (1999) 6818.
- [45] Avrorin A.V. et al., Astronomy Lett. 35 (2009) 651.
- [46] Avrorin A.V. et al., Astronomy Lett. 37 (2011) 692.
- [47] Aynutdinov V. et al., Astropart. Phys. 29 (2008) 366.
- [48] Antipin K. et al., Proc. of the First Workshop on Exotic Physics with Neutrino Telescopes (EPNT06), Uppsala, Sweden 2006, p.34.
- [49] Avrorin A. et al., Proc. of the 31st ICRC Conference, Lodz, Poland, 2009; arXiv:0205.304.
- [50] Avrorin A.V. et al., Nucl. Instr. and Meth. A 639 (2011) 30.
- [51] Avrorin A.V. et al., Instr. and Exp. Tech. 54 (2011) 649.
- [52] Balkanov V.A. et al., Phys. Atomic Nucl. 62 (1999) 949.
- [53] Balkanov V.A. et al., Astropart. Phys. 14 (2000) 61.
- [54] Balkanov V.A. et al., Nucl. Phys. B (Proc. Suppl.) 77 (1999) 486.
- [55] Aynutdinov V. et al., Astropart. Phys. 25 (2006) 140.
- [56] Aynutdinov V.M. et al., Acoustical Phys. (2005), v.51, No 6, P. 619.
- [57] Capone A. et al., Nucl. Instr. and Meth. A 487 (2002) 423.
- [58] Avrorin A. et al., Nucl. Instr. and Meth. A 693 (2012) 186.
- [59] Pelevin V.N., Izvestiya of Academy of Sciences, USSR. Atmospheric and Ocean Physic. 1 (1965) 539.
- [60] Pelevin V.N. and Prokudina T.M., Ocean and atmospheric optics, Nauka Publ., Leningrad, 1972, 148.
- [61] Pope R.M. and Fry E.S., Appl. Optics 36 (1997) 8710.
- [62] Pelevin V.N. and Rostovseva V.V., Atmospheric and ocean optics, 10 (1997) 989.
- [63] <http://www.pskovgeokabel.ru/catalog/cabel/armir/72>
- [64] Tamm I. E. and Frank I. M. J. Phys. USSR, 1 (1939) 439.
- [65] Kuzmichev L.A. Nucl. Inst. and Meth. A482 (2001) 304.
- [66] Capdevielle L. et al., KfK Report 4998. Karlsruhe: Kernforschungs/.entrum, 1992.
- [67] Калмыков Н.Н., Остапченко С. С., Ядерная физика, 56 (1993) 105.
- [68] Wiebel-Sooth B., Biermann P. Cosmic Rays. 1999.
- [69] Волкова Л.В., Зацепин Г.Т., Кузьмичев Л.А., Ядерная физика. 29 (1980) 1252.
- [70] Gaisser T. Cosmic Rays and Particle Physics. Cambridge University Press, 1990.
- [71] Agrawal V., Gaisser T., Lipari P., Stanev T., Phys. Rev. D. 53 (1996) 1314.
- [72] Lai H.L. et al., /Phys. Rev. D. 55 (1997) 1280.
- [73] Sokalsky I.A., Bugaev E.V., Klimushin S.I., Phys. Rev. D. 64 (2001) 074015.
- [74] Honda M. et al., Prog. Theor. Phys. Suppl. 123 (1996) 483.
- [75] Belolaptikov I.A. et al. , Astropart. Phys. 7 (1997) 263.
- [76] Dzhilkibaev Zh-A.M., Preprint Moscow: INR RAS 1068/2001, 2001;

- Dzhilkibaev Zh-A.M. et al., Proc. of the Workshop on Technical Aspects of a Very Large Neutrino Telescope in the Mediterranean Sea, Ed. by E. de Wolf, NIKHEF, Amsterdam, the Netherlands, 2004, p.99.
- [77] Belen'kii S.Z., Particle cascade phenomena in cosmic rays. Moscow: Gostechizdat, 1948.
- [78] Greisen K., Progress in Cosmic Ray Physics, Ed. by JI. Wilson. Amsterdam: North-Holland, 3 (1956) 3.
- [79] Hillas A., J. Phys. G8 (1982) 1461.
- [80] Fenyves E. et al., Phys. Rev. D. 37 (1988) 649.
- [81] Wiebusch C. Detection of faint light in deep underwater neutrino telescope: Ph.D. thesis. Aachen, Germany, 1995.
- [82] Bezrukov L. and Butkevich A., Proc. of workshop "Simulation and Analysis Methods for Large Neutrino Telescopes". Ed. by Ch.Spiering; DESY Zeuthen. Germany: 1998.
- [83] Alvarez-Muniz J. and **Zas** E., Phys. Lett. B. 434 (1998) 396.
- [84] Alvarez-Muniz J. and Zas E., (1999) URL: <http://arxiv.org/abs/astro-ph/9906347>.
- [85] Migdal A., Phys. Rev. 103 (1956) 1811.
- [86] Alvarez-Muniz J. and Zas.E., Phys. Lett. B. 411 (1997) 218.
- [87] Belyaev A., Ivanenko L, Makarov V., Proc. of the 1978 DUMAND Summer Workshop / Ed. by A. Roberts. Vol. 1. 1979. P. 337.